



HAL
open science

Experimental Investigation of Size Effects on Surface Phonon Polaritons and Phonon Transport

Yunhui Wu

► **To cite this version:**

Yunhui Wu. Experimental Investigation of Size Effects on Surface Phonon Polaritons and Phonon Transport. Thermics [physics.class-ph]. Université Paris Saclay (COMUE), 2019. English. NNT : 2019SACLC012 . tel-02135264

HAL Id: tel-02135264

<https://theses.hal.science/tel-02135264>

Submitted on 21 May 2019

HAL is a multi-disciplinary open access archive for the deposit and dissemination of scientific research documents, whether they are published or not. The documents may come from teaching and research institutions in France or abroad, or from public or private research centers.

L'archive ouverte pluridisciplinaire **HAL**, est destinée au dépôt et à la diffusion de documents scientifiques de niveau recherche, publiés ou non, émanant des établissements d'enseignement et de recherche français ou étrangers, des laboratoires publics ou privés.

Experimental Investigation of Size Effects on Surface Phonon Polariton and Phonon Transports

Thèse de doctorat de l'Université Paris-Saclay
préparée à CentraleSupélec

Ecole doctorale n°579 Sciences mécaniques et énergétiques, matériaux et
géosciences (SMEMAG)
Spécialité de doctorat : Énergétique

Thèse présentée et soutenue à à Gif-sur-Yvette, le 31/01/2019, par

YUNUI WU

Composition du Jury :

M. Franck ENGUEHARD Professeur, Université de Poitiers	Président
M. Younes EZZAHRI Professeur associé, Université de Poitiers	Rapporteur
M. Masahiro NOMURA Professeur associé, University of Tokyo	Examineur
M. Jose ORDOÑEZ-MIRANDA Chargé de Recherche, Université de Poitiers	Examineur
M. Jean-François ROBILLARD Professeur associé, Université de Lille	Examineur
M. Konstantinos TERMENTZIDIS Chargé de Recherche, Université de Poitiers	Rapporteur
M. Sebastian VOLZ Directeur de Recherche, University of Tokyo	Directeur de thèse

Acknowledgements

First and foremost, I offer my sincerest gratitude to my family for their firm support and always concern.

My deepest gratitude goes to my supervisor Sebastian Volz, who supervised my study during three years and offered me the opportunities to participate in the conferences and scientific collaborations. I am also grateful to his patient guidance and many advices.

I would like to thank all the members from Thermal Nanoscience group (Sergei Gluchko, Brice Davier, Romain Bude, Lantao Yu, Haoxue Han, Jordan Soussi, Benoît Latour, Wassim Kasseem, Juliana Jaramillo, Laurent Tranchant, Shiyun Xiong, Aymeric Ramiere, Jose Ordonez-Miranda, Shenghong Ju) for all the constructive advices and fruitful discussions.

I am also grateful to all the colleagues from EM2C laboratory, especially Yi Ding and David Charalampous for their help during three years. I also would like to express my thanks to Noï Lavaud, Nathalie Rodrigue and Brigitte Llobel for their assistances in the administration.

Special thanks to Professor Nomura for his acceptance and active guidance during my fifteen months visit in his laboratory. I want to acknowledge all the members from Nomura laboratory, especially Roman Anufriev and Ryoto Yanagisawa for their support and creating a warm environment to enjoy my stay and to conduct my research.

Last but not least, I also want to thank Mikyung Lim and Rajasekar P. who joined our team for six months visit and had a significant influence on my work. I also would like to thank Ramirez Rincon Jorge Andres from Institute Pprime for the collaborative projects.

Abstract

Thermal conduction becomes less efficient as structures scale down into submicron sizes since phonon-boundary scattering becomes predominant and impedes phonons more efficiently than Umklapp scattering. Recent studies indicated that the surface phonon polaritons (SPhPs), which are the evanescent electromagnetic waves generated by the hybridization of the optical phonons and the photons and propagating at the surface of a polar dielectric material surface, potentially serve as novel heat carriers to enhance the thermal performance in micro- and nanoscale devices. We study the condition of SPhPs existing in a dielectric submicron film with a broad frequency range. The calculation of SPhPs thermal conductivity based on Boltzmann transport equation (BTE) demonstrates that the heat flux carried by SPhPs exceeds the one carried by phonons. We also conduct a time-domain-thermal-reflectance (TDTR) measurement of *SiN* submicron films and demonstrate that the thermal conductivity due to the SPhPs at high temperatures increases by decreasing the film thickness. The results presented in this thesis have potential applications in the field of heat transfer, thermal management, near-field radiation and polaritonics.

Résumé

La conduction thermique devient moins efficace à mesure que la taille des structures diminue en dessous du micron, car la diffusion de surface des phonons devient prédominante et limite plus efficacement les phonons que la diffusion phonon-phonon Umklapp. Des études récentes ont indiqué que les phonon polaritons de surface (SPhPs), qui sont les ondes électromagnétiques évanescentes générées par l'hybridation des phonons optiques et des photons et se propagent à la surface d'une surface diélectrique polaire, pourraient servir de nouveaux vecteurs de chaleur pour améliorer les performances thermiques dans des dispositifs micro- et nano-métriques. Nous étudions l'état des SPhPs existant dans un film submicronique diélectrique dans une large gamme de fréquences. Le calcul de la conductivité thermique des SPhPs basé sur l'équation de transport de Boltzmann (BTE) montre que le flux de chaleur transporté par les SPhPs est supérieur à celui des phonons. Nous effectuons également une mesure de réflectance thermique dans le domaine temporel (TDTR) de films submicroniques de *SiN* et démontrons que la conductivité thermique due aux SPhPs à haute température augmente lorsque l'épaisseur du film diminue. Les résultats présentés dans cette thèse ont des applications potentielles dans le domaine du transfert de chaleur, de la gestion thermique, du rayonnement en champ proche et de la polaritonique.

Contents

Abstract	v
Résumé	vii
I Introduction	1
1 Macro- and Nanoscale heat conduction	3
1.1 Thermal conduction at macroscales and at nanoscales	3
1.2 Surface phonon polariton fundamental concept and applications.	7
1.3 Thermoelectric systems and Phononic Crystals	11
1.4 Outline of this work	15
II Surface Phonon Polaritons	17
2 Contribution of Surface Phonon Polaritons to Thermal Properties in Ultra-Thin Films	19
2.1 Introduction	19
2.2 Surface electromagnetic waves	20
2.3 Suspended dielectric thin film surrounded by the same media $\epsilon_1 = \epsilon_3$	24
2.4 Dielectric constant and dispersion relation of SiN films	26
2.5 Calculation of the dispersion relation and the mean free path of surface modes in SiN film	27
2.6 SPhPs thermal conductivity	30
2.7 Survey of experimental thermal conductivity values of SiN con- tributed by phonons	34
2.8 Conclusion	35
3 Sample fabrication	37
3.1 Sample preparation	37
3.2 EB lithography and patterns design	38
3.3 PVD deposition and SEM characterization	39

3.4	Conclusion	41
4	Thermal characterization	43
4.1	Thermal decay measurement with TDTR	43
4.2	Correction with the TDTR signal	44
4.3	Extraction of the thermal conductivity from the numerical model	46
4.4	Conclusion	49
5	Results and discussion	51
5.1	Results of low temperature thermal conductivity measurements	51
5.2	Results of high temperature thermal conductivity measurements	52
5.3	Discussion	53
5.4	Conclusion	57
III Investigation of phonon transport in nanostructured thin films: Phononic Crystals and Thermoelectric Alloys		59
6	Introduction of Phononic Crystals	61
6.1	Phononic Crystals: heat conduction and heat convection	61
6.2	Analytical model for heat dissipation by conduction and convection	63
6.3	Conclusion	67
7	Fabrication and thermal characterization of porous membrane	69
7.1	Sample design and fabrication	69
7.2	Thermal characterization by two-laser Raman thermometry . .	70
7.3	Conclusion	72
8	Determining the Phononic Crystal thermal properties	75
8.1	Setting the PnC thermal conductivity parameters in vacuum . .	75
8.2	Setting the PnC thermal convection parameters in air	76
8.3	Discussion	77
8.4	Conclusion	80
9	Photothermal Radiometry	83
9.1	Introduction	83
9.2	Heat propagation in layered samples	86
9.3	Conclusion	92
10	$Bi_2Te_xSe_{3-x}$ nanostructured film synthesis and thermal characterization	93
10.1	Synthesis method of $Bi_2Te_xSe_{3-x}$ alloy films	93
10.2	Photothermal characterization of $Bi_2Te_xSe_{3-x}$ alloy films . . .	94
10.3	Conclusion	96

CONTENTS

xi

Conclusion

99

References

105

Index

107

List of Figures

1.1	Schematic representation of an object with cross section A and length L heated from the left side and cooled down from the right side. Heat transport in this object is diffusive due to the fact that the phonon mean free path is much smaller than the characteristic length L	4
1.2	Diffusive and ballistic transport regime: when the characteristic length of an object is longer than the phonon mean free path, the phonon transport is diffusive, and when the characteristic length is shorter than the phonon mean free path, the phonon transport is ballistic (Nomura (2016)).	4
1.3	(left) Phonon dispersion curves of bulk silicon: longitudinal acoustic modes (red curve) and transversal acoustic modes (blue curve). (right) Density of states of bulk silicon (black curve).	6
1.4	Calculated phonon dispersion: (a) in bulk silicon crystal. (b) in wurtzite GaN film with the thickness of layers: 4 nm / 2 nm / 4 nm Pokatilov, Nika, and Balandin (2004). (c) in GaN nanowires with the core radius $R_1 = 6nm$ and the coating radius $R = 10nm$ Pokatilov, Nika, and Balandin (2005b). (d) Phonon group velocity in GaN nanowires without (red curve) and with soft (green curve) and hard (blue) surface coating, GaN nanowire with acoustically fast AlN barriers of the 4nm \times 6nm and 2nm \times 3nm GaN nanowire cross sections Pokatilov, Nika, and Balandin (2005a).	6
1.5	Schematic illustration of a thermophotovoltaic converter, which uses solar photons to heat up an intermediate selective absorber, in order to re-emit photons near the bandgap of a PV cell: (a) the frequency spectra of solar energy; (b) selective absorbance spectra of the absorber; (c) selective emission spectra at the emitter; (d) photovoltaic cell absorption spectra (Baxter, Bian, Chen, Danielson, Dresselhaus, Fedorov, Fisher, Jones, Maginn, Kortshagen, Manthiram, Nozik, Rolison, Sands, Shi, Sholl, and Wu (2009)).	8

1.6	Energy density calculated at different distance from the surface of an amorphous silicon plate in vacuum. When the distance scales from 100 μm to 100 nm, the energy density increase by 5 orders of magnitude at the frequency close to 100 THz (Joulain, Mulet, Marquier, Carminati, and Greffet (2005)).	8
1.7	(left) Thermal conductance between a silica sphere and a silica plate versus the sphere-plane separation. The thermal conductance increases three times when the separation scales from 2500 nm to 30 nm. (right) Schematic illustration of the experimental setup (Rousseau, Siria, Jourdan, Volz, Comin, Chevrier, and Greffet (2009)).	9
1.8	The dispersion curve of bulk phonon polaritons in GaP (Yu and Cardona (2010))	10
1.9	Schematic illustration of Surface Phonon Polaritons excited at the interface of a polar dielectric and air.(Gluchko, Palpant, Volz, Braive, and Antoni (2017))	11
1.10	Distribution of wasted thermal energy. Data is obtained from prometeon.com	12
1.11	Thermoelectric device consisting of vertical thermoelectric modules. The hot side from the top and the cold side from the bottom generate a temperature gradient and generate a voltage difference in the electrical circuit (Von Lukowicz, Abbe, Schmiel, Tajmar, von Lukowicz, Abbe, Schmiel, and Tajmar (2016)). . .	12
1.12	Figure of merit ZT of current state of the art thermoelectric materials versus temperature (Minnich, Dresselhaus, Ren, and Chen (2009)).	13
1.13	Normalized thermoelectric properties and ZT figure of merit values versus doping concentration at 300 K for n-type $\text{Si}_{0.8}\text{Ge}_{0.2}$, where S is the seebeck coefficient, k represents the thermal conductivity and σ refers to the electrical conductivity (Minnich, Dresselhaus, Ren, and Chen (2009)).	14
1.14	SEM images of structures for different lattice sizes and patterns (scale bars are 300 nm in length) (Anufriev, Maire, and Nomura (2016))	15
1.15	Thermal conductivity of a nanobeam as a function of diameter of aluminium pillars. (insight) The TEM image of a nanobeam and pillars (Anufriev, Yanagisawa, and Nomura (2017)).	15
2.1	Two types of phonon modes in crystalline structure: (up) acoustic phonons, where the movement of atoms is in phase and (down) optical phonons, where the movement of atoms is out-of-phase. Optical phonons can be excited by electromagnetic waves.	20

2.2	Schematic of a system consisting of two media, which are separated by a plane interface. ϵ_1 and ϵ_2 refer to dielectric functions in medium 1 and medium 2, respectively.	21
2.3	Schematic of a system consisting of three media, which are separated by two interfaces at $z=0$ and $z=d$, where d is the thickness of the second medium. ϵ_1 , ϵ_2 and ϵ_3 refer to the dielectric function in medium 1, medium 2 and medium 3, respectively.	24
2.4	Real and imaginary parts of the dielectric function of silicon nitride constructed with Equation 2.31 and the fitting parameters of Table 2.1.	27
2.5	Comparison of dispersion relation of the SiN-air single interface (yellow line) and light (blue line). The dispersion curve presented here are considered the absorption by the SiN material.	28
2.6	Dispersion relation of SPhPs in a suspended SiN membrane with symmetrical surroundings ($\epsilon_1=\epsilon_3=1$). The calculation is based on three thicknesses: $d=2 \mu\text{m}$ (blue line), $d=1 \mu\text{m}$ (yellow line) and $d=100 \text{ nm}$ (green line).	28
2.7	Imaginary part of wavevector as a function of frequency for a suspended SiN membrane in symmetrical surroundings ($\epsilon_1=\epsilon_3=1$). The calculation is based on three different thicknesses film: $d=200 \text{ nm}$ (blue curve), $d=100 \text{ nm}$ (yellow curve) and $d=50 \text{ nm}$ (green curve).	29
2.8	Mean free path of SPhPs as a function of frequency for a suspended SiN membrane with symmetrical surroundings ($\epsilon_1=\epsilon_3$). The calculation is based on three thicknesses: $d=200 \text{ nm}$ (blue line), $d=100 \text{ nm}$ (yellow line) and $d=50 \text{ nm}$ (green line).	30
2.9	Schematic view of a film with thickness d , width L_x and length L_y . The z -axis is chosen to be perpendicular to the film, while the x -axis and y -axis are parallel to the in-plane direction. Temperature difference is applied on the two sides of the film, which leads to a heat flux following the temperature gradient and propagating along the y -axis.	31
2.10	Thermal conductivity contributed by SPhPs as a function of temperature in a SiN film for four different thicknesses.	33
2.11	SiN thin film thermal conductivity contributed by SPhPs as a function of thickness and for three different temperatures.	34

2.12	Thermal conductivity of amorphous SiN films as a function of thickness. These experimental results are obtained at room temperature. No thickness dependence is observed by Griffin Jr, Brotzen, and Loos (1994) (green dots) on 60 nm to 8.5 μm thick films or by Mastrangelo, Tai, and Muller (1990) (pink dots) on 2 - 5 μm thick films. Lee and Cahill (1997) reported that from 200 nm film to 250 nm thicknesses, the increase in thermal conductivity is less than 30 %. However, a surprising jump around 200 nm is noticed. Queen and Hellman (2009) indicated an increase of 2.5 W/m/K between the 50 nm thick film to the 200 nm thick one.	35
3.1	Schematic of a SiN membrane fabrication process: firstly, 320 nm thick EB resist is spun on the top of the suspended film; secondly, circular patterns are drawn by electron beam lithography and then an aluminum layer is deposited by physical vapor deposition; finally, the EB resist is removed by the ZD-MAC resist remover.	37
3.2	EB lithography machine (model: JBX-6300FS) from JEOL company, which can easily write patterns down to 8 nm or less (actual result: 5 nm) by the employment of an electron optical system that automatically adjusts a 2.1 nm-diameter electron beam at a 100 kV accelerating voltage.	38
3.3	GDS pattern for EB lithography. (a) Five metal strips per side for mask alignment. (b) square lattice metal pads are drawn for EB lithography. The length of the side of a square in (a) is 200 μm and in (b) is 50 μm	39
3.4	Electron-beam physical vapor deposition: (a) view from outside, PVD machine consists of a vacuum chamber and a control panel; (b) view from inside, where a sample holder is attached in the top of the vacuum chamber, the sputtering target is placed at the bottom and is evaporated by EB during the process, a shelter is placed between the sample holder and the target to switch on/off the process; (c) SiN membranes are fixed on a sample holder by metal strips.	40
3.5	SEM image of a SiN membrane after fabrication: (a) top view showing that the aluminum pads have a diameter of 5 μm ; (b) Inclined view of a metal strip showing that the aluminum layer has a thickness of 70 nm.	40
3.6	Microscopy image of the top view of a 30 nm thick SiN membrane with aluminium pads.	41

4.1 (a)Schematic of the TDTR setup: the sample is placed in a cryostat with temperature controlled by an helium flow or a heating stage; a pump laser is periodically heating up the aluminum pads on the sample and a probe laser is continuously measuring the reflectance of the aluminum pads by monitoring the intensity of the reflected beam in the photodetector; a lamp and a camera assist to locate the aluminum pads on the sample; (b)Normalized TDTR decay signal (red line) interpolated by an exponential decay curve (black line) (Anufriev, Yanagisawa, and Nomura (2017)). 44

4.2 (Left) TDTR signals are continuously recorded for one minute, which consist of 1000 TDTR decay curves. (Right) Single TDTR decay curve of a SiN membrane. The red dots and green discontinuous line indicate the normalized intensity of the probe and pump laser, respectively. The blue line denotes an exponential fit of the normalized intensity of the probe laser. Region A and region C correspond to the beginning and the end of a single TDTR measurement, respectively. Region B relates to the maximum intensities of a single TDTR measurement. 46

4.3 Single TDTR decay curve of a SiN membrane after the correction of offset in Figure 4.2 (right). Red dots represent the normalized signal recorded by the probe laser. Green discontinuous line indicates a single pulse of the pump laser. Blue line denotes to an exponential fit of the TDTR signal. 47

4.4 Temperature mapping of a quarter of a suspended SiN film with an Aluminum circular pad in the center as predicted by COM-SOL Multiphysics. 48

4.5 (Left) TDTR measurement compared with three decay curves predicted for different thermal conductivities using the COM-SOL model. (Right) Black dots represent the signal integral between 100 and 500 μ s of selected curve versus thermal conductivity, whereas the red lines represents a polynomial function interpolating the black dots. 48

5.1 Thermal conductivity as a function of temperature of four different thickness films: 30 nm (pink dots), 50 nm (blue dots), 100 nm (red dots), 200 nm (black dots) in a temperature range of 4 K to 300 K. 52

5.2 Thermal conductivity as a function of temperature of four different film thicknesses: 30 nm (pink dots), 50 nm (blue dots), 100 nm (red dots), 200 nm (black dots) in a temperature interval ranging from 300 K to 600 K. 53

5.3	Comparison between the analytical model and the experimental results of the SPhPs contribution to thermal conductivity as a function of temperature. Continuous lines represent the calculation from theoretical model with four different thicknesses: 30 nm (pink line), 50 nm (blue line), 100 nm (red line) and 200 nm (black line). The solid dots stand for the experimental results of four different thicknesses: 30 nm (pink triangle), 50 nm (blue square), 100 nm (red circle) and 200 nm (black triangle). A bar break at 6 W/m/K at the vertical axis should be noticed and it assists to visualize our analytical model of the 50 nm and the 30 nm thick film.	55
5.4	Normalized thermal conductivity of the experimental results as a function of temperature. The solid dots stand for the experimental results of four different thicknesses: 30 nm (pink triangle), 50 nm (blue square), 100 nm (red circle) and 200 nm (black triangle).	56
6.1	Phonon mean free path spectra of silicon at room temperature: longitudinal acoustic modes (blue line) and transversal acoustic modes (red line).	61
6.2	Temperature map in two dimensional phononic crystal simulated by COMSOL Multiphysics. A continuous laser applied on the Aluminium pad to generate heat propagating along the phononic crystal into the heat sink. The coloured bar (with unit in kelvin) indicates the temperature in the whole structure.	62
6.3	Schematic of the modelled cylinder system. r refers to the radial distance, θ is the polar angle, and ϕ is the azimuthal angle in spherical coordinate.	63
6.4	Phonon scattering in PnCs is contributed by three processes: phonon-phonon scattering Λ_{P-P} , phonon-hole scattering Λ_{H-P} and surface-phonon scattering Λ_{S-P}	65
7.1	(a) SEM image with a scale bar of 20 μm in length and (b) insight. The disk with thickness t is patterned with square lattice holes with diameter d , neck distance n and periodicity a (Graczykowski, El Sachat, Reparaz, Sledzinska, Wagner, Chavez-Angel, Wu, Volz, Wu, Alzina, and Sotomayor Torres (2017)).	70
7.2	The two-laser Raman thermometry calibration. (a) Temperature versus the silicon longitudinal optical phonon frequency. (b) Raman shift due to the temperature increases.	71

7.3 Schematic of the Raman thermometer: a heating laser with wavelength 405 nm continuously heats up the center of the sample, meanwhile a probe laser with wavelength 488 nm simultaneously scans the sample surface in the in-plane direction. The probe laser has low intensity and only heats up the sample within 5 kelvins and the reflected signal is guided into the Raman spectrometer to detect the temperature vibrational modes. This measurement can be performed in vacuum or in ambient conditions (Graczykowski, El Sachat, Reparaz, Sledzinska, Wagner, Chavez-Angel, Wu, Volz, Wu, Alzina, and Sotomayor Torres (2017)). 71

7.4 Two-laser Raman thermometry result of PnC1 sample: measurement in vacuum (red circle) and in air (blue circle). 72

8.1 Experiment vs. model fitting results: (a) 250 nm thick silicon membrane; (b) sample PnC1 with lattice parameter of $a = 300$ nm and hole diameter of $d = 135$ nm; (c) sample PnC2 with lattice parameter of $a = 250$ nm and hole diameter of $d = 110$ nm; (d) sample PnC3 with lattice parameter of $a = 300$ nm and hole diameter of $d = 130$ nm. The red circles represent experimental data measured in vacuum and black lines represent our analytical model. 76

8.2 Experiment vs. model fitting results including air convection: (a) 250 nm thick silicon membrane; (b) sample PnC1 with lattice parameter of $a = 300$ nm and hole diameter of $d = 135$ nm; (c) sample PnC2 with lattice parameter of $a = 250$ nm and hole diameter of $d = 110$ nm; (d) sample PnC3 with lattice parameter of $a = 300$ nm and hole diameter of $d = 130$ nm. The blue circles represent experimental data measured in air and black lines represent our analytical model. 77

8.3 Thermal conductivities of a 250 nm thick silicon membrane and three phononic crystals as a function of temperature. Temperature dependence is weaker for the phononic crystal with smaller neck distance. 78

8.4 Heat transfer coefficient of a 250 nm thick silicon membrane (black cross) and three types of phononic crystals: PnC1 with lattice parameter $a = 300$ nm and hole diameter $d = 135$ nm (blue cross); PnC2 with lattice parameter of $a = 250$ nm and hole diameter $d = 110$ nm (red cross); PnC3 with lattice parameter $a = 300$ nm and hole diameter $d = 130$ nm (green cross). 79

8.5 Convective heat loss in percentage as a function of neck distance (blue discontinuous line) and of volume reduction factor (red discontinuous line). 80

9.1	Diagram of the PTR experimental setup developed in the EM2C laboratory.	84
9.2	Radial profile of the laser beam intensity measured by Thorlab photodiode.	85
9.3	Calibration of the PTR phase signal with a 0.5 mm thick stainless steel sample.	85
9.4	Amplitude and phase of the radiative thermal waves as a function of modulated frequency, for four different samples: Stainless Steel (red); Vitreous Carbon (green); Silver (blue); Copper (black). The verticle dotted lines refer to the critical frequencies.	88
9.5	PTR signal as a function of the modulated frequency based on a 0.5 mm thick stainless steel sample with no deposition (red line); with 1 μm (blue line), 10 μm (green line) and 100 μm (black line) thick gold film deposition.	91
10.1	Schematic of the synthesis process.	94
10.2	SEM images of disk-shaped of $Bi_2Te_{2.85}Se_{0.15}$ (Bude (2018)).	94
10.3	Analogical schematic of disk-shaped nanograins after pressing and drying. The thickness of the nanograins averages 10 nm. And the porosity of the pressed sample is approximately 0.1.	95
10.4	Amplitude of PTR signal (blue circle) compared to the theoretical prediction (red curve) of $Bi_2Te_{2.85}Se_{0.15}$ alloy film. The inset figure highlights a calibration of the amplitude of the PTR signal of a 0.5 mm thick stainless steel.	96
10.5	Amplitude of PTR signal compared to the theoretical prediction of Bi_2Te_3 , $Bi_2Te_{1.5}Se_{1.5}$ and Bi_2Se_3 alloy film.	97

Part I

Introduction

Chapter 1

Macro- and Nanoscale heat conduction

In this chapter, we briefly review the concept of phonon transport in macroscale and microscale. By nanostructuring, the phonon mean free path and dispersion curves can be tailored and therefore satisfy the requirement of specific applications.

1.1 Thermal conduction at macroscales and at nanoscales

1.1.1 Diffusive and ballistic heat conduction

Thermal conductivity reflects the ability of conducting heat in macroscale objects. This quantity relates the total heat flow and the the temperature gradient in the direction of thermal conduction. It was first formulated by Jean Baptiste Joseph Fourier in 1822 ([Joseph \(1822\)](#)) who concluded that "the heat flux resulting from thermal conduction is proportional to the magnitude of the temperature gradient and opposite to its sign":

$$\vec{j} = -\kappa \vec{\nabla}T, \quad (1.1)$$

where \vec{j} is the heat flux density, $\vec{\nabla}T$ is the temperature gradient, and κ the thermal conductivity. The Fourier's law can be combined with the energy conservation into spatial and temporal description:

$$\frac{\partial T}{\partial t} = \frac{\kappa}{\rho C_p} \Delta T, \quad (1.2)$$

where ρ is mass density and C_p is specific heat.

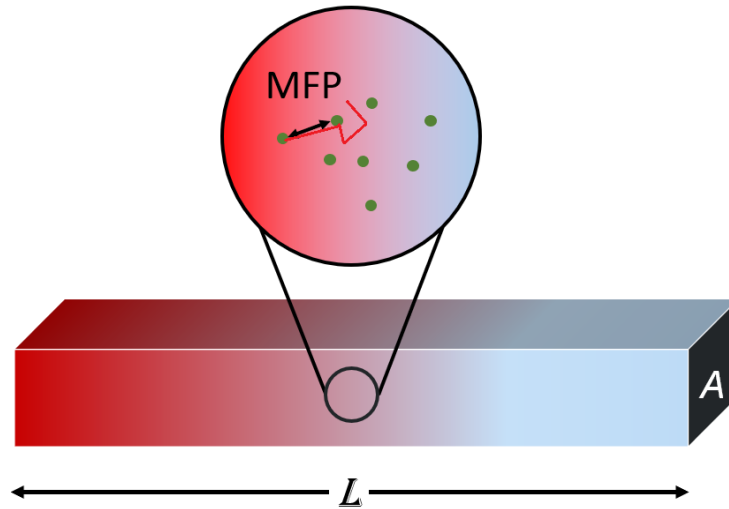


Figure 1.1: Schematic representation of an object with cross section A and length L heated from the left side and cooled down from the right side. Heat transport in this object is diffusive due to the fact that the phonon mean free path is much smaller than the characteristic length L .

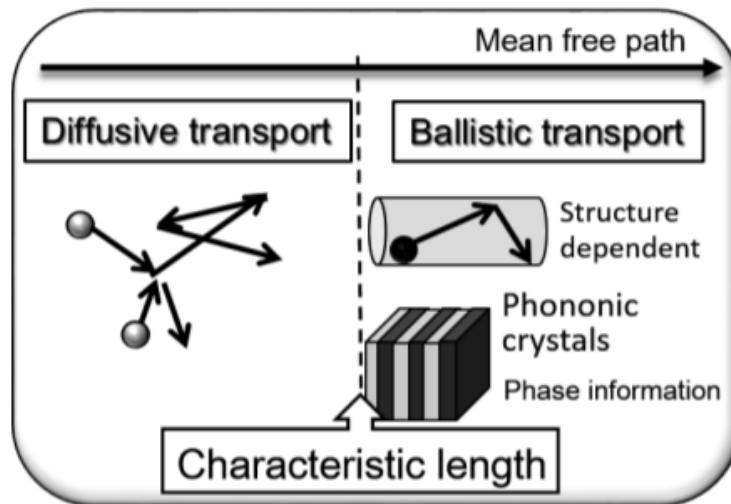


Figure 1.2: Diffusive and ballistic transport regime: when the characteristic length of an object is longer than the phonon mean free path, the phonon transport is diffusive, and when the characteristic length is shorter than the phonon mean free path, the phonon transport is ballistic (Nomura (2016)).

Phonon transport behaves differently when the system size scales down. Phonon mean free path describes the average distance that a phonon travels before it collides another phonon. In bulk materials, i.e. when the characteristic length of the structure is larger than the phonon mean free path, the phonon transport

is diffusive. When the phonon mean free path (MFP) is much shorter than the characteristic length L of the object, the phonon transport is diffusive. This mechanism can be analysed by the kinetic thermal conductivity as follows:

$$\kappa = \frac{1}{3}C\nu_s\Lambda_{ph}, \quad (1.3)$$

where C is the volumetric specific heat, ν_s is group velocity of phonon and Λ is average phonon mean free path.

Phonons can be scattered during propagation in a bulk material, those scattering events includes Umklapp phonon-phonon scattering, phonon-impurity scattering, phonon-electron scattering and phonon-boundary scattering. These four scattering processes can be combined using Matthiessen's law:

$$\frac{1}{\tau_C} = \frac{1}{\tau_U} + \frac{1}{\tau_I} + \frac{1}{\tau_{ph-e^-}} + \frac{1}{\tau_B}, \quad (1.4)$$

where τ_C is the combined relaxation time of phonon scattering processes, τ_U refers to the relaxation time of Umklapp phonons scattering, τ_I is the relaxation time of phonon-impurity scattering, τ_{ph-e^-} corresponds to the relaxation time of phonon-electron scattering and τ_B denotes the relaxation time of phonon-boundary scattering. In bulk materials, phonons are scattered mainly through Umklapp phonon-phonon scattering, whereas in small structures, phonons are mostly scattered by phonon-boundary scattering.

1.1.2 Wave effects in heat transport

Thermal conduction becomes less efficient as structures scale down into sub-micron sizes since phonon-boundary scattering becomes predominant and impede phonons more efficiently than Umklapp scattering (Cahill et al. (2003) Goodson (1996) Zeng and Chen (2001)). Therefore, thermal management becomes more challenging in micro-electronic or optical devices (Biswas et al. (2012) Cahill et al. (2003) Dusastre (2011) Volz et al. (2016) Volz et al. (2016)).

Dispersion relation of phonons of bulk silicon is shown in figure 1.3 as well as the calculated density of states. Dispersion curves consists of acoustic (in-phase) and optical (out-of-phase) "branches". Often, acoustic phonons are the major heat carriers, whereas optical phonons contribute very little to thermal transport, except indirectly in their interactions with acoustic phonons. Optical phonons have flatter branches compared to acoustic phonons, resulting in their low group velocity, which limits the contribution by optical phonon to thermal transport.

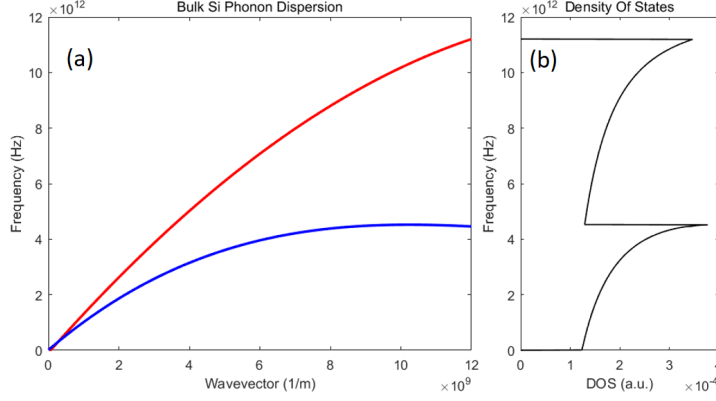


Figure 1.3: (left) Phonon dispersion curves of bulk silicon: longitudinal acoustic modes (red curve) and transversal acoustic modes (blue curve). (right) Density of states of bulk silicon (black curve).

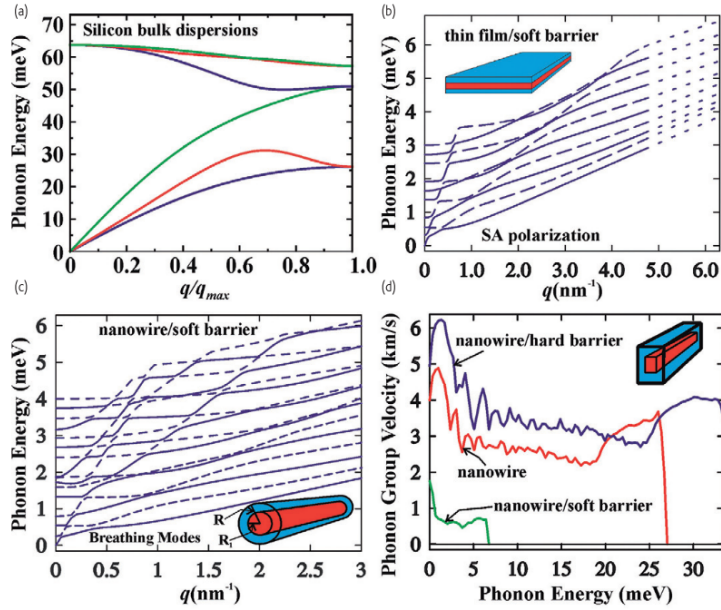


Figure 1.4: Calculated phonon dispersion: (a) in bulk silicon crystal. (b) in wurtzite GaN film with the thickness of layers: 4 nm / 2 nm / 4 nm Pokatilov et al. (2004). (c) in GaN nanowires with the core radius $R_1 = 6\text{nm}$ and the coating radius $R = 10\text{nm}$ Pokatilov et al. (2005b). (d) Phonon group velocity in GaN nanowires without (red curve) and with soft (green curve) and hard (blue) surface coating, GaN nanowire with acoustically fast AlN barriers of the 4nm x 6nm and 2nm x 3nm GaN nanowire cross sections Pokatilov et al. (2005a).

For the structure with characteristic length larger than phonon wavelength, phonons transport is based on the bulk phonon modes in materials without in-

interacting with boundary. Instead when the structure with characteristic length comparable or smaller than phonon wavelength, confinement effect occurs and modified phonon dispersion should be taken into account. The interaction between phonon and boundary increases, which leads the modification of the dispersion curves. Furthermore, the dispersion relations can be tailored by nanostructuring at low dimensions to satisfy targeted material properties for specific applications. [Balandin and Nika \(2012\)](#) described several methods to modify the phonon dispersion by surface coating in low-dimensional materials, as exemplified in figure 1.4.

As shown in equation 1.3, thermal conductivity is proportional to group velocity which can be deduced from the derivation of the dispersion curves. Therefore, it is achievable to tailor the thermal conductivity through mode confinement in dispersion curves.

1.2 Surface phonon polariton fundamental concept and applications.

Over the past few years, significant research efforts have been devoted to the study of surface waves, due to the fact that the surface effects predominate over the volumetric ones when the high surface-to-volume ratio increases in nanomaterials. Moreover, the investigation of surface waves encouraged considerable potential applications, such as the ones related to the improvement of the thermal performance and stability of micro- and nanoelectronics ([Chen and Chen \(2010\)](#) [Chen and Chen \(2007\)](#) [Mulet et al. \(2001\)](#)), thermophotovoltaics ([Baxter et al. \(2009\)](#)), infrared microscopies, surface wave guiding, phase-changed materials ([Staude and Rockstuhl \(2016\)](#)), heat assisted magnetic recording or heat assisted lithography ([Rousseau et al. \(2009\)](#)).

Thermophotovoltaic (TPV) systems satisfy the requirement of providing the amount of energy needed on a reduce space scale and time frame with minimal impact on the environment. It was firstly proposed by Kenry Kolm at MIT in 1956 and further developed by Pierre Aigrain in 1960. A TPV generally consists of a thermal emitter and a photovoltaic diode cell and it converts directly heat into electricity via photons. As shown in figure 1.5, the TPV cells uses solar photons to heat up an intermedia selective absorber in order to re-emit photons near the bandgap of a PV cell.

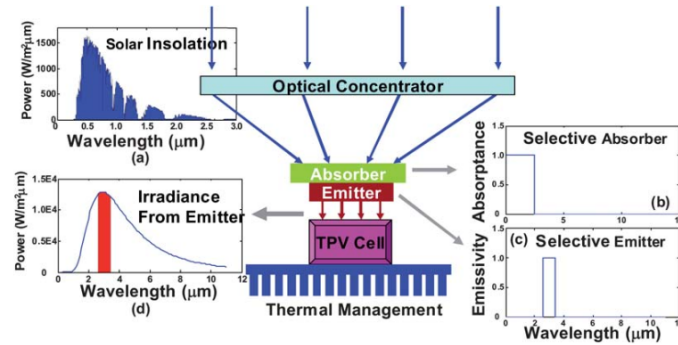


Figure 1.5: Schematic illustration of a thermophotovoltaic converter, which uses solar photons to heat up an intermediate selective absorber, in order to re-emit photons near the bandgap of a PV cell: (a) the frequency spectra of solar energy; (b) selective absorptance spectra of the absorber; (c) selective emission spectra at the emitter; (d) photovoltaic cell absorption spectra (Baxter et al. (2009)).

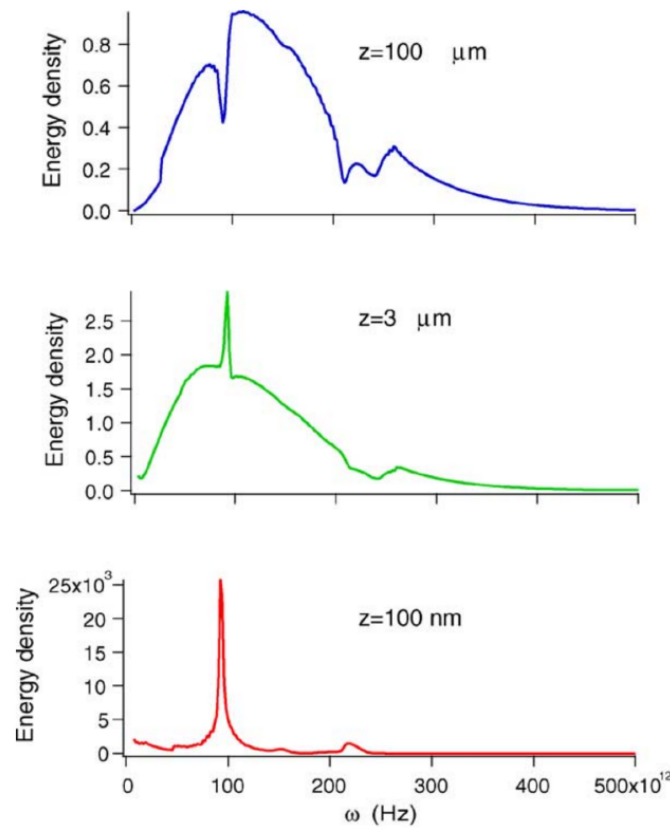


Figure 1.6: Energy density calculated at different distance from the surface of an amorphous silicon plate in vacuum. When the distance scales from $100 \mu\text{m}$ to 100 nm , the energy density increase by 5 orders of magnitude at the frequency close to 100 THz (Joulain et al. (2005)).

Such systems have a theoretical maximum efficiency of 85.4%, which is comparable to that of infinite multijunction cells (86.8%). A monochromatic irradiance from the emitter is essential to improve the conversion efficiency in TPV systems.

Planck's radiation law, firstly formulated in 1900 by Max Planck, describes the spectral-energy distribution of radiation emitted by a blackbody. Joulain et al. (Joulain et al. (2005)) demonstrated the existence of a near-field monochromatic radiation between a SiO₂ surface heated up to 300 K and a vacuum at 0 K, as illustrated in figure 1.6.

Heat can be exchanged between two surfaces through emission and absorption of thermal radiation. Rousseau, Siria, Jourdan, Volz, Comin, Chevrier, and Greffet (2009) measured the thermal conductance for gaps varying between 2.5 μm to 30 nm and demonstrated that the sphere-plane conductance increased from 6 to 18 nWK⁻¹, as shown in figure 1.7.

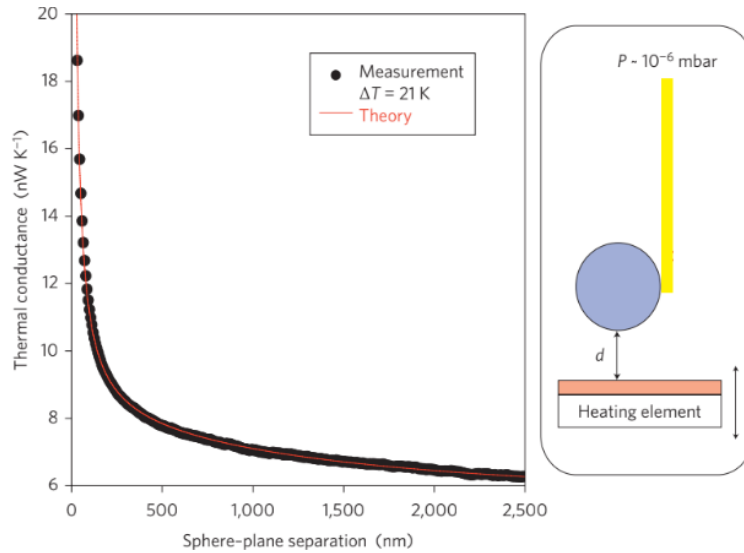


Figure 1.7: (left) Thermal conductance between a silica sphere and a silica plate versus the sphere-plane separation. The thermal conductance increases three times when the separation scales from 2500 nm to 30 nm. (right) Schematic illustration of the experimental setup (Rousseau et al. (2009)).

A polariton is a particle resulting from the coupling of photons with another quasiparticle. Three types of coupling have been investigated theoretically and experimentally to date: Tolpygo obtained the coupled states of electromagnetic waves and phonons in ionic crystals and their dispersion relation in 1950 (Tolpygo (1950)), those states were later found by Huang independently in 1951 (Huang (1951)). This coupling particle is now known as phonon polaritons. Otto discovered the existence of surface plasmon-polaritons in silver by the method of frustrated total reflection in 1968 (Otto (1968)). The stable

Frenkel exciton-polaritons at room temperature was observed by Giovanni Lerario in 2016 (Lerario et al. (2017)).

The frequency spectra of polaritons ranges from hundreds of gigahertz to several terahertz, which matches the frequency gap between electronics and photonics. This property fits diverse applications such as signal processing and spectroscopy (Feurer et al. (2007)), ultrafast optical switches (Thi Ha et al. (2017)), ultralow threshold polariton lasers (Zamfirescu et al. (2002)) and light emitting diodes (Tsintzos et al. (2008)).

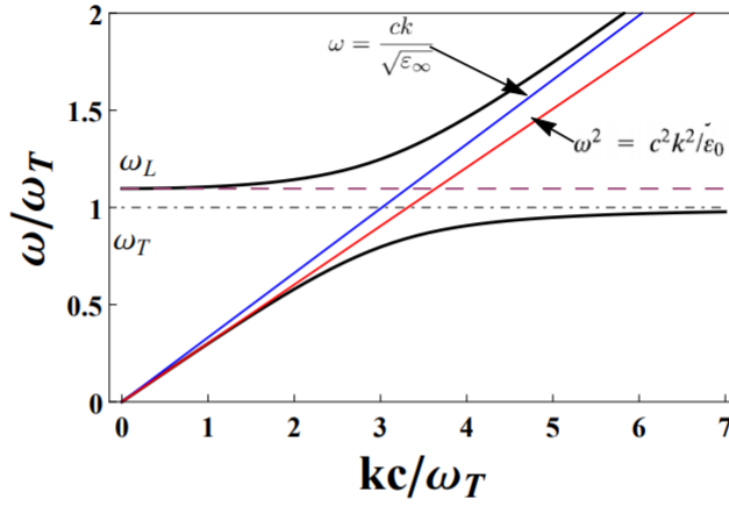


Figure 1.8: The dispersion curve of bulk phonon polaritons in GaP (Yu and Cardona (2010))

Surface phonon polaritons are evanescent electromagnetic surface waves coupled with optical phonons and propagate along the interface of a polar medium (such as SiO₂ (Gluchko et al. (2017)) or SiN) and a dielectric one.

The surface phonon-polaritons contribution to in-plane thermal conductivity of a nano thin film of silicon nitride is investigated based on the Maxwell equations and the Boltzmann transport equation. To calculate the thermal conductivity contributed by surface phonon polaritons, the work from Chen and, later, Ordonez proposed a theoretical approach (Chen et al. (2005a) Ordonez-Miranda et al. (2013)):

$$\lambda_{SPhPs} = \frac{1}{4\pi d} \int_{\omega_L}^{\omega_H} \hbar\omega \Lambda \beta_R \frac{\partial f_0}{\partial T} d\omega. \quad (1.5)$$

where λ_{SPhPs} the thermal conductivity contributed by surface phonon polaritons, d the thickness of the film, f_0 the Bose-Einstein distribution function, T

temperature of the film, β_R the real part of the wave vector along the in-plane axis, Λ the mean free path of the surface phonon polaritons, \hbar the Plancks constant divided by 2π , and ω_H and ω_L the highest and lowest cutoff frequencies of the surface phonon polaritons, respectively. These two frequencies are associated with the frequency region where the real part of the dielectric function is smaller than -1.

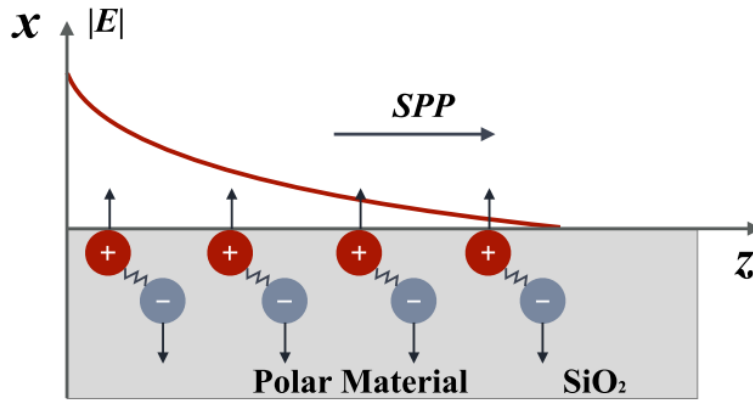


Figure 1.9: Schematic illustration of Surface Phonon Polaritons excited at the interface of a polar dielectric and air. (Gluchko et al. (2017))

1.3 Thermoelectric systems and Phononic Crystals

To date, stastical data demonstrates that only 34 % of the energy produced by fossil fuel burning or nuclear fission power plant is used, whereas 66 % is lost in the form of wasted heat. In the past few decades, more and more efforts targeted recovering the wasted heat into electricity by using thermoelectric devices.

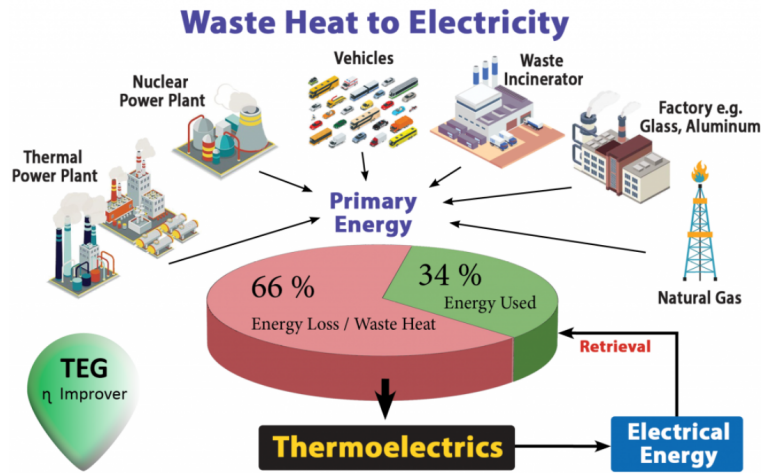


Figure 1.10: Distribution of wasted thermal energy. Data is obtained from *prometeon.com*

A thermoelectric device converts temperature gradient directly into electrical energy due to the Seebeck effect, discovered firstly in 1821 by Thomas Johann Seebeck. A conventional thermoelectric device (see in figure 1.11) consists of two separated bridges with n-doped and p-doped semiconductors. One electrode is used to connect the bridges to the hot side, whereas two electrodes separately connect the bridges to the cold side. A temperature gradient is formed inside both bridges and drive the charge carriers from the hot side to the cold side, resulting in a voltage difference in the electrical circuit.

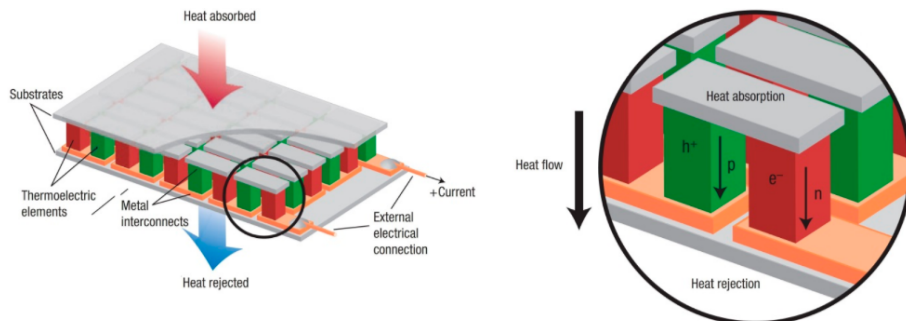


Figure 1.11: Thermoelectric device consisting of vertical thermoelectric modules. The hot side from the top and the cold side from the bottom generate a temperature gradient and generate a voltage difference in the electrical circuit (Von Lukowicz et al. (2016)).

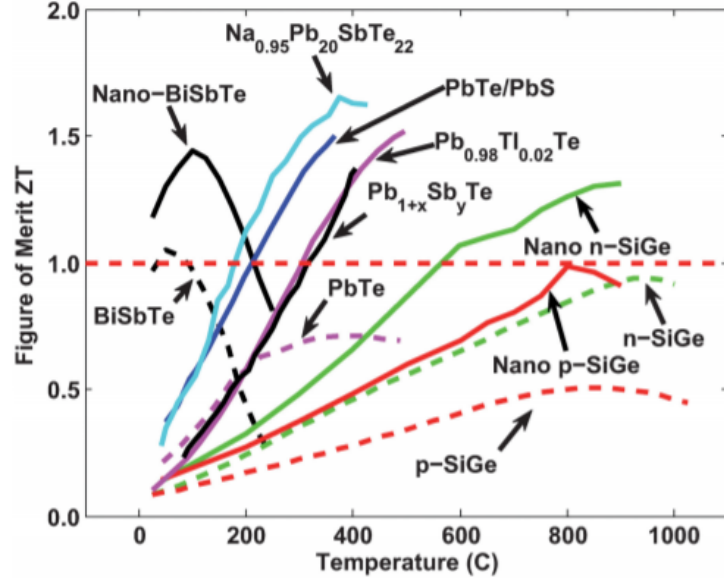


Figure 1.12: Figure of merit ZT of current state of the art thermoelectric materials versus temperature (Minnich et al. (2009)).

The ability of a given material to efficiently produce thermoelectric power is related to a dimensionless figure of merit:

$$ZT = \frac{S^2 \sigma T}{\kappa_E + \kappa_L}. \quad (1.6)$$

where S is the Seebeck coefficient, σ is the electrical conductivity and κ_E and κ_L are the thermal conductivity of electrons and phonons, respectively. The product of σ and S^2 is also called power factor. Materials with a high power factor can extract more energy from the temperature difference, however it does not indicate a higher efficiency in generating this energy.

It is not straightforward to maximize the ZT value by simply maximizing or minimizing one of the thermoelectric properties through modifying the doping concentration. Taking an example of n-doped $\text{Si}_{0.8}\text{Ge}_{0.2}$ (see in figure 1.13), the maximum seebeck coefficient or the maximum electrical conductivity does not lead to the maximum ZT value. However, by decreasing the thermal conductivity (contributed by electrons and phonons), the ZT value efficiently increases.

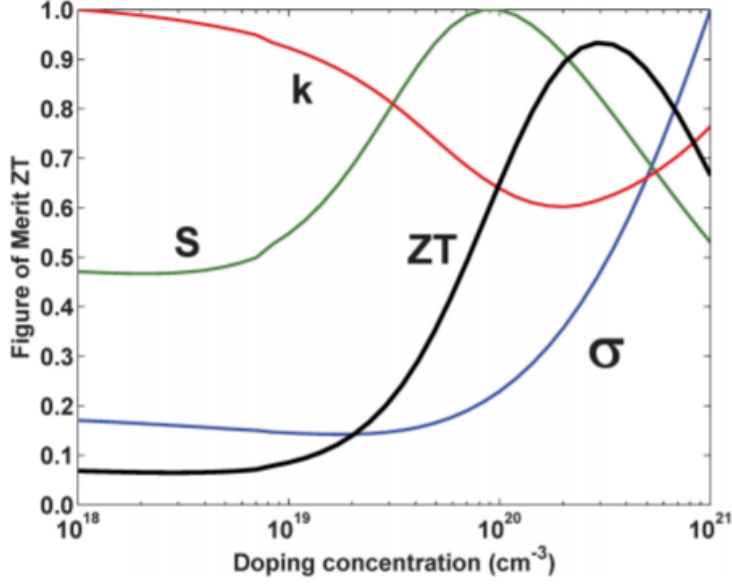


Figure 1.13: Normalized thermoelectric properties and ZT figure of merit values versus doping concentration at 300 K for n-type $\text{Si}_{0.8}\text{Ge}_{0.2}$, where S is the seebeck coefficient, k represents the thermal conductivity and σ refers to the electrical conductivity (Minnich et al. (2009)).

From the analytical point of view, the reduction of κ_E and κ_L leads to the increase of ZT value. Using the Wiedemann-Franz Law the thermal conductivity of electrons is formulated as follows:

$$\kappa_E = L\sigma T. \quad (1.7)$$

where T is absolute temperature and σ is electrical conductivity of electrons, L is the Lorentz number with the value of $2.45 \times 10^{-8} \text{W}\Omega\text{K}^{-2}$, which is generally considered as constant and depends on carrier concentration.

A promising strategy consists in maximizing the ZT value reducing lattice thermal conductivity by nanostructuring the thermoelectric materials.

One promising strategy is to reduce the phonon thermal conductivity and maintain the electrical conductivity via the artificial creation of phonon-boundary scattering as implemented in phononic crystals.

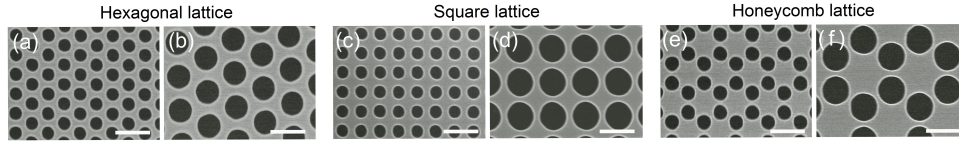


Figure 1.14: SEM images of structures for different lattice sizes and patterns (scale bars are 300 nm in length) (Anufriev et al. (2016))

Another way to reduce the thermal conductivity by nanostructuring is to place nanopillars on the surface of silicon based nanowires. Anufriev et al. (2017) experimentally demonstrated that a nanobeam with a diameter of 335 nm has 20 % lower thermal conductivity as compared to pristine nanobeams (see figure 1.15). Respectively, the aluminium / silicon intermixing layer only reduces the thermal conductivity but also may maintain the electrical conductivity.

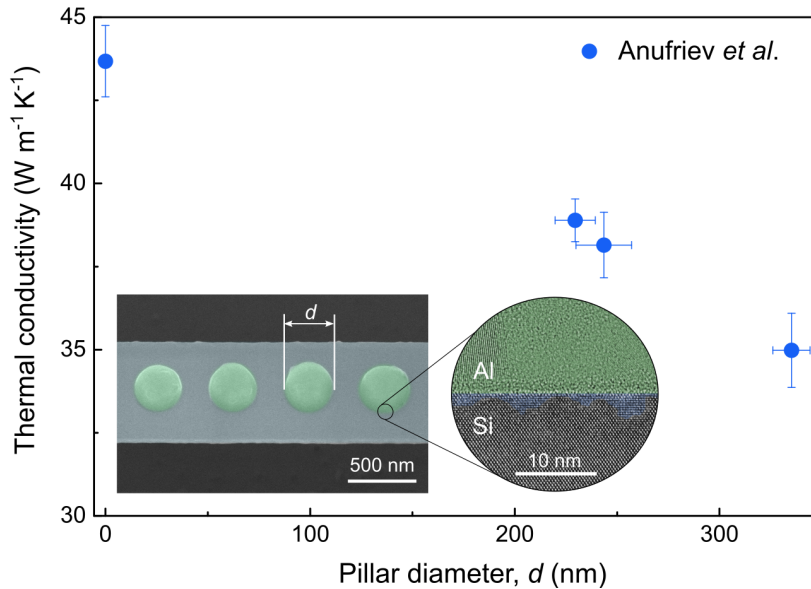


Figure 1.15: Thermal conductivity of a nanobeam as a function of diameter of aluminium pillars. (insight) The TEM image of a nanobeam and pillars (Anufriev et al. (2017)).

1.4 Outline of this work

This work is organized as follows.

In Part II, we investigate the SPhPs transport in a dielectric medium theoretically and experimentally. This part consists of Chapters 2-5. In Chapter 2, we present a theoretical approach to the excitation and propagation of SPhPs modes in a dielectric medium. The contribution of the SPhPs modes to the

thermal conduction is formulated based on the Boltzmann transport equation. The parametric study of SPhPs propagation length and its thermal conductivity is conducted for SiN. In the following chapters, we study SPhPs modes experimentally. In Chapter 3, we detail the fabrication process of metallic transducer on a suspended SiN film. In Chapter 4, we focus on the thermal conductivity measurements in the SiN films with different thicknesses. The measurement is performed at the temperatures between 4 K and 600 K. Finite element method is used to extract the thermal conductivity from the experimental data. In Chapter 5, we discuss the obtained thickness and temperature dependence of the films.

In Part III, we address the phonon transport in nanostructured thin films in the application of phononic crystals and thermoelectric alloys. This part consists of Chapters 6-10. In Chapter 6, we provide an analytical model describing the size effects on the thermal conductivity of phononic crystals including the contribution of convective losses through air. In Chapter 7, we briefly review the fabrication process of the porous silicon membranes and the two-laser Raman thermometry technique. In Chapter 8, we investigate quantitatively the heat conduction and convection in the phononic crystals using the analytical model developed in Chapter 6. In Chapter 9, we provide an overview of the photothermal radiometry technique and an analytical model based on the heat conduction in layered samples. In Chapter 10, we demonstrate the synthesis and the photothermal characterization of the $Bi_2Te_xSe_{3-x}$ ($0 \leq x \leq 3$) alloy films.

The conclusion and perspective is provided at the end of this work.

Part II

Surface Phonon Polaritons

Chapter 2

Contribution of Surface Phonon Polaritons to Thermal Properties in Ultra-Thin Films

In this chapter, we theoretically explore the potential of thermal transport contributed by surface phonon-polaritons in dielectric submicron thin films. Furthermore, amorphous silicon nitride is analytically investigated based on temperature and thickness dependencies.

2.1 Introduction

Thermal conduction becomes less efficient as structures scale down since phonon-boundary scattering becomes predominant, therefore, thermal management becomes more challenging in micro-electronic or optical devices (Biswas et al. (2012), Cahill et al. (2003), Dusastre (2011), Volz et al. (2016), Volz et al. (2016)). Here, we aim at revealing a novel heat carrier, i.e. the phonon polariton, which might be able to overcome the decrease of conventional thermal transport and even lead to its enhancement due to a surface effect. Over the past few years, significant research efforts have been devoted to the study of surface waves, due to the fact that the surface effects predominate over the volumetric ones with the high surface area/volume ratio in nanomaterials. Moreover, the investigation of surface waves encouraged considerable potential applications to improve the thermal performance and stability of nanoscale devices in electronics (Chen and Chen (2010), Chen and Chen (2007), Mulet et al. (2001)). Surface phonon polaritons are evanescent electromagnetic surface waves coupled with optical phonons and propagate along the interface of a polar medium (such as SiC or SiN) and a dielectric one (Chen et al. (2005a), Gluchko et al. (2017), Greffet et al. (2002), Ordonez-Miranda et al. (2013)). The mean free path of this evanescent wave is predicted to be in the range of hundreds of micrometers, which is significantly larger than the mean free path

of the acoustic phonons.

2.2 Surface electromagnetic waves

It is essential to picture the interaction of incident electromagnetic waves and optical phonons from the early stage. In this section, we introduce firstly the generation of optical phonons. Unlike acoustic phonons, which are treated as major heat carriers, optical phonons are often considered negligible in thermal transport, due to the fact that its slow group velocity results from its flat dispersion curve at high frequency. Nevertheless, due to the increase in surface-to-volume ratio, optical phonon located close to the surface have more chance to interact with incident electromagnetic waves. This phenomenon opens an additional channel for heat dissipation.

In a dielectric material, the bound charges can not move freely but can shift positions as a result of the presence of an electric field \mathbf{E} . A polarization is induced due the displacement and the electric displacement field \mathbf{D} is defined as follows:

where the ϵ is dielectric constant of the material and \mathbf{P} refers to the polarization density.

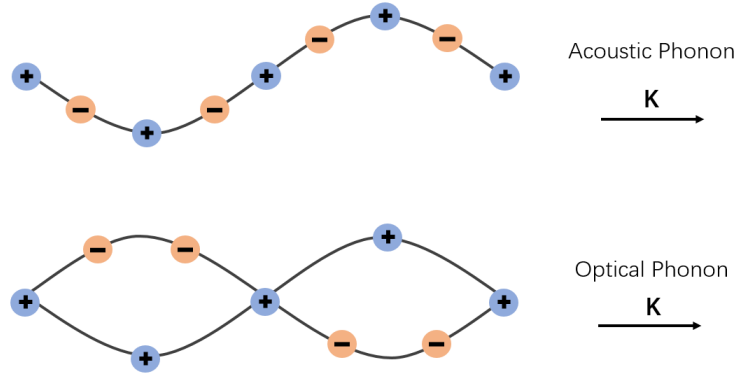


Figure 2.1: Two types of phonon modes in crystalline structure: (up) acoustic phonons, where the movement of atoms is in phase and (down) optical phonons, where the movement of atoms is out-of-phase. Optical phonons can be excited by electromagnetic waves.

Our following discussion is based on a system which consists of two non-magnetic media and here we consider $\mu = 1$, where μ is the permeability. One interesting property of the film medium that we focus on is the dielectric constant $\epsilon_j, j = 1, 2$, where the index refers to the medium so j has to be set to 1 or 2. Cartesian coordinates are applied where the z -axis represents the direction perpendicular to the interface, whereas the y and x -axis are parallel to the

interface. The evanescent electromagnetic wave is designed to propagate along the interface in the y -axis in both media. The system is depicted in Figure 2.2:



Figure 2.2: Schematic of a system consisting of two media, which are separated by a plane interface. ϵ_1 and ϵ_2 refer to dielectric functions in medium 1 and medium 2, respectively.

The analysis is based on Maxwell equation. One of the interests is to find out the existence condition for SPhPs. We start with the Maxwell equation in matter:

$$\nabla \cdot \mathbf{D} = \rho, \quad (2.1)$$

$$\nabla \cdot \mathbf{B} = 0, \quad (2.2)$$

$$\nabla \times \mathbf{E} = -\frac{\partial \mathbf{B}}{\partial t}, \quad (2.3)$$

$$\nabla \times \mathbf{H} = \mathbf{J} + \frac{\partial \mathbf{D}}{\partial t}. \quad (2.4)$$

where $\mathbf{D} = \epsilon_0 \mathbf{E}$ and $\mathbf{B} = \mu_0 \mathbf{H}$. Due to the absence of free point charge and electrical current, $\rho = 0$ as well as $\mathbf{J} = 0$.

Conventionally, the transverse electromagnetic waves are assumed to take the forms:

$$\mathbf{E}(\mathbf{r}, t) = \mathbf{E}(\mathbf{r})e^{i\omega t}, \quad (2.5)$$

$$\mathbf{H}(\mathbf{r}, t) = \mathbf{H}(\mathbf{r})e^{i\omega t}. \quad (2.6)$$

By replacing Equations 2.5 and 2.6 into Equations 2.3 and 2.4, we have:

$$\nabla \times \mathbf{E} + i\mu\omega \mathbf{B} = 0, \quad (2.7)$$

$$\nabla \times \mathbf{B} - i\epsilon\omega \mathbf{B} = 0, \quad (2.8)$$

Applying rotor to both Equations 2.7 and 2.8, new equations arise as:

$$(\nabla^2 + \mu\epsilon\omega^2)\mathbf{E} = 0, \quad (2.9)$$

$$(\nabla^2 + \mu\epsilon\omega^2)\mathbf{B} = 0. \quad (2.10)$$

This formalism can be applied in any coordinate system. In the following discussion, we will only use Cartesian coordinates. Besides, the dielectric constant is defined as the following complex quantity:

$$\epsilon = \epsilon_r - i\epsilon_i, \quad (2.11)$$

Let us assume a semi-infinite system with a plane interface separating two media. Each medium is homogeneous, isotropic and its dielectric constant ϵ and magnetic constant μ are independent.

Moreover, let us define β as the wavevector parallel to the interface, p_1 and p_2 referring to the wave vectors perpendicular to the interface in medium 1 and 2, respectively. Consequently, p_1 and p_2 are defined as follows:

$$p_j^2 = \beta^2 - \epsilon_j k_0^2, \quad (2.12)$$

where $j=1,2$, and $k_0=\omega/c$ where c is the speed of light in vacuum.

Here, we discuss the continuity on the interface region where $z = 0$. The electric field has the form $\mathbf{E}(x, t) = E_{x,j}e^{(i\omega t - p_j x)}$. The continuity of the electric field imposes that:

$$E_{x,1} = E_{x,2} \quad (2.13)$$

The continuity condition of the magnetic field yields:

$$\frac{\epsilon_1}{p_1}E_{x,1} + \frac{\epsilon_2}{p_2}E_{x,2} = 0 \quad (2.14)$$

We have the following solution:

$$\frac{\epsilon_1}{p_1} + \frac{\epsilon_2}{p_2} = 0 \quad (2.15)$$

Combining the three last equations leads to:

$$\frac{\epsilon_1^2}{\epsilon_2^2} = \frac{\beta^2 - \epsilon_1 k_0^2}{\beta^2 - \epsilon_2 k_0^2} \quad (2.16)$$

Equation 2.16 is simplified and the dispersion relation of semi-infinite media is obtained:

$$\beta = \frac{\omega}{c} \sqrt{\frac{\epsilon_1 \epsilon_2}{\epsilon_1 + \epsilon_2}} \quad (2.17)$$

Before moving to extend our discussion on any complex variables such as the in-plane wavevector β or the dielectric constant ϵ , the surface wave propagating forward, i.e. $\beta > 0$ requires two conditions:

(1) the dielectric constants of the media have opposite signs ($\epsilon_1\epsilon_2 < 0$) and the sum of the dielectric constants is positive ($\epsilon_1 + \epsilon_2 > 0$). Under the condition that $\epsilon_1 = 1$, the dielectric constant of medium 2 must satisfy: $-1 < \epsilon_2 < 0$;

(2) the dielectric constants of the two media are with the same signs ($\epsilon_1\epsilon_2 > 0$) and the sum of the dielectric constants is negative ($\epsilon_1 + \epsilon_2 < 0$). Such dielectric constant of medium 2 does not exist.

Next, we consider that the medium 2 is dissipative ($\beta = \beta_r - i\beta_i$) and the dielectric constant is in a complex form $\epsilon_2 = \epsilon_{2r} - i\epsilon_{2i}$. With considering the absorption exists in the medium 2, i.e. $\epsilon_i \neq 0$. Equation 2.17 can be expanded in the following expression:

$$\beta_r - i\beta_i = \frac{\omega}{c} \sqrt{\frac{\epsilon_1(\epsilon_{2r} - i\epsilon_{2i})}{\epsilon_1 + \epsilon_{2r} - i\epsilon_{2i}}} \quad (2.18)$$

The real and imaginary part of the in-plane wavevectors can be organized as follows:

$$\beta_r = \frac{\omega}{c} \sqrt{\frac{\epsilon_1}{(\epsilon_1 + \epsilon_{2r})^2 + \epsilon_{2i}^2} \frac{\epsilon_e^2 + (\epsilon_e^4 + \epsilon_1^2 \epsilon_{2i}^2)^{1/2}}{2}}, \quad (2.19)$$

$$\beta_i = \frac{\omega}{c} \sqrt{\frac{\epsilon_1}{(\epsilon_1 + \epsilon_{2r})^2 + \epsilon_{2i}^2} \frac{\epsilon_{2i}\epsilon_1}{2(\epsilon_e^2 + (\epsilon_e^4 + \epsilon_1^2 \epsilon_{2i}^2)^{1/2})}} \quad (2.20)$$

where $\epsilon_e^2 = \epsilon_{2r}^2 + \epsilon_{2i}^2 + \epsilon_{2r}\epsilon_1$.

With an ideal condition that the absorption in medium 2 is negligible, i.e. $\epsilon_{2i} = 0$, we develop in the Equation 2.16 and obtain a simplified dispersion relation as follows:

$$\beta_r = \frac{\omega}{c} \sqrt{\frac{\epsilon_1\epsilon_{2r}}{(\epsilon_1 + \epsilon_{2r})}}, \quad (2.21)$$

In the following discussion, we only consider the case that an absorbing medium 2 and the dispersion relation is expressed with Equation 2.20. In this Equation, we assume $\epsilon_{2r} < 0$, $-\epsilon_{2r} \gg \epsilon_{2i}$ and $-\epsilon_{2r} > \epsilon_1$, the Equation 2.20 can be simplified as:

$$\beta_r \approx \frac{\omega}{c} \sqrt{\frac{\epsilon_1 \epsilon_{2r}}{\epsilon_1 + \epsilon_{2r}}} > \frac{\omega}{c} \epsilon_1^{1/2}, \quad (2.22)$$

$$\beta_i \approx \frac{\omega}{c} \frac{\epsilon_{2i} \epsilon_1}{2(-\epsilon_{2r} - \epsilon_1)} \sqrt{\frac{\epsilon_1}{\epsilon_{2r}^2 + \epsilon_1 \epsilon_{2r}}}, \quad (2.23)$$

Under these approximations, the Equation 2.22 demonstrate the SPhPs modes exist with the condition that the real part of the in-plane wavevector β_r is greater than the one of light, i.e. $\beta_r > \frac{\omega}{c} \epsilon_1^{1/2}$. And the the imaginary part of the in-plane wavevector β_i describes the absorption of the medium 2. These quantities are strongly depends on the complex dielectric constant and the absorption of the medium 2. The quantification will be provided and discussed dedicated to certain dielectric material, such as SiN, in the following section.

2.3 Suspended dielectric thin film surrounded by the same media $\epsilon_1 = \epsilon_3$

In this subsection, we aim at studying a system consisting of three media. Slightly different from two semi-infinite media separated by a single interface that we presented in the previous subsection, here we discuss a system (depicted in figure 2.3) with two parallel interfaces located at $z = 0$ and $z = d$. The surface electromagnetic wave is chosen to propagate along the interface in the y direction.

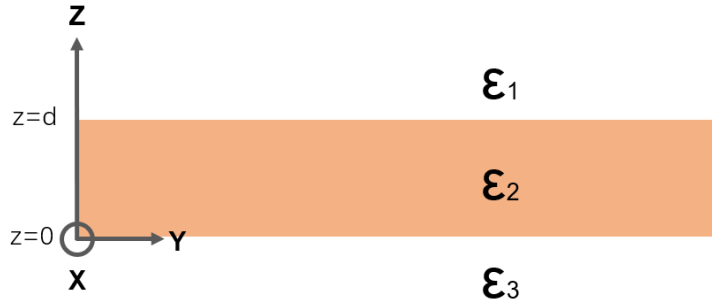


Figure 2.3: Schematic of a system consisting of three media, which are separated by two interfaces at $z=0$ and $z=d$, where d is the thickness of the second medium. ϵ_1 , ϵ_2 and ϵ_3 refer to the dielectric function in medium 1, medium 2 and medium 3, respectively.

In the case of a suspended thin film with thickness d , [Yeh and Shimabukuro \(2008\)](#) formulate the dispersion relation as follows:

$$\tanh(p_2 d) = -\frac{p_2 \epsilon_2 (p_1 \epsilon_3 + p_3 \epsilon_1)}{p_2^2 \epsilon_1 \epsilon_3 + p_1 p_3 \epsilon_2^2}, \quad (2.24)$$

When considering $\epsilon_1 = \epsilon_3$, the wavevectors along the y direction are symmetric on the top side ($z = d$) and on the bottom side ($z = 0$) of the film. Additionally, Equation 2.24 shows two branches where one is considered as even magnetic field and another as odd magnetic field [Yeh and Shimabukuro \(2008\)](#). Here we only discuss the even branch since its propagation length is larger ([Yang et al. \(1991\)](#)). Equation 2.24 eventually yields:

$$\tanh\left(\frac{p_2 d}{2}\right) = -\frac{p_1 \epsilon_2}{p_2 \epsilon_1}, \quad (2.25)$$

When the film thickness is thick enough, meaning that $p_2 d/2 \gg 1$, Equation 2.25 is simplified as follows:

$$p_1 \epsilon_2 + p_2 \epsilon_1 = 0 \quad (2.26)$$

This is exactly the dispersion relation that we have developed for a two media system.

In the case with a sufficiently thin film, $p_2 d/2 \ll 1$, the approximation of Equation 2.25 leads to:

$$\frac{p_2 d}{2} = -\frac{p_1 \epsilon_2}{p_2 \epsilon_1}, \quad (2.27)$$

with the condition that $p_2^2 = p_1^2 - (\epsilon_2 - \epsilon_1)k_0^2$, and that the real part of p_1 is positive to guarantee that the electrical and magnetic fields behave properly ([Yeh and Shimabukuro \(2008\)](#), [Ordonez-Miranda et al. \(2013\)](#)), Equation 2.27 then yields:

$$p_1 = \frac{d}{2} \left(1 - \frac{\epsilon_1}{\epsilon_2}\right) \epsilon_1 \frac{\omega^2}{c^2}, \quad (2.28)$$

We consider the wavevector along the surfaces with the complex form $\beta = \beta_r - i\beta_i$, as well as the complex transverse wavevector $p = p_r - ip_i$. Finally, the longitudinal wavevector can be written as:

$$\beta_r = \sqrt{\epsilon_1} \frac{\omega}{c} \left[1 + \frac{\epsilon_1 \left(\frac{\omega d}{c}\right)^2}{8} \left(1 - \frac{2\epsilon_1 \epsilon_{2r}}{|\epsilon_2|^2} + \frac{\epsilon_1^2 (\epsilon_{2r}^2 - \epsilon_{2i}^2)}{|\epsilon_2|^4} \right) \right], \quad (2.29)$$

$$\beta_i = \sqrt{\epsilon_1} \frac{\omega}{c} \frac{\left(\frac{\omega d}{c}\right)^2}{4} \frac{\epsilon_1^2 \epsilon_{2i}}{|\epsilon_2|^2}, \quad (2.30)$$

2.4 Dielectric constant and dispersion relation of SiN films

The dielectric constant $\epsilon(\omega)$ describes the dielectric response to an incident electric field $E(\omega)$. The dielectric constant of a doped semiconductor is defined by a function of frequency, ω , provided by the classical Maxwell-Helmholtz-Drude model (Button (1983)):

$$\epsilon(\omega) = \epsilon_{\infty} + \sum_{j=1}^M \frac{(\epsilon_{j+1} - \epsilon_j)\omega_{Tj}^2}{\omega_{Tj}^2 - \omega^2 - i\Gamma'_j(\omega)\omega} \quad (2.31)$$

where ϵ_j has a complex form $\epsilon_j = \epsilon_{jr} + i\epsilon_{ji}$, ϵ_{jr} and ϵ_{ji} are the real and imaginary part of the dielectric function, with j being the number of oscillators, ω_p is the plasma frequency and Γ'_j is the effective Lorentzian damping coefficient:

$$\Gamma'_j(\omega) = \Gamma_j \exp\left[-\alpha_j \left(\frac{\omega_{Tj}^2 - \omega^2}{\omega\Gamma_j}\right)^2\right], \quad (2.32)$$

where α_j refers to an interpolation between Lorentzian ($\alpha_j = 0$) and Gaussian wings ($\alpha_j > 0$).

j	ϵ_{jr}	ϵ_{ji}	$\omega_{Tj}/2\pi(THz)$	$\Gamma_j/2\pi(THz)$	α_j
1	7.582	0	13.913	5.81	0.0001
2	6.754	0.3759	15.053	6.436	0.3427
3	6.601	0.0041	24.521	2.751	0.0006
4	5.430	0.1179	26.44	3.482	0.0002
5	4.601	0.2073	31.724	5.948	0.008
6	4.562	0.0124			

Table 2.1: Fitting parameters for five oscillators characterized by Cataldo et al. (2012).

The real part and the imaginary part of the dielectric constant of a SiN film is presented in Figure 2.4. In glass, there exists two frequency regimes supporting SPhPs, i.e. in the vicinity of 90 Trad/s and 210 Trad/s (Palik (1998)). In SiN, a single SPhP resonance around 170 Trad/s exists. This resonance frequency indicates that a large amount of electromagnetic energy is absorbed in SiN.

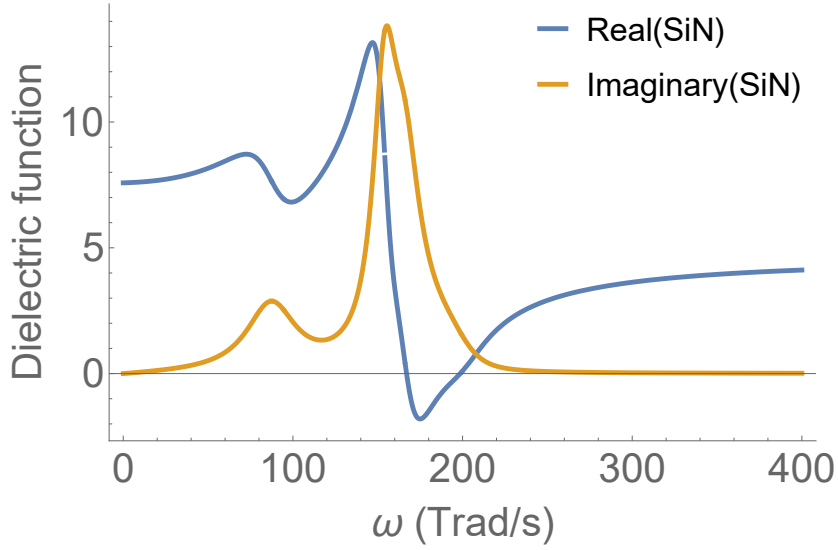


Figure 2.4: Real and imaginary parts of the dielectric function of silicon nitride constructed with Equation 2.31 and the fitting parameters of Table 2.1.

2.5 Calculation of the dispersion relation and the mean free path of surface modes in SiN film

The calculations in the following subsections is based on the SiN dielectric constant obtained in the previous chapter. The dispersion relation of the SPhPs are demonstrated in two cases: for a SiN-air single interface and for a SiN film suspended in air.

2.5.1 Case of the SiN-air single interface

Based the analytical model we developed before, Figure 2.5 demonstrates that the dispersion relation of the SiN-air single interface with comparison of the one of light with taking into account the absorption in the dielectric films. The SPhPs As we can see, only limited amount of propagating surface modes exist in the case of a single interface of SiN and air.

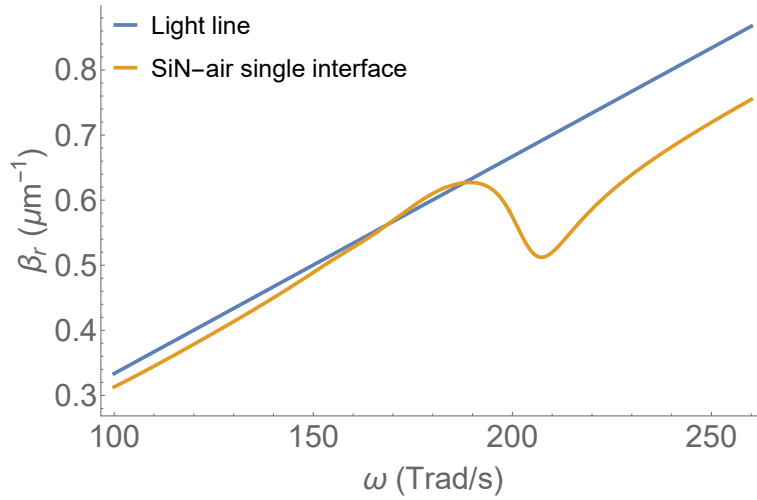


Figure 2.5: Comparison of dispersion relation of the SiN-air single interface (yellow line) and light (blue line). The dispersion curve presented here are considered the absorption by the SiN material.

2.5.2 Case of the SiN film surrounded by air

As we discussed before, the propagating surface mode exist when the real part of the in-plane wavevector locates on the the left side of the light line, i.e. $\beta_r > \frac{\omega}{c} \epsilon_1^{1/2}$, the dispersion relation is shown in Figure 2.6.

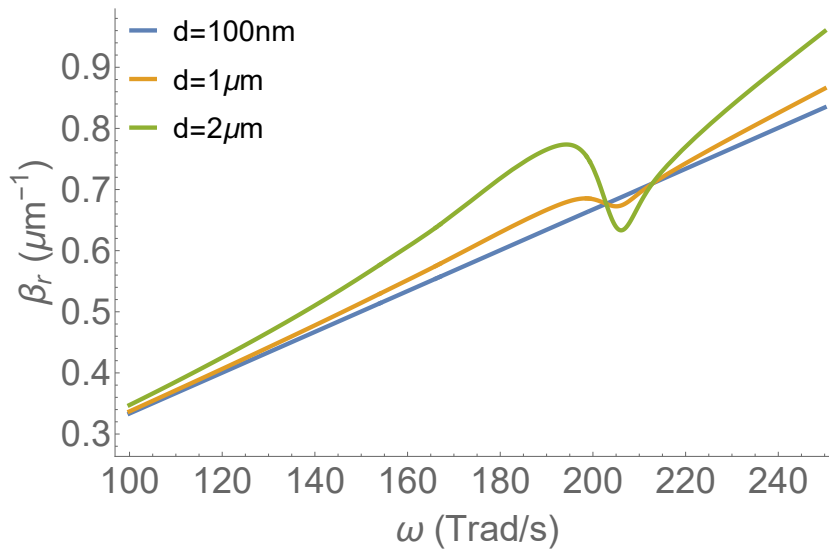


Figure 2.6: Dispersion relation of SPhPs in a suspended SiN membrane with symmetrical surroundings ($\epsilon_1 = \epsilon_3 = 1$). The calculation is based on three thicknesses: $d = 2 \mu\text{m}$ (blue line), $d = 1 \mu\text{m}$ (yellow line) and $d = 100 \text{ nm}$ (green line).

Three different thicknesses of SiN film are considered here: 100 nm, 1 μm and 2 μm . The propagating surface modes cover nearly the whole range of frequency, and the numbers of surface modes decrease when the thickness of the film decrease because less surface modes can be coupled.

The imaginary part of the in-plane wavevector is plotted in Figure 2.7. This quantity is related to the absorption of surface modes and as we can see, the absorption decrease as the films thickness decrease.

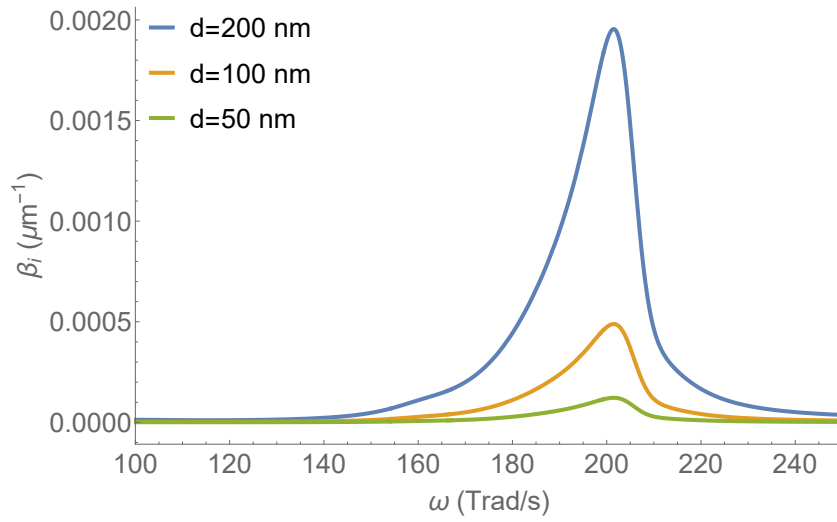


Figure 2.7: *Imaginary part of wavevector as a function of frequency for a suspended SiN membrane in symmetrical surroundings ($\epsilon_1=\epsilon_3=1$). The calculation is based on three different thicknesses film: $d=200$ nm (blue curve), $d=100$ nm (yellow curve) and $d=50$ nm (green curve).*

As formulated by [Chen et al. \(2005b\)](#), the mean free path of SPhPs is inversely proportional to the imaginary part of the wavevector: it yields:

$$\Lambda = \frac{1}{2\beta_i}, \quad (2.33)$$

As reported in Figure 2.8, the MFP of SPhPs increases when the film thickness d decreases. In the case of 50 nm thick film, the absorption in the dielectric film is very small and it leads to nearly two orders of magnitude of the enhancement in mean free path. One note that at the frequency 200 Trads/s, the MFP reaches a minimum corresponding to the optical phonon resonance.

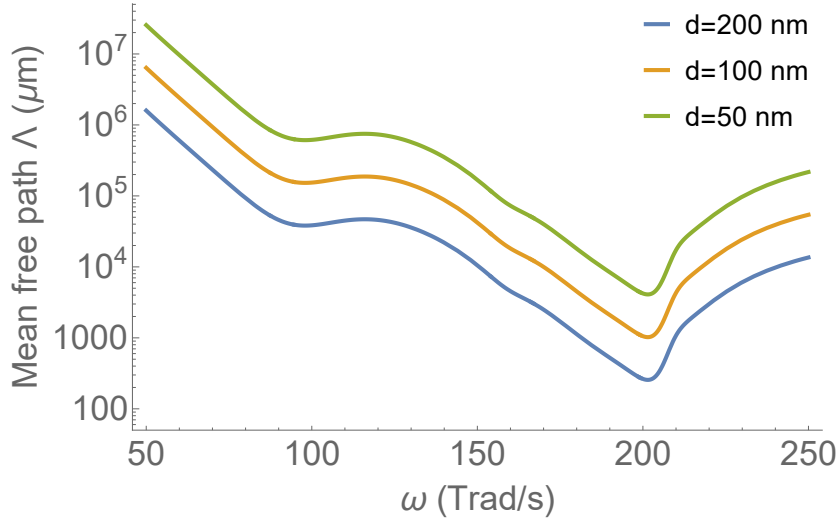


Figure 2.8: Mean free path of SPhPs as a function of frequency for a suspended SiN membrane with symmetrical surroundings ($\epsilon_1 = \epsilon_3$). The calculation is based on three thicknesses: $d=200$ nm (blue line), $d=100$ nm (yellow line) and $d=50$ nm (green line).

2.6 SPhPs thermal conductivity

In this section, we aim at building a formalism based on Boltzmann transport equation to investigate the in-plane thermal conductivity contributed by surface phonon polaritons. We apply this model on amorphous silicon nitride suspended films and calculate the SPhPs contribution with thickness and temperature dependences.

We develop the model in detail of the surface effect and target the role of structure confinement. Let us first consider a simple planar film depicted in Figure 2.9 with limited lateral dimensions: L_y as its total length, L_x as its total width and d as its thickness. A temperature difference is applied along the y-axis direction where T_H and T_c labels the hot side and the cold side, respectively. The film is sufficiently thin so that the temperature gradient along the z-axis remains negligible. We emphasize that the film is suspended and has a frequency-dependent dielectric function $\epsilon(\omega)$ differing from the surrounding media. The heat flux Q_y is excited on both surfaces of the film and propagates along the y-axis.

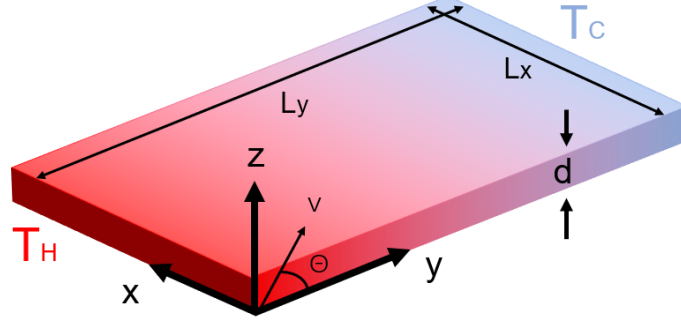


Figure 2.9: Schematic view of a film with thickness d , width L_x and length L_y . The z -axis is chosen to be perpendicular to the film, while the x -axis and y -axis are parallel to the in-plane direction. Temperature difference is applied on the two sides of the film, which leads to a heat flux following the temperature gradient and propagating along the y -axis.

For an elementary interval of time dt , the amount of flux passing through a cross-section $L_x \cdot d$ is defined as:

$$dQ_y = \frac{dE}{dtd(xz)}, \quad (2.34)$$

The amount of energy dE is defined based on statistical mechanics:

$$dE = \hbar\omega f d^2q d^2p \quad (2.35)$$

where \hbar denotes the Planck constant divided by 2π , ω is the angular frequency, f is a distribution function. q and p correspond to the position and momentum, which have derivative forms as follows:

$$d^2q = dx dz, \quad (2.36)$$

$$d^2p = \hbar d^2\beta, \quad (2.37)$$

where β denotes the in-plane wavevector. Combining Equation 2.34 and 2.35, the flux in an elementary wavevector interval and angle interval propagating in the y direction has a form that:

$$dQ_y = \frac{\hbar\omega f}{4\pi^2 d} v \cos(\theta) \beta d\beta d\theta \quad (2.38)$$

The integral of Equation 2.38 with proper boundaries leads the heat flux propagating in the y direction with the form:

$$Q_y = \frac{1}{4\pi^2 d} \int \int v \hbar\omega f \cos(\theta) \beta d\beta d\theta, \quad (2.39)$$

In a non-equilibrium regime, the Boltzmann Transport Equation (BTE) is a conservation equation for the distribution function $f(r, \beta, t)$:

$$\frac{\partial f}{\partial t} + \frac{\hbar\beta}{m^*} \nabla_r f + \frac{F}{\hbar} \nabla_\beta f = \sum_{\beta'} f(\beta') S(\beta', \beta) - \sum_{\beta} f(\beta) S(\beta, \beta'), \quad (2.40)$$

where m^* is the effective mass of the particle, F refers to the external force, and $S(\beta', \beta)$ and $S(\beta, \beta')$ correspond to the scattering rate from states β' to β and from states β to β' , respectively.

The approximation of a single relaxation time is introduced here. In addition, the transport regime is in steady state and no external force is applied, the Equation 2.40 is thus simplified as follows:

$$v \nabla_r f = \frac{f - f_0}{\tau}, \quad (2.41)$$

where v denotes $\frac{\hbar\beta}{m^*}$ and f_0 is the distribution function at equilibrium and τ refers to the relaxation time.

Moreover, we only assume that the temperature gradient and the difference of the distribution exist in the y direction, therefore:

$$f(T) - f_0(T) = \Lambda \cos(\theta) \frac{\partial f}{\partial y}, \quad (2.42)$$

where Λ is the mean free path. For phonons, photons and thus for SPhPs, f_0 refers to the Bose-Einstein distribution with the form:

$$f_0(T) = \frac{1}{\exp(\frac{\hbar\omega}{k_B T}) - 1}, \quad (2.43)$$

We choose the y direction as the positive propagation direction, such that Q_+ and Q_- take the expressions as follows:

$$Q_+ = \frac{1}{4\pi^2 d} \int_{-\frac{\pi}{2}}^{\frac{\pi}{2}} (f_0 - \Lambda \cos(\theta) \frac{\partial f_0}{\partial y}) \cos(\theta) d\theta \int \hbar\beta\omega d\omega, \quad (2.44)$$

$$Q_- = \frac{1}{4\pi^2 d} \int_{\frac{\pi}{2}}^{\frac{3\pi}{2}} (f_0 - \Lambda \cos(\theta) \frac{\partial f_0}{\partial y}) \cos(\theta) d\theta \int \hbar\beta\omega d\omega, \quad (2.45)$$

Consequently, by considering that the net flux Q_y is simply the difference of the fluxes along the y axis, i.e. $Q_y = Q_+ - Q_-$ and with the Fourier law leads to $Q_y = -\frac{\partial T}{\partial y} \kappa_{SPhPs}$. We thus derive the expression of the thermal conductivity contributed by SPhPs κ_{SPhPs} :

$$\kappa_{SPhPs} = \frac{1}{4\pi d} \int_{\omega_L}^{\omega_H} \hbar\omega \Lambda \beta_r \frac{\partial f_0}{\partial T} d\omega, \quad (2.46)$$

where κ_{SPhPs} refers to the in-plane thermal conductivity contributed by SPhPs, d to the thickness of the film. f_0 is the Bose-Einstein distribution function, T the temperature of the film, β_r denotes the real part of the wave vector along the in-plane axis, Λ the mean free path of the SPhPs, \hbar is the Planck's constant divided by 2π . Finally ω_H and ω_L are the lowest and highest cutoff frequencies of the SPhPs associated with the frequency region where the surface modes are evanescent.

As shown in Figure 2.4 and based on the numerical calculation of Equation 2.46, the dielectric function of the SiN thin film has a lower cut-off frequency ω_L of 167 Trad/s and a higher cut-off frequency ω_H of 210 Trad/s.

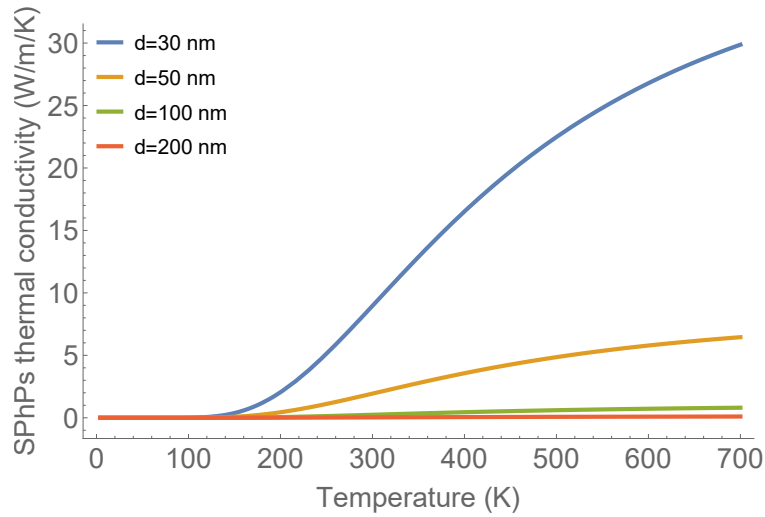


Figure 2.10: Thermal conductivity contributed by SPhPs as a function of temperature in a SiN film for four different thicknesses.

Figure 2.11 shows the SPhPs contribution to the thermal conductivity as a function of the thickness of the amorphous SiN thin film. When the film thickness is 200 nm, the SPhPs contribution is nearly negligible. Note that when the film thickness decreases to 50 nm, the SPhPs thermal conductivity is 6.5 W/m/K, 5 W/m/K, and 2 W/m/K for the temperatures of 700 K, 500 K and 300 K, respectively.

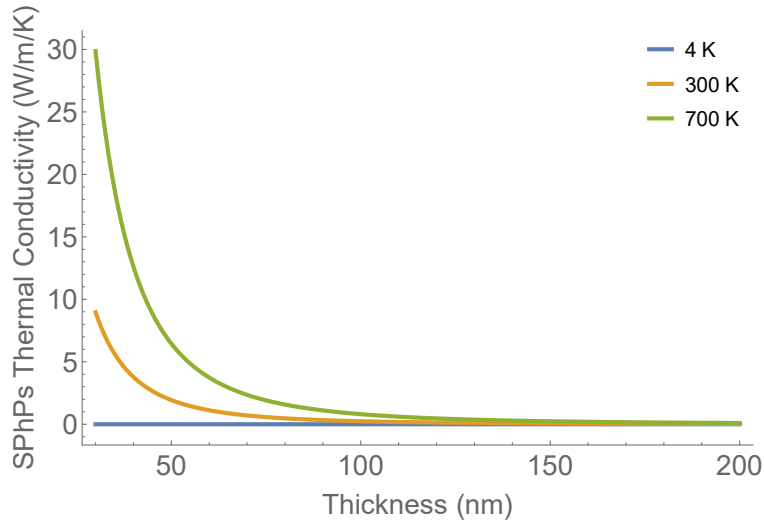


Figure 2.11: *SiN* thin film thermal conductivity contributed by SPhPs as a function of thickness and for three different temperatures.

2.7 Survey of experimental thermal conductivity values of SiN contributed by phonons

At room temperature, the measurement of the total in-plane thermal conductivity of amorphous SiN films have been reported by several teams (as shown in Figure 2.12). Griffin Jr et al. (1994) measured 60 nm to 8.5 μm thick films and they reported a thermal conductivity of approximately 2 W/m/K. A thickness-independent behavior was also observed by Mastrangelo et al. (1990) on 2 - 5 μm thick films and they reported a thermal conductivity approximately of 3.2 W/m/K. A thickness-dependent behavior was also observed by Lee and Cahill (1997) on thinner 20-260nm films. They reported that the in-plane thermal conductivity is decreased when the structure scales down, except for the thin film with a thickness of 200 nm.

Hence, none of the experimental studies highlighted the enhancement of total in-plane thermal conductivity in thinner film so far. Indeed, all the measurements presented above are performed at room temperature and the high temperature-dependent thermal conductivity of SiN thin films is missing so far.

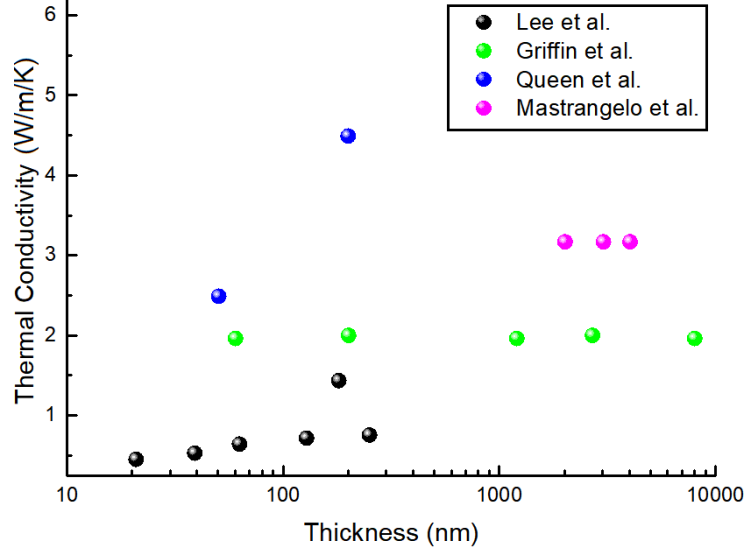


Figure 2.12: Thermal conductivity of amorphous SiN films as a function of thickness. These experimental results are obtained at room temperature. No thickness dependence is observed by Griffin Jr et al. (1994) (green dots) on 60 nm to 8.5 μm thick films or by Mastrangelo et al. (1990) (pink dots) on 2 - 5 μm thick films. Lee and Cahill (1997) reported that from 200 nm film to 250 nm thicknesses, the increase in thermal conductivity is less than 30%. However, a surprising jump around 200 nm is noticed. Queen and Hellman (2009) indicated an increase of 2.5 W/m/K between the 50 nm thick film to the 200 nm thick one.

2.8 Conclusion

In this chapter, we explore the fundamental theorem of the excitation and propagation of the SPhPs modes in two cases: a single interface of air-dielectric and a suspended dielectric film surrounded by air. Our parametric study demonstrates that the propagation and absorption of the surface waves can be tuned by varying the thickness of the dielectric medium. Furthermore, we developed the formalism which quantifies the contribution of the SPhPs modes to in-plane thermal conductivity based on the Boltzmann transport equation. This analytical prediction leads us to conduct a thermal measurement in the later section.

Chapter 3

Sample fabrication

3.1 Sample preparation

The samples were fabricated on commercially available SiN suspended membranes purchased from Norcada company. Aluminum pads allowing for the TDTR laser heating and probing of the sample, were deposited on the membranes using the standard top-down approach as shown in Figure 3.1: first, the resist (ZEP-520A) for electron beam (EB) lithography was spin-coated on the membranes for 60 seconds at 4500 rpm. Then, the resist was baked at 160 °C for 3 mins. These parameters are chosen to ensure the thickness of the resist (320 nm) to be several times thicker than the deposited metallic layer (70 nm) for the correct lift-off process of the EB resist.

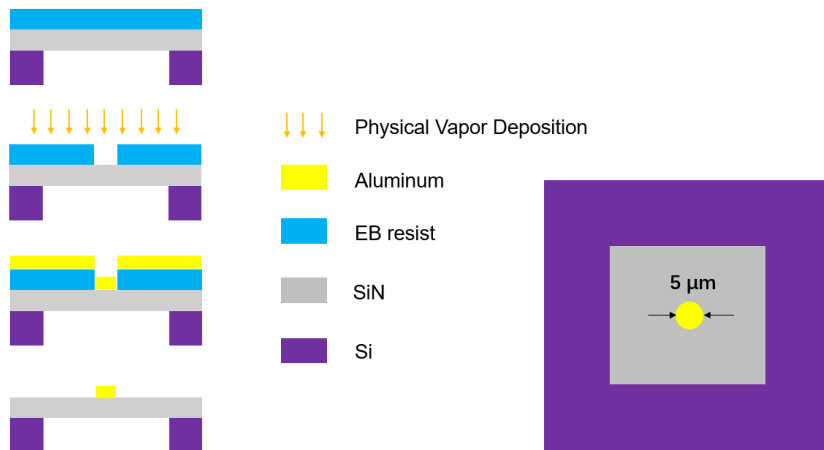


Figure 3.1: Schematic of a SiN membrane fabrication process: firstly, 320 nm thick EB resist is spun on the top of the suspended film; secondly, circular patterns are drawn by electron beam lithography and then an aluminum layer is deposited by physical vapor deposition; finally, the EB resist is removed by the ZD-MAC resist remover.

3.2 EB lithography and patterns design

Next, the electron beam (EB) lithography as shown in Figure 3.2 was used to draw the metal pad shapes in multiple locations on the membranes. The EB machine (model: JBX-6300FS) is designed by JEOL company, which can easily write patterns down to 8 nm by the employment of an electron optical system that automatically adjusts a 2.1 nm-diameter electron beam at 100 kV accelerating voltage. Furthermore, this EB machine can achieve at a high field-stitching and overlay accuracy of 9 nm, providing high cost performance. Since the EB machine has a high-precision stage that employs Beam positioning of 19 bits with 0.125 nm resolution and Laser interferometer with 0.6 nm resolution, the top-of-the-line writing positional accuracy of 9 nm is achieved for small fields to large-area fields.



Figure 3.2: *EB lithography machine (model: JBX-6300FS) from JEOL company, which can easily write patterns down to 8 nm or less (actual result: 5 nm) by the employment of an electron optical system that automatically adjusts a 2.1 nm-diameter electron beam at a 100 kV accelerating voltage.*

Figure 3.3 features a GDS file compatible with the EB lithography machine. The pattern is designed to have a separation of the pads of 200 μm . This separation distance is to ensure the thermal isolation and later to compare with a structure of the same dimension in the numerical model. To develop the exposed regions of the resist, ZED N-50 developer was applied for two minutes, followed by one minute application of a ZMD-B development stopper. The use of ZED N-50 developer and ZMD-B development stopper is specified for the ZEP-520A EB resist.

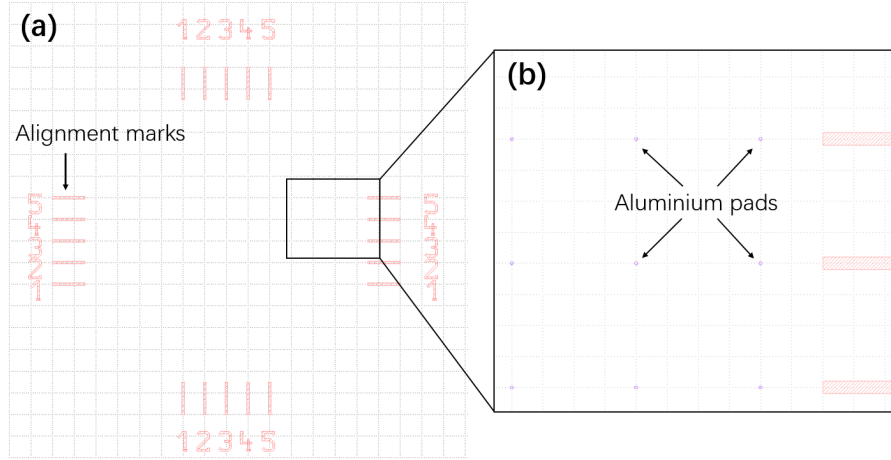


Figure 3.3: GDS pattern for EB lithography. (a) Five metal strips per side for mask alignment. (b) square lattice metal pads are drawn for EB lithography. The length of the side of a square in (a) is $200 \mu\text{m}$ and in (b) is $50 \mu\text{m}$.

3.3 PVD deposition and SEM characterization

After the lithography process, the samples were placed in the vacuum chamber of the electron-beam assisted physical deposition machine Ulvac EX-300, as shown in Figure 3.4, for aluminum deposition. Further details related to this fabrication process is reported in [Anufriev et al. \(2017\)](#) and [Anufriev et al. \(2016\)](#).

The samples were heated up to $60 \text{ }^\circ\text{C}$. Then, 65 nm of aluminum topped with 5 nm of gold were evaporated at the rate of 1 \AA/s . After the deposition, the lift-off process was done by applying a ZD-MAC resist remover for around 24 hours, followed by a sample cleaning in acetone and IPA at $50 \text{ }^\circ\text{C}$ for 2.5 mins. A SEM image is taken, as shown in Figure 3.5, to characterize the size of an aluminum pad. An optical microscopy image is taken, as shown in Figure 3.6, to allow the visualization of the quality of the membrane after the fabrication process.

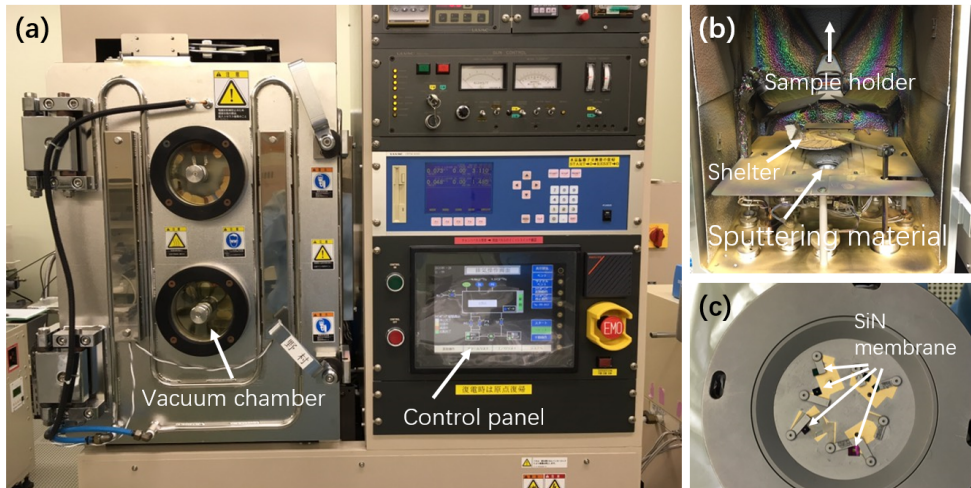


Figure 3.4: *Electron-beam physical vapor deposition: (a) view from outside, PVD machine consists of a vacuum chamber and a control panel; (b) view from inside, where a sample holder is attached in the top of the vacuum chamber, the sputtering target is placed at the bottom and is evaporated by EB during the process, a shelter is placed between the sample holder and the target to switch on/off the process; (c) SiN membranes are fixed on a sample holder by metal strips.*

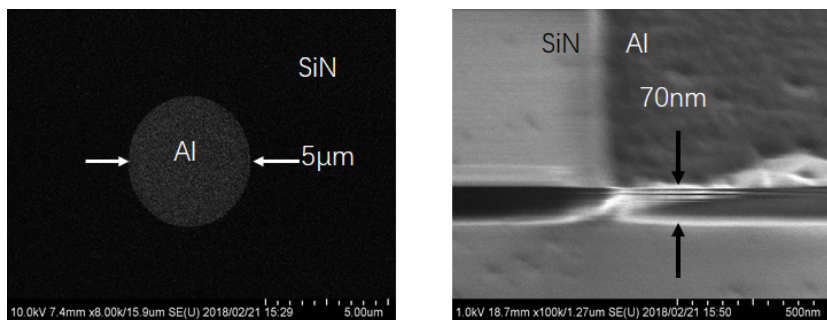


Figure 3.5: *SEM image of a SiN membrane after fabrication: (a) top view showing that the aluminum pads have a diameter of 5 μm; (b) Inclined view of a metal strip showing that the aluminum layer has a thickness of 70 nm.*

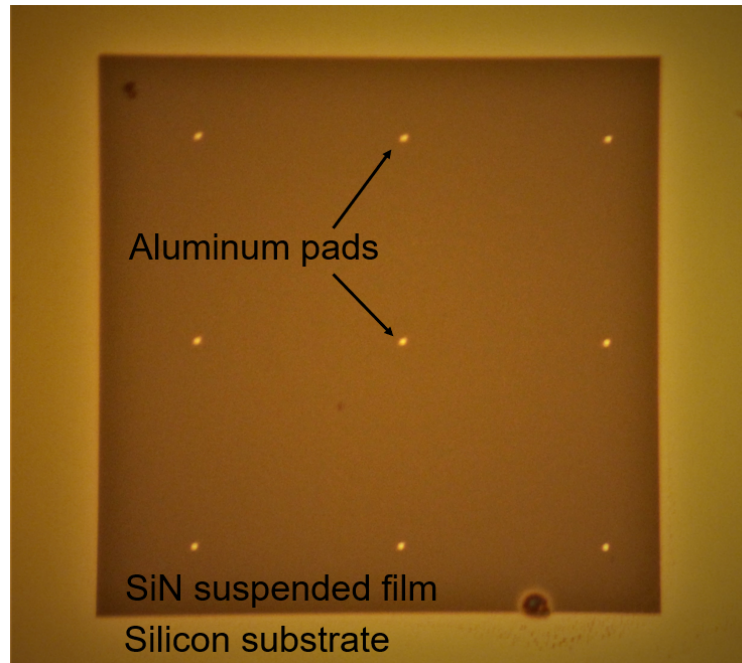


Figure 3.6: *Microscopy image of the top view of a 30 nm thick SiN membrane with aluminium pads.*

3.4 Conclusion

In this chapter, we demonstrate the cleanroom fabrication process for a $5 \mu\text{m}$ in diameter and 70 nm thick metal pad on the suspended amorphous SiN thin films. This top-down approach consists of EB lithography and PVD deposition. The characterization carried by the SEM and optical microscopy ensure the dimension of the metal pads. Due to the fact that the SiN films are highly stressed and with a thickness in the submicron range, the fabrication remains challenging especially during the PVD deposition and the lift-off process. These metal pads will be served simultaneously as a transducer and as a sensor in the following thermal characterization.

Chapter 4

Thermal characterization

4.1 Thermal decay measurement with TDTR

The thermal properties of the sample were measured using a micro-time-domain thermoreflectance (TDTR) setup, schematically shown in Fig. 4.1 (a). The TDTR measurement technique is an all-optical pump-probe technique for contactless measurements, and thus is an optimal choice for measurements on different samples at different temperatures without opening the cryostat.

The sample were placed either in a Helium-flow cryostat or in a water-flow heating stage for the low (4 - 300 K) and high (300 - 600 K) temperature measurements correspondingly. The pressure in the cryostat was kept below 10^{-3} Pa to avoid convection.

The TDTR technique involves two laser beams: a continuous wave probe beam (785 nm) and a pulsed pump beam (642 nm). Both laser beams are focused on the aluminum pad by an optical microscope with a x40 magnification. The probe beam is used to continuously measure the reflectance of the aluminum pads by monitoring the intensity of the reflected beam in the photodetector plugged in a digital oscilloscope. The pump beam is used to periodically heat up the aluminum pad and thus changes its reflectance coefficient, which is proportional to the temperature via the thermoreflectance coefficient. Thus, each pulse of the pump laser generates a jump in the signal of the probe laser. As heat gradually spreads from the aluminum pad through the underlying membrane, the temperature and thus the reflectance of the pad returns to the initial level. This process is measured by the probe laser as a gradual return of the reflected laser intensity shown in Figure 4.1(b).

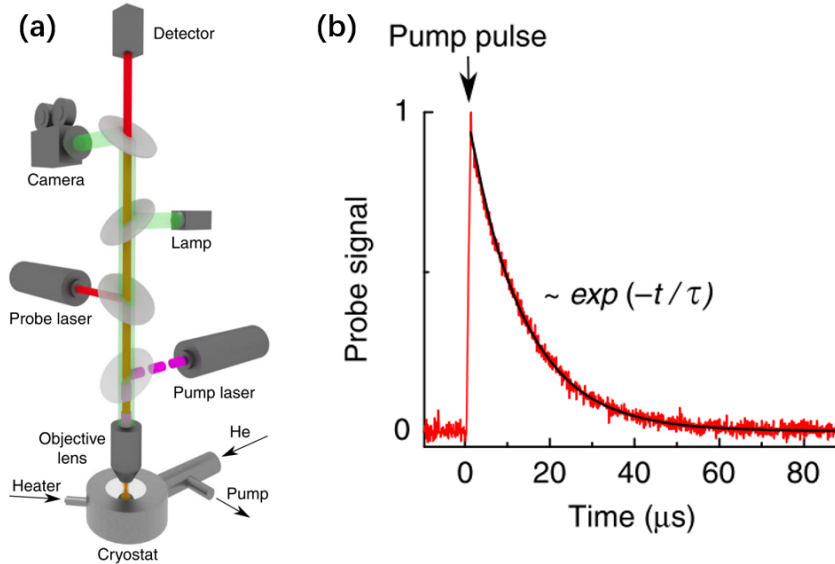


Figure 4.1: (a) Schematic of the TDTR setup: the sample is placed in a cryostat with temperature controlled by an helium flow or a heating stage; a pump laser is periodically heating up the aluminum pads on the sample and a probe laser is continuously measuring the reflectance of the aluminum pads by monitoring the intensity of the reflected beam in the photodetector; a lamp and a camera assist to locate the aluminum pads on the sample; (b) Normalized TDTR decay signal (red line) interpolated by an exponential decay curve (black line) (Anufriev et al. (2017)).

In the case of a ribbon structure, the decay of the pump signal can be described by the exponential function as shown in Figure 4.1 (right), from which the characteristic time of heat dissipation - the decay time - can be extracted. Thus, the TDTR technique allows us to measure the rate of heat dissipation, which can be converted to the thermal conductivity. To reduce the noise of the TDTR signal, 10000 pump pulses are integrated by the lock-in detector to obtain one decay curve. During the measurements, 1000 of the such decay curves are recorded.

4.2 Correction with the TDTR signal

The process presented in the previous section is conventionally used in the nanostructured sample when the heat dissipated in one dimension (Anufriev et al. (2017)). However, with our SiN membrane sample having a cylindrical symmetry, the heat diffusion equation in steady state with lateral and temporal

dependence yields:

$$\frac{1}{r} \frac{\partial}{\partial r} \left(r \frac{\partial T}{\partial r} \right) = \frac{1}{\alpha} \frac{\partial T}{\partial t}, \quad (4.1)$$

where α denotes the thermal diffusivity. Equation 4.1 leads to the solution with a series of exponential component describing the temporal evolution and a series of bessel function denoting the lateral propagation, the solution writes:

$$T(r, t) = \frac{2}{b^2} \sum_{n=1}^{\infty} \frac{J_0(\lambda_n r)}{J_1^2(\lambda_n b)} \exp(-\alpha \lambda_n^2 t) \int_0^b r' J_0(\lambda_n r') f(r') dr', \quad (4.2)$$

where b denotes the radius of the heating area, J_0 and J_1 are the bessel functions of the first and second orders.

As shown in Figure 4.2 (right), the Equation 4.2 can not be described simply by an exponential decay, i.e. the thermal decay time is not directly correlated to the thermal conductivity. The background intensity of the probe laser varies in time as shown in Figure 4.2 (left), leading to the difference (approximately 10 % in the scale of the normalized amplitude) in the intensity at the beginning and at the end of the single measurement. On the other hand, we simulate a single TDTR decay using COMSOL Multiphysics and the intensities at the beginning and at the end of the measurement are consistent. The discrepancy between the experimental decay curve and the numerical ones hinder the accurate extraction of the thermal conductivity of the sample. Thus, an analysis technique is required to compensate the drift in the background intensity of the probe laser.

As shown in Figure 4.2 (right), firstly we specify three regions to implement a correction of the offset: region A corresponds to the time domain before the pump laser excitation; region B relates to the end of the pump laser as well as of the maximum of the TDTR signal and region C refers to the end of a signal TDTR decay curve. The correction method provides a rotation of a TDTR decay curve centered in the region B to compensate the offset amplitude in the region C. The TDTR signal is corrected as follows:

$$Y_f = \bar{Y}_A - t * \frac{\bar{Y}_C - \bar{Y}_A}{t_C - t_A}, \quad (4.3)$$

where Y_f refers to the TDTR signal after the correction, \bar{Y}_A and \bar{Y}_C denote the mean TDTR signal in the region A and C, respectively. t_A and t_C are the

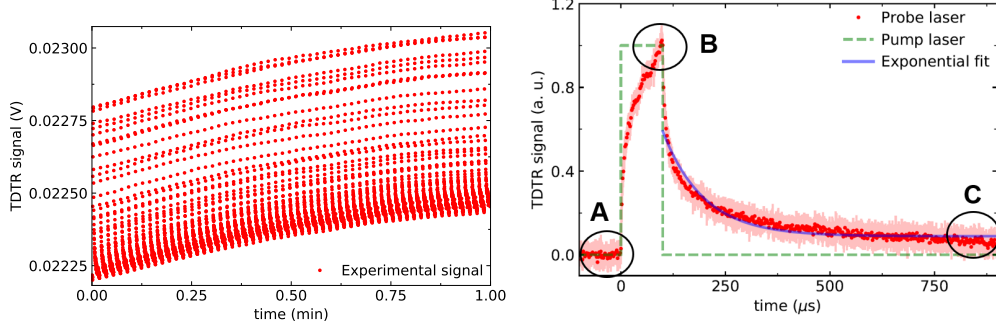


Figure 4.2: (Left) TDTR signals are continuously recorded for one minute, which consist of 1000 TDTR decay curves. (Right) Single TDTR decay curve of a SiN membrane. The red dots and green discontinuous line indicate the normalized intensity of the probe and pump laser, respectively. The blue line denotes an exponential fit of the normalized intensity of the probe laser. Region A and region C correspond to the beginning and the end of a single TDTR measurement, respectively. Region B relates to the maximum intensities of a single TDTR measurement.

duration of the time of the regions A and C, respectively. Next, the corrected signal Y_f is normalized as follows:

$$Y'_f = \frac{Y_f}{\bar{Y}_B}, \quad (4.4)$$

where Y'_f is the corrected TDTR signal being normalized and \bar{Y}_B corresponds to the mean TDTR signal in the region B. The normalized TDTR signal is plotted in the Figure 4.3, and can be compared to the same TDTR signal without the correction in the Figure 4.2 (right).

4.3 Extraction of the thermal conductivity from the numerical model

To convert the measured decay curves into the thermal conductivity of the membranes, a finite element method (FEM) modeling implemented using Comsol Multiphysics is used. The model reproduces the experiment with the heat flux applied to the metal pads and with constant temperature boundary conditions applied to the boundary at 200000 nm away from the pad (Figure: 4.4). Like in the experiment, the simulations monitor changes of the temperature in the aluminum pad with respect to time.

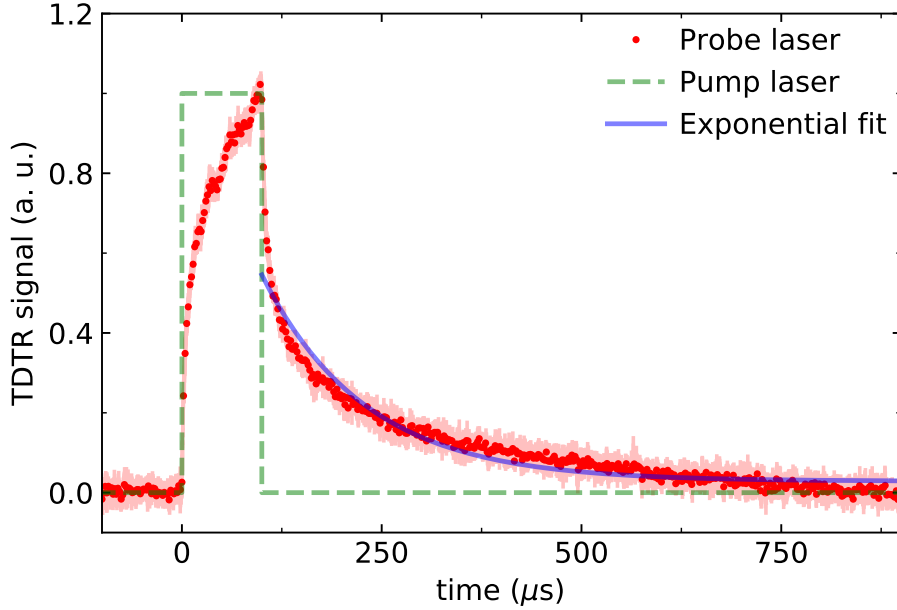


Figure 4.3: Single TDTR decay curve of a SiN membrane after the correction of offset in Figure 4.2 (right). Red dots represent the normalized signal recorded by the probe laser. Green discontinuous line indicates a single pulse of the pump laser. Blue line denotes to an exponential fit of the TDTR signal.

The same simulation is run several times for different values of the membrane thermal conductivity. Taking an example of the 50 nm film at 600 K (Figure: 4.5 left), we plot the experimental data (black dots) along with the three decay curves associated with different thermal conductivities (2 W/m/K, 3 W/m/K, 4 W/m/K) simulated in the COMSOL model. Due to the fact that the TDTR signal of a SiN membrane can not be described by an exponential function, the thermal conductivity can not be converted from the thermal decay time. We propose a strategy consisting in extracting the thermal conductivity from the integral under the thermal decay curve. We select the integral between 100 μs and 500 μs due to the fact that the TDTR signal decays nearly by 90 % in this range. The obtained dependence of the signal integral as a function of thermal conductivity is interpolated with a polynomial function (Figure: 4.5 right). Thus, the integral of the experimental decay curve is taken as a variable in the polynomial function to extract the thermal conductivity.

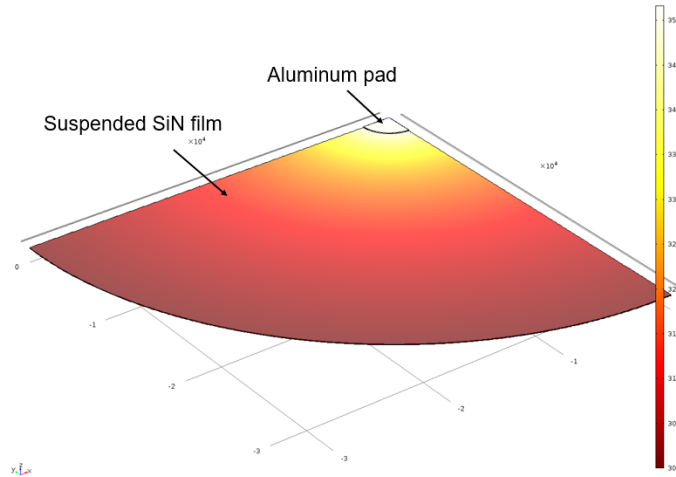


Figure 4.4: Temperature mapping of a quarter of a suspended SiN film with an Aluminum circular pad in the center as predicted by COMSOL Multiphysics.

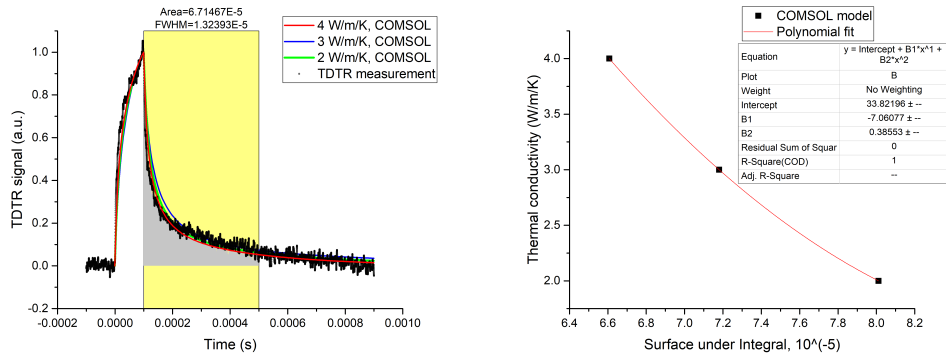


Figure 4.5: (Left) TDTR measurement compared with three decay curves predicted for different thermal conductivities using the COMSOL model. (Right) Black dots represent the signal integral between 100 and 500 μ s of selected curve versus thermal conductivity, whereas the red lines represents a polynomial function interpolating the black dots.

4.4 Conclusion

In this chapter, we provide an overview of the TDTR technique, which is based on the thermoreflectance principle that the change in reflectivity of a metal (in our case, the setup is calibrated with aluminum) at a certain wavelength is linked to its change in temperature. This technique is coupled with either a cryostat or a heating chamber which allow us to cool down to 4 K or to heat up to 600 K, respectively. We measure four different thicknesses of the suspended SiN films in the temperature interval ranging from 4 K to 600 K and extract their in-plane thermal conductivity by using a finite element method (FEM) modeling implemented using Comsol Multiphysics. To overcome the drift of probe signal at high temperature, we provide a numerical correction of the thermal decay signal. The obtained in-plane thermal conductivities will be presented and discussed in the following section.

Chapter 5

Results and discussion

5.1 Results of low temperature thermal conductivity measurements

The in-plane thermal conductivity of four different thin films (30 nm, 50 nm, 100 nm and 200 nm in thickness) have been measured versus temperature from 4 K to 300 K in a cryostat. Liquid helium is used to cool down the sample down to 4 K precisely. The pulse of the pump laser that we applied here is 10 μ s. The detector records at least 20 iterations and each iteration consists of 10^4 pulses. The experimental data of the in-plane thermal conductivity are presented in Figure 5.1. We heated up both samples by 30 K steps and, for each temperature, let the sample reach thermal equilibrium (a typical 10 minutes delay was noted).

In the 200 nm thick sample, the increase of thermal conductivity is 2.8 W/m/K when the temperature ranges from 4 K to 60 K. From 60 K to 210 K, the thermal conductivity reaches a plateau due to the predominance of phonon-boundary scattering. We observe that the measurements have a larger error bar at 120 K and we assume that this high uncertainty is related to the mechanical oscillation of the thin film.

In the 100nm thickness sample, the thermal conductivity is constantly increasing from 4 K to 180 K. The amount of enhancement in this range is 1.5 W/m/K. The phonon-boundary scattering is likely impacting in the temperature range between 180 K and 300 K, which is similar to the case of the 50 nm thick sample. Nevertheless, the plateau exists at a slightly different temperature range.

Moreover, we reveal that by heating up from 4 K to 300 K, the thermal conductivity of the 30nm thick film remains nearly constant at 1 W/m/K.

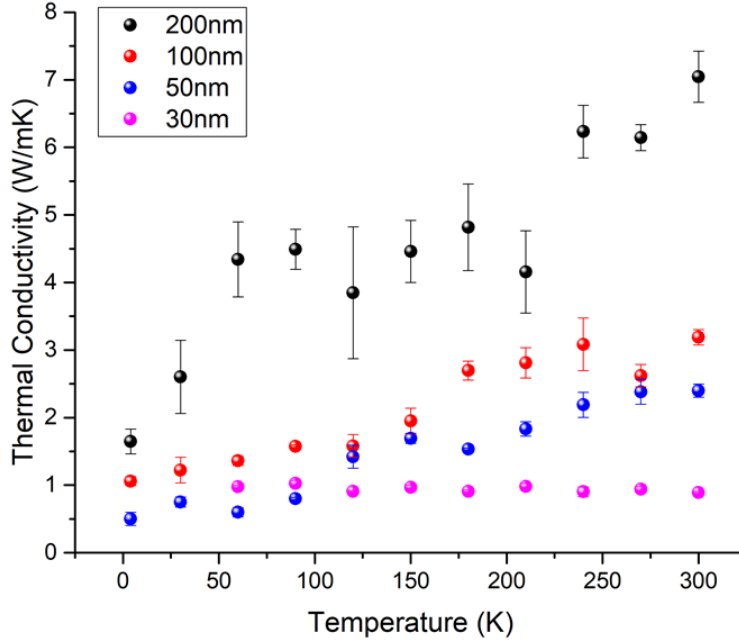


Figure 5.1: Thermal conductivity as a function of temperature of four different thickness films: 30 nm (pink dots), 50 nm (blue dots), 100 nm (red dots), 200 nm (black dots) in a temperature range of 4 K to 300 K.

5.2 Results of high temperature thermal conductivity measurements

The in-plane thermal conductivity of four different thin films (30 nm, 50 nm, 100 nm and 200 nm in thickness) have been measured versus temperature from 300 K to 600 K in a heating chamber. The pulse of the pump laser that we applied here is 100 μ s. To reduce the signal-to-noise ratio, the detector continuously records 1000 iterations where each iteration consists of 10^4 pulses. The experimental data of the in-plane thermal conductivity are presented in Figure 5.2. We heated up both samples by 30 K steps and, for each temperature, let the sample reach thermal equilibrium (a typical 10 minutes delay was noted).

For the 200 nm film, we obtained the thermal conductivity of 2.96 ± 0.041 W/m/K at 300 K. Up to 480 K, the thermal conductivity behaves as independent of temperature. A jump is observed at 510 K which may be due to the mechanical vibration of the film, leading the drift of the probe laser signal.

In the 100nm thickness sample, we observed a slight decrease from 300 K to

360 K. This drop of thermal conductivity may be caused by the Umklapp scattering. Similar trend is observed in the 50 nm film. When the temperature increases, both 100 nm and 50 nm films show strong increasing trend. Up to 510 K, the thermal conductivity of the 50 nm thick film is comparable to the ones of the 200 nm thick film. This may be the evidence of the existence of SPhPs contribution and we will discuss it in more details in a later section.

However, we observed a negligible increase (approximate 0.5 W/m/K) in the 30 nm thick film, which does not correspond to the theoretical prediction.

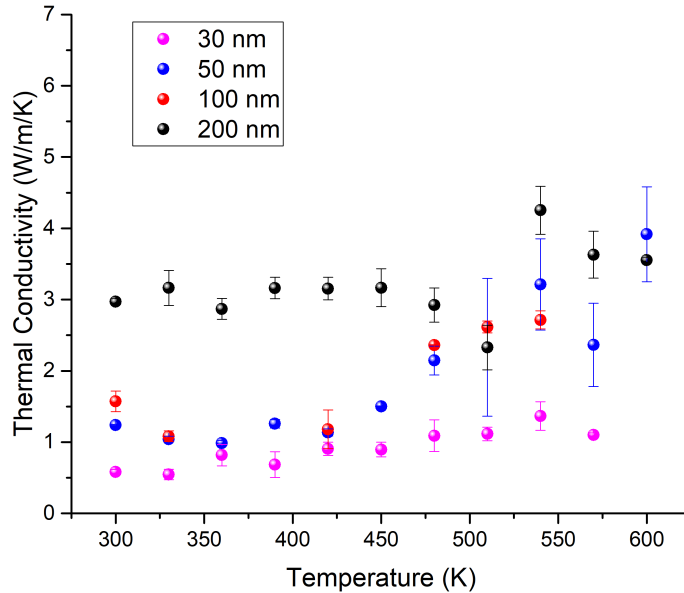


Figure 5.2: Thermal conductivity as a function of temperature of four different film thicknesses: 30 nm (pink dots), 50 nm (blue dots), 100 nm (red dots), 200 nm (black dots) in a temperature interval ranging from 300 K to 600 K.

5.3 Discussion

In the previous section, we presented the experimental results of the thermal conductivity of SiN thin films with four different thicknesses obtained by TDTR measurements. The thermal conductivity that we obtained is a total quantity, which includes the phonon contribution and the SPhPs ones. A consistent increase of thermal conductivity is observed both in the 50 and the 100 nm thick films from 420 K up to 600 K, whereas in the 200 nm film temperature independence is observed. This behavior with thickness-dependence can not be fully explained by the phonon contribution and it is considered as a poten-

tial evidence of the existence of the SPhPs contribution. However, it requires a quantitative analysis to confront the analytical model and the experimental results.

The analytic model presented in the previous chapter is merely based on the contribution of SPhPs. To date, limited reports provide the phonon contribution to thermal conductivity of SiN films of given thickness. This lack of reference raises the difficulty to evaluate the SPhPs contribution and furthermore to compare it with our analytical expectation. From Figure 5.2, we assume that the thermal conductivity obtained at 300 K is purely contributed by phonons (0.5 W/m/K for 30 nm film, 1.2 W/m/K for 50 nm film, 1.5 W/m/K for 100 nm film and 2.9 W/m/K for 200 nm). These assumed values are in the range of agreement with the ones reported by [Lee and Cahill \(1997\)](#) and [Griffin Jr et al. \(1994\)](#). Assuming those data as valid, we subtract the phonon contribution to thermal conductivity and plot the Figure 5.3 to visualize the SPhPs contribution.

In the Figure 5.3, we compare the analytic prediction and the experimental results. The SPhPs contribution of the 200 nm film is nearly negligible, which correlates to the theoretical prediction below 500 K.

We witness the potential evidence of the SPhPs contribution in the 100 nm thick film. When the sample is heated up to 480 K, a consistent increase of thermal conductivity appears with approximate values as predicted in our model. An increasing trend is found in the 50 nm thick film starting from 420 K up to 600 K, whereas a similar trend was obtained in the theoretical model. Nevertheless, a discrepancy (approximately 3 W/m/K) is observed between the experimental data and the theoretical prediction. Moreover, our theoretical model predicted a dramatic increase in the 30 nm thick film, but such increase has not been observed in the experimental measurement.

These results imply that the SPhPs contributions qualitatively exist in the 100 and the 50 nm thick film. However, the absolute values of the SPhPs contribution may be overestimated in the 50 and the 30 nm thick films. In our analytical model, the dielectric constant is assumed to be independent from the temperature and thickness. However, this assumption may lead to the underestimation of the absorption in the dielectric film. From the other hand, we assume the SPhPs modes are thermally excited through the lattice vibration in the membrane. The phonon temperature is equivalent to the SPhPs temperature and the energy is conserved during the transfer. These two factors are not explored in the analytical model, thus may lead to the overestimation in the SPhPs contribution to the thermal conductivity.

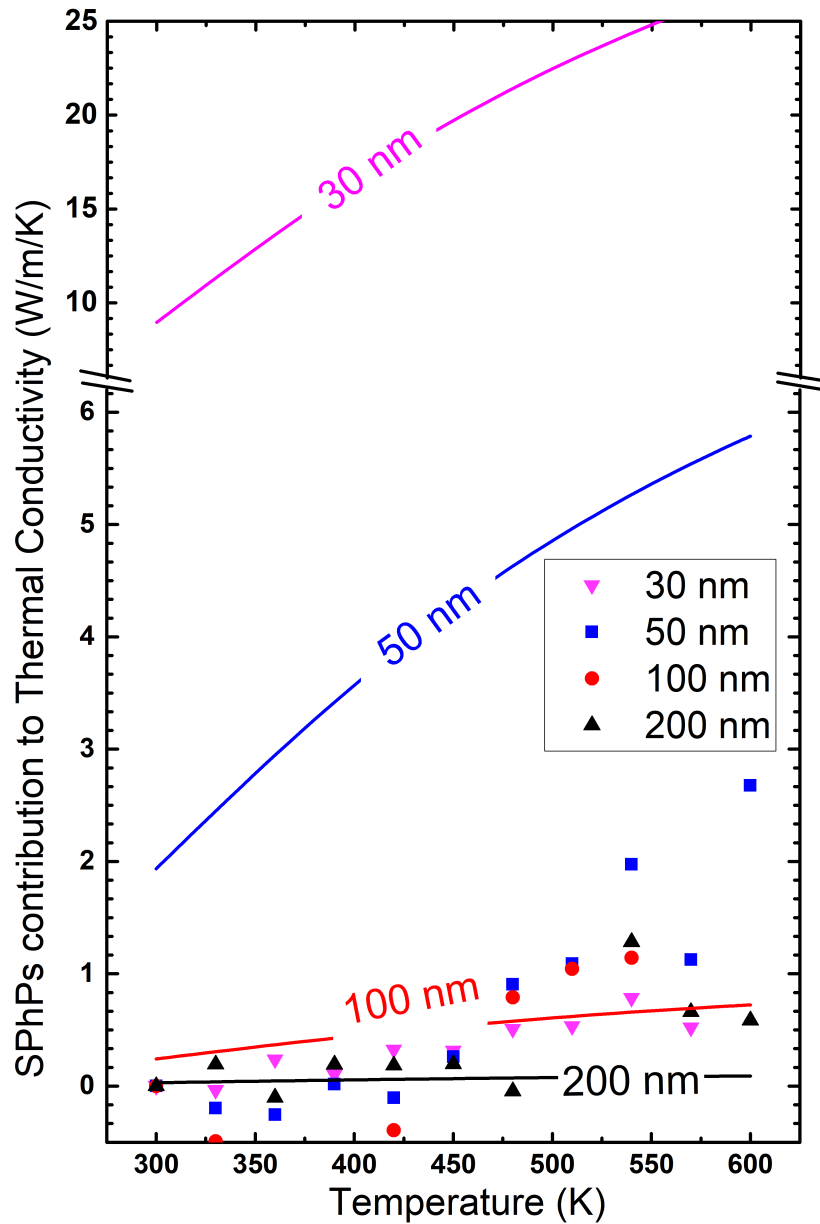


Figure 5.3: Comparison between the analytical model and the experimental results of the SPhPs contribution to thermal conductivity as a function of temperature. Continuous lines represent the calculation from theoretical model with four different thicknesses: 30 nm (pink line), 50 nm (blue line), 100 nm (red line) and 200 nm (black line). The solid dots stand for the experimental results of four different thicknesses: 30 nm (pink triangle), 50 nm (blue square), 100 nm (red circle) and 200 nm (black triangle). A bar break at 6 W/m/K at the vertical axis should be noticed and it assists to visualize our analytical model of the 50 nm and the 30 nm thick film.

Figure 5.4 reports the normalized thermal conductivity as a function of temper-

ature. The data indicate the increase of relative thermal conductivity for thinner membranes. However, the thermal conductivity of the 200 nm film shows nearly independence of temperature. The error bars represent the standard deviation of three individual measurements performed on the same membrane. The uncertainty may result from the mechanical vibration of the membrane and the drifting of background of the probe laser signal. In addition, the pump laser power is slightly tuned in order to obtain a better signal-to-noise ratio. The uncertainty does not allow us to clearly compare the trend with different thicknesses. Perspectively, the future study should be conducted on different membranes with the same thickness to reduce the uncertainty.

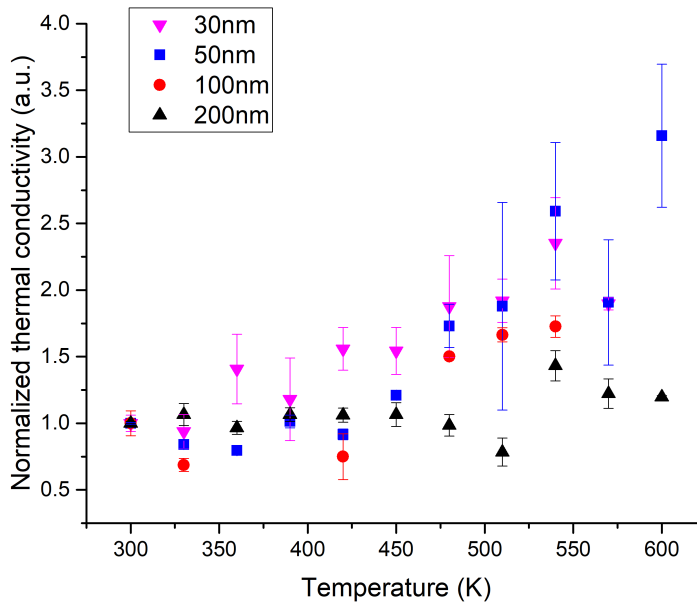


Figure 5.4: Normalized thermal conductivity of the experimental results as a function of temperature. The solid dots stand for the experimental results of four different thicknesses: 30 nm (pink triangle), 50 nm (blue square), 100 nm (red circle) and 200 nm (black triangle).

Last but not least, we applied a longer duration of the pump laser in the high temperature measurement campaign to make the temperature uniform on the entire metal pads and thus minimize the metal pads gradient in the thermal decay curve. The different durations potentially cause the discontinuity of the thermal conductivity between the low and high temperature measurements. In order to ensure consistent measurement, the conditions of the experimental protocol, the optical objective and the acquisition time also should be maintained.

5.4 Conclusion

The results discussed above lead to the fact that the SPhPs contribution to thermal conductivity has a significant dependence on the thickness and temperature of the dielectric film. The high temperature thermal conductivity measurements reveal that the SPhPs contribution to thermal conductivity is reversely proportional to the film thickness. The result for the 200 nm thick film quantitatively satisfy this analytical prediction. From the other hand, a clear increase of thermal conductivity in the 30 nm and the 50 nm thick films is observed. This enhancement of thermal conduction becomes potential evidence of the SPhPs existence. Nevertheless, the coupling efficiency between the phonons temperature and the SPhPs temperature should be explored in the analytical model.

Part III

Investigation of phonon transport in nanostructured thin films: Phononic Crystals and Thermoelectric Alloys

Chapter 6

Introduction of Phononic Crystals

6.1 Phononic Crystals: heat conduction and heat convection

Since the end of the nineties, phononic crystals have been extensively studied for their acoustic transmission. More recently, they have also been viewed as a promising configuration to design phonon heat conduction by tailoring the phonon mean free path such as in silicon (6.1).

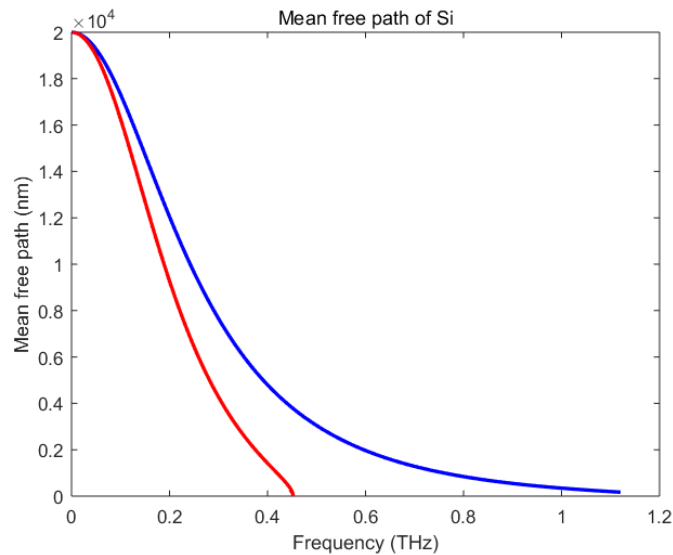


Figure 6.1: Phonon mean free path spectra of silicon at room temperature: longitudinal acoustic modes (blue line) and transversal acoustic modes (red line).

A Phononic Crystal (PnC) is the analog of a photonic crystal where a periodic

structuration introduces a super-period and the folding of the photon dispersion. In photonic crystals, the opening of a band gap is targeted to modify the transmission properties of the system.

However, producing wave interference between thermal phonons remains difficult. It was for instance proven that phonon wave effects do not take place beyond 17K in silicon. Therefore, thermal conduction in PnC mostly results from scattering with the periodic pattern as a usual boundary scattering. While many studies have proposed thermal conductivity measurements of PnCs, none of them have rigorously treated the impact of heat losses. Losses via convection and radiation are however expected to be significant due to the increase of exchange surface.

We propose a complete treatment of the coupled heat transfers occurring in PnCs including experimental (via Raman thermometry) and theoretical analysis. This approach covers boundary scattering effect on heat conduction as well as convection and radiation losses.

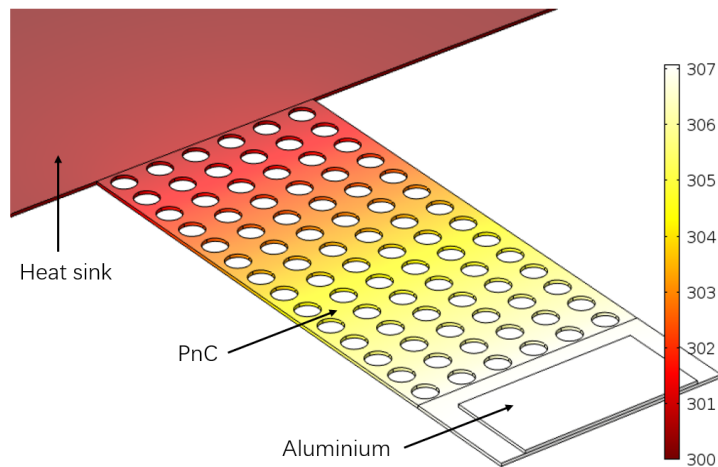


Figure 6.2: *Temperature map in two dimensional phononic crystal simulated by COMSOL Multiphysics. A continuous laser applied on the Aluminium pad to generate heat propagating along the phononic crystal into the heat sink. The coloured bar (with unit in kelvin) indicates the temperature in the whole structure.*

In this chapter, we investigate the reduction of thermal conductivity by holey phononic patterning on silicon thin film at room temperature. We quantify the neck size and hole size effects by analytical models developed from the heat diffusion equation. Furthermore, the impact of air convection will be discussed independently based on experimental measurements done both in vacuum and

in ambient conditions.

In PnCs, the main physical quantity to be tuned is the phonon mean free path. When the characteristic length of the system is equivalent or smaller than the phonon mean free path, boundary scattering is increased and phonon thermal conductivity is impeded.

6.2 Analytical model for heat dissipation by conduction and convection

To understand the full functionality of thermal reduction in phononic crystal, it is essential to have an analytical model considering different types of phonon scattering processes. Additionally, for PnCs which serves for thermoelectric device, the operation temperature is usually far beyond room temperature and the device is exposed in air. In fact, heat radiation and convection is not negligible when we analyse heat dissipation in phononic crystal. However, we lack of an analytical model taking all these factors into account.

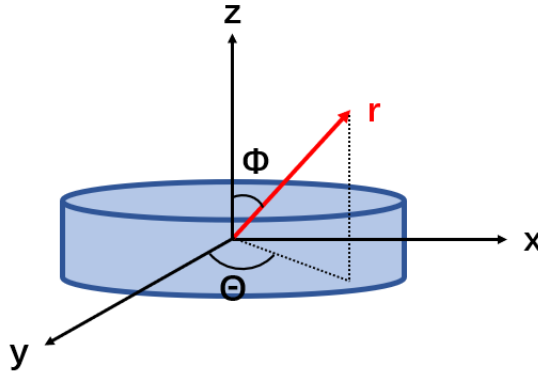


Figure 6.3: Schematic of the modelled cylinder system. r refers to the radial distance, θ is the polar angle, and ϕ is the azimuthal angle in spherical coordinate.

To simplify the problem, we firstly study heat conduction in a spherical disk (shown in figure 6.3) surrounded by air. The structure is homogeneous and in steady state and the heat diffusion equation in spherical coordinate can be written as:

$$0 = \frac{1}{r} \frac{\partial}{\partial r} \left(r \kappa \frac{\partial T}{\partial r} \right) + \frac{1}{r^2} \frac{\partial}{\partial \phi} \left(\kappa \frac{\partial T}{\partial \phi} \right) + \frac{\partial}{\partial z} \left(\kappa \frac{\partial T}{\partial z} \right) + \dot{Q}, \quad (6.1)$$

where r is the radial distance, ϕ is the azimuthal angle in cylindrical coordinates, z is the height, κ is thermal conductivity, T is the temperature, \dot{Q} is the rate of heat dissipation, ρ is the volumic mass density and c is specific heat capacity.

To have a model approach to conventional thermal characterization such as Time domain thermoreflectance or Raman spectrometer, we assume that the disk is heated up by a disk of radius r_0 in the center of the upper main disk. Since the disk is thin enough, the temperature gradient in the out-of-plane direction is negligible and heat flux propagates only in the radial direction. Taking into account the azimuthal symmetry and the losses via the heat transfer coefficient h , the rate of heat flow (in Watts) due to natural convection from both sides of the disk expressed by Newton's law of cooling as:

$$\dot{Q} = \frac{2h}{S}(T_s - T_\infty) \quad (6.2)$$

where h is the heat transfer coefficient, S is the effective surface of disk, T_s is the temperature of the disk and T_∞ is the temperature of surroundings.

Equation 6.1 leads to the following equation:

$$0 = \frac{1}{r} \frac{d}{dr} \left(r \frac{\partial T}{\partial r} \right) - \frac{2h}{S\kappa} T + \frac{P}{\kappa} \quad (6.3)$$

where d is the membrane thickness, T is the temperature difference between sample and surrounding $T = T_s - T_\infty$, and P refers to the Gaussian distribution of laser power intensity $P = \frac{2P_0}{\pi r_b^2} \exp(-\frac{2r^2}{r_b^2})$ with r_b the radius of the laser beam.

This second order differential equation has solutions known as Bessel's equations. It yields the solutions that are linear combinations of Bessel functions of first and second kinds.

$$T_s(r) = AI_0(mr) + BK_0(mr), \quad (6.4)$$

$$m^2 = \frac{2h}{S\kappa}, \quad (6.5)$$

where I_0 and K_0 are the 0th order of the first and second kind Bessel functions, respectively. A and B correspond to arbitrary constants.

In order to set the constant, two boundary conditions are applied:

1) the temperature is set to the room temperature 300 K at the system boundaries when $r=L$:

$$T(r = L) = T_{\infty}, \quad (6.6)$$

2) the excitation heat flux is generated homogeneously where $r < r_0$ and at $r=r_0$ the heat flux follows the continuity condition:

$$-\kappa \left. \frac{\partial T(r)}{\partial r} \right|_{r=r_0} = \frac{P_0}{2\pi r_0 t}. \quad (6.7)$$

where P_0 is the heating power of the laser.

By applying these two boundary conditions, we found that the two constants A and B take the following form:

$$A = \frac{T_{\infty} - BK_0(mL)}{I_0(mL)}, \quad (6.8)$$

$$B = \frac{T_{\infty}I_1(mr_0) + \frac{P_0I_0(mL)}{2\pi r_0^2 \kappa m t}}{K_0(mL)I_1(mr_0) + K_1(mr_0)I_0(mL)}, \quad (6.9)$$

where I_0 and I_1 are the zero and the first order of the first kind of solution to the Bessel's equation, respectively, K_0 and K_1 are the zero and the first order of the second kind of solution to the Bessel's equation, respectively.

So far, we have constructed an analytic model which provides the insight of heat conduction of phononic crystal. In this model, two critical characters require more detail analysis: the thermal conductivity and heat transfer coefficient.

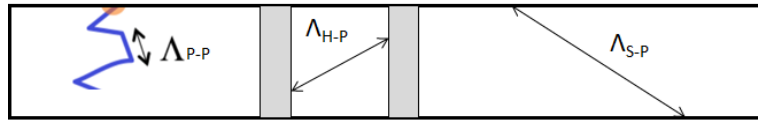


Figure 6.4: Phonon scattering in PnCs is contributed by three processes: phonon-phonon scattering Λ_{P-P} , phonon-hole scattering Λ_{H-P} and surface-phonon scattering Λ_{S-P} .

Phonon scattering in PnCs is contributed by three processes (shown in Fig. 6.4): phonon-phonon scattering, phonon-hole scattering and surface-phonon scattering combined using Matthiesen's rule:

$$\frac{1}{\tau} = \frac{1}{\tau_{p-p}} + \frac{1}{\tau_{h-p}} + \frac{1}{\tau_{s-p}}, \quad (6.10)$$

where τ is total relaxation time, τ_{p-p} , τ_{h-p} and τ_{s-p} are the relaxation time associated with phonon-phonon scattering, hole-phonon scattering and surface-phonon scattering, respectively.

We can further derive the thermal conductivity from relaxation time formulation through the kinetic model. Umklapp scattering is the dominant process in phonon-phonon scattering process at high temperatures for low defect crystals. The thermal conductivity for an insulating crystal where the U-processes are dominant has $1/T$ dependence. Consequently, following the phonon gas model and a grey approximation, the thermal conductivity can be expressed as proportional to relaxation time tau as follows:

$$\frac{1}{\kappa} = f_{p-p}T + \frac{f_{h-p}}{n} + \frac{f_{s-p}}{t}, \quad (6.11)$$

where f_{p-p} , f_{h-p} and f_{s-p} are three fitting parameters corresponding to phonon-phonon, hole-phonon and surface-phonon scattering process, respectively. Hole-phonon and surface-phonon scattering are indeed both governed by their corresponding geometrical parameters of neck n (shortest distance between two holes) and film thickness t .

Considering the disk is heated up in the central region $r < r_0$ and exposed simultaneously to cold air, the both surfaces of disk are cooled down by natural convection. Natural convection on the surface depends on the geometry of the surface as well as its orientation.

$$Pr = \frac{\nu}{\alpha}, \quad (6.12)$$

where ν is the kinematic viscosity and α is the thermal diffusivity.

$$Gr = \frac{\beta(T_s - T_\infty)gL_c^3}{\nu^2}, \quad (6.13)$$

where β is the coefficient of thermal expansion with $\beta = 2/(T_s + T_\infty)$, g is the gravitational acceleration ($g = 9.8m/s^2$), L_c is the characteristic length ($L_c = L/2$) with L is the radius of the disk.

Rayleigh number is a product of the Grashof number and Prandtl number. for natural convection,

$$Ra = Gr \cdot Pr, \quad (6.14)$$

For a horizontal plate, the Nusselt number in convection is in the following form:

$$Nu = 0.54Ra^{1/4}, \quad (6.15)$$

To sum up all the consideration above, one obtains a heat transfer coefficient in the following expression:

$$h = \frac{Nu \cdot \kappa_{air}}{L_c}, \quad (6.16)$$

Here, we implement a fitting parameter f_{conv} to adapt the Equation 6.16 as follows:

$$h = f_{conv} \left(\frac{T - T_\infty}{T + T_\infty} \right)^{\frac{1}{4}} \quad (6.17)$$

This fitting parameter allows us to quantify the heat loss due to the air convection.

6.3 Conclusion

In this chapter, we developed an analytical model by taking into account the heat conduction and heat convection in a horizontal placed porous membrane. The three types of phonon scattering mechanisms (Umklapp, phonon scattered with the surface, phonon scattered with the boundary) can be investigated individually through three tunable parameters. By including the factor of heat transfer coefficient, we will be able to quantify the air convection based on different geometry. The numerical analysis will be carried on in the next chapter.

Chapter 7

Fabrication and thermal characterization of porous membrane

7.1 Sample design and fabrication

The sample fabrication and thermal characterization were implemented by our partners of the group of Professor Sotomayor. These processes are reported in our publication [Graczykowski et al. \(2017\)](#).

The fabrication processes of silicon-based phononic crystal mainly consist of electron beam lithography and reactive ion etching. The square lattice holes on the membranes were fabricated using the standard top-down approach: First, the positive resist (AR-P) for electron beam lithography was spin-coated on the membranes for 60 seconds at 4000 rpm. Then, the resist was baked at 150 degrees celsius for one minute. Electron beam lithography (Raith 150-TWO) was used to pattern the holes in multiple locations on the membranes (shown in figure 7.1). To develop the exposed regions of the resist, AR 600-546 developer was applied for one minute, followed by one minute of post-baked process at 130 °C. This step additionally hardened the mask before the reactive ion etching. After the lithography and post-baked processes, the samples were placed in Alcatel AMS-100DE for a 60 s etching process. Finally, the samples were placed in a plasma system (PVA Tepla) and cleaned in 50 sccm O₂ at 400 W for one minute. As shown in figure 7.1, a high-resolution scanning electron microscope was used to measure the diameter of the holes (shown in table 7.1). Further details related to this fabrication process are reported in [Sledzinska et al. \(2016\)](#).

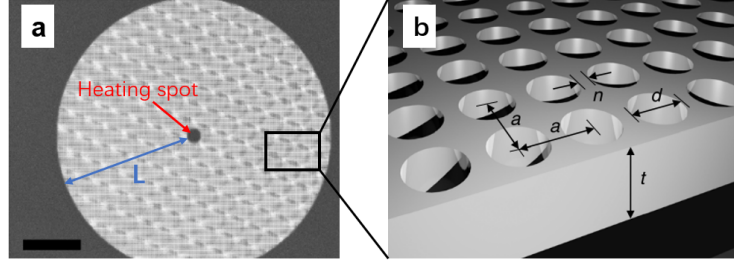


Figure 7.1: (a) SEM image with a scale bar of $20 \mu\text{m}$ in length and (b) insight. The disk with thickness t is patterned with square lattice holes with diameter d , neck distance n and periodicity a (Graczykowski et al. (2017)).

	thickness (nm)	hole diameter (nm)	neck distance (nm)
membrane	250	-	-
PnC_1	250	135	165
PnC_2	250	140	110
PnC_3	250	130	70

Table 7.1: The hole diameter and neck distance of holey phononic crystal samples are characterized by a high-resolution SEM.

7.2 Thermal characterization by two-laser Raman thermometry

The two-laser Raman thermometry (2LRT) is a thermal characterization tool coupling a heating laser with a conventional Raman spectroscopy, which detects the vibrational, rotational and low-frequency modes in solid-state system. 2LRT is a contactless technique suitable to measure the thermal conductivity of nanowires, free-standing membranes (Reparaz et al. (2014)), thin films on a given substrate, and bulk samples. This technique is based on detecting the temperature dependent Raman spectra of a given material and convert the Raman shift to temperature in the material through calibration. A linear fitting (in figure 7.2 (a)) indicates the slope of $-43.43 \pm 0.5 \text{ K}(\text{cm}^{-1})^{-1}$, which is used to convert Raman shift into temperature.

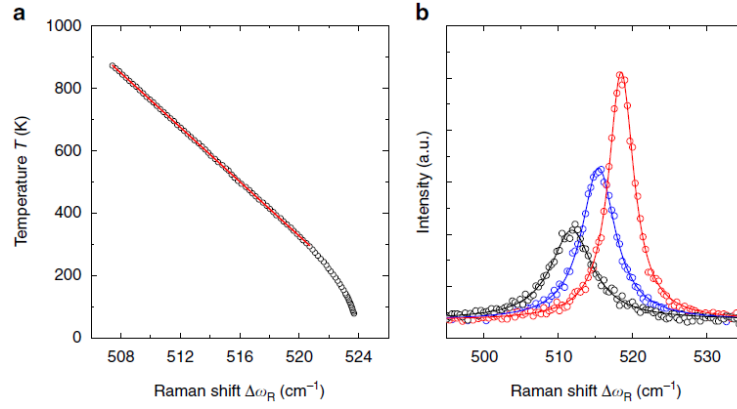


Figure 7.2: The two-laser Raman thermometry calibration. (a) Temperature versus the silicon longitudinal optical phonon frequency. (b) Raman shift due to the temperature increases.

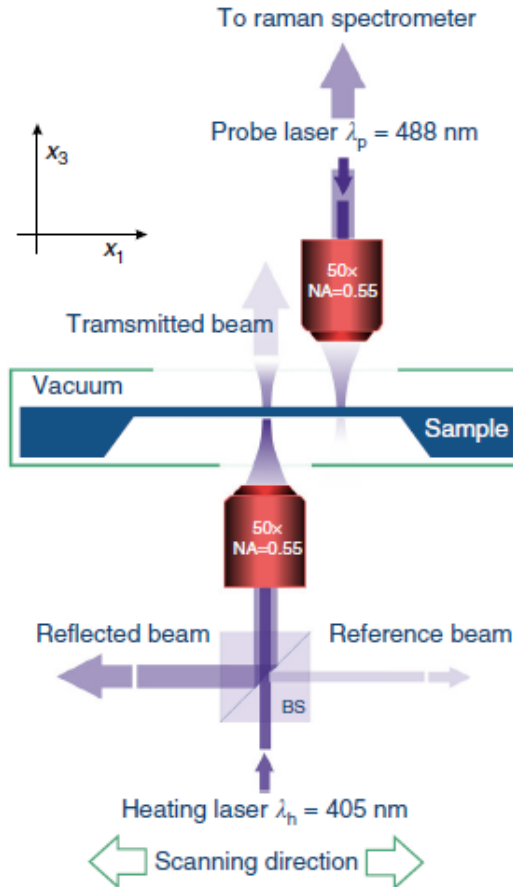


Figure 7.3: Schematic of the Raman thermometer: a heating laser with wavelength 405 nm continuously heats up the center of the sample, meanwhile a probe laser with wavelength 488 nm simultaneously scans the sample surface in the in-plane direction. The probe laser has low intensity and only heats up the sample within 5 kelvins and the reflected signal is guided into the Raman spectrometer to detect the temperature vibrational modes. This measurement can be performed in vacuum or in ambient conditions (Graczykowski et al. (2017)).

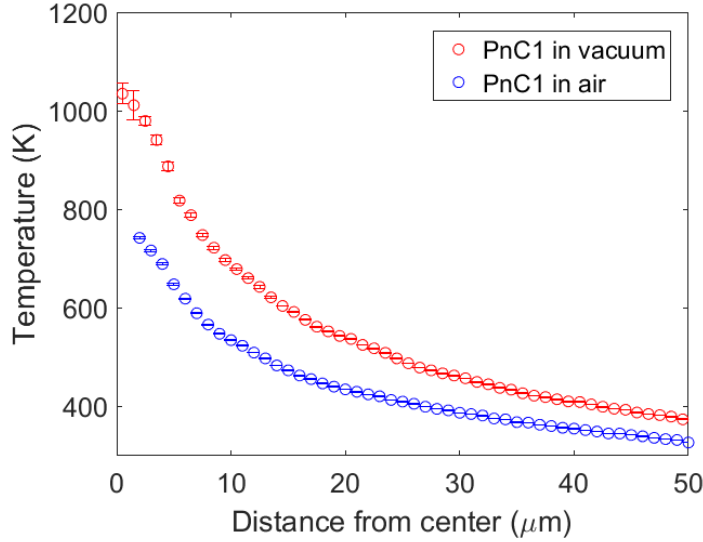


Figure 7.4: Two-laser Raman thermometry result of PnC1 sample: measurement in vacuum (red circle) and in air (blue circle).

For PnCs samples, a central region with a diameter about $5 \mu\text{m}$ has no pattern and it serves as an heating island. A heating laser with wavelength 405 nm continuously heats up the central region of the sample. Heat flux generates in the center and propagate along the in-plane radical axis. The samples are thin enough and the temperature gradient in the out-of-plane axis is negligible. Meanwhile a probe laser with wavelength 488 nm scans the sample surface along the radical. The temperature-dependence Raman shift is recorded and converted into temperature increased in the sample.

The lateral temperature profile of the phononic crystal sample PnC1 (with periodicity $a=300 \text{ nm}$ and hole diameter $d=130 \text{ nm}$) is shown in figure 7.4. From this figure, we notice that the heat losses caused by the presence of air is not negligible, even though the air has low thermal conductivity of $2.623 - 6.763 \times 10^{-2} \text{ W/m/K}$ [Kadoya et al. \(1985\)](#). Later, we will quantify the heat losses in air through the analytic model we developed in the previous chapter.

7.3 Conclusion

In this chapter, we briefly review the fabrication process of the periodic porous silicon suspended membrane and the two-laser Raman thermometry (2LRT). The different periodicity is designed to study the reduction in thermal transport based on diffusive phonon-boundary scattering and air-mediated losses. Furthermore, the thermal properties are characterized by a contactless 2LRT above room temperature. The experimental results will be presented in the

next chapter and coupled with the analytic model developed in the previous chapter.

Chapter 8

Determining the Phononic Crystal thermal properties

8.1 Setting the PnC thermal conductivity parameters in vacuum

To fit the thermal conductivity parameters, equation 6.4 including the thermal conductivity of equation 6.11 was solved to provide a radius dependent temperature profile. This profile was then confronted to the measured one by 2LRT, which is depicted in figure 8.1. Up to this point, we have considered only measurements performed in vacuum, i.e., where heat loss due to the air convection is negligible. In order to define each fitting parameter, we start the fitting with the temperature profile of silicon membrane measured in vacuum (shown in figure 8.1 (a)). In this primary fitting step, due to the fact that no hole is presented in the sample, only f_{p-p} and f_{s-p} are tunable, i.e. only the Umklapp and surface-phonon scattering processes are taken into account in the membrane sample. From the best fit, we extract the values of f_{p-p} and f_{s-p} correspond to the temperature dependence and the surface-phonon scattering effect regarding to 250 nm thick membrane.

Consequently, the fitted parameters obtained for the pristine membrane, f_{p-p} and f_{s-p} , yielding the data of Figure 8.1 (a), were then reinjected in the PnC models as shown in Figures 8.1 (b)-(d), where the only tunable parameter is f_{h-p} , which is correlated to the hole diameter.

From Figure 8.1 (a)-(b), the analytical model has good agreement with the experimental data. A consistent decay is observed from the heating center to the edge of the membrane. However, in Figure 8.1 (c)-(d), a shape temperature decay occurs near the laser heating spot ($r = 5\mu m$) and it may be due to the different effective thermal conductivity in silicon membrane and porous membrane.

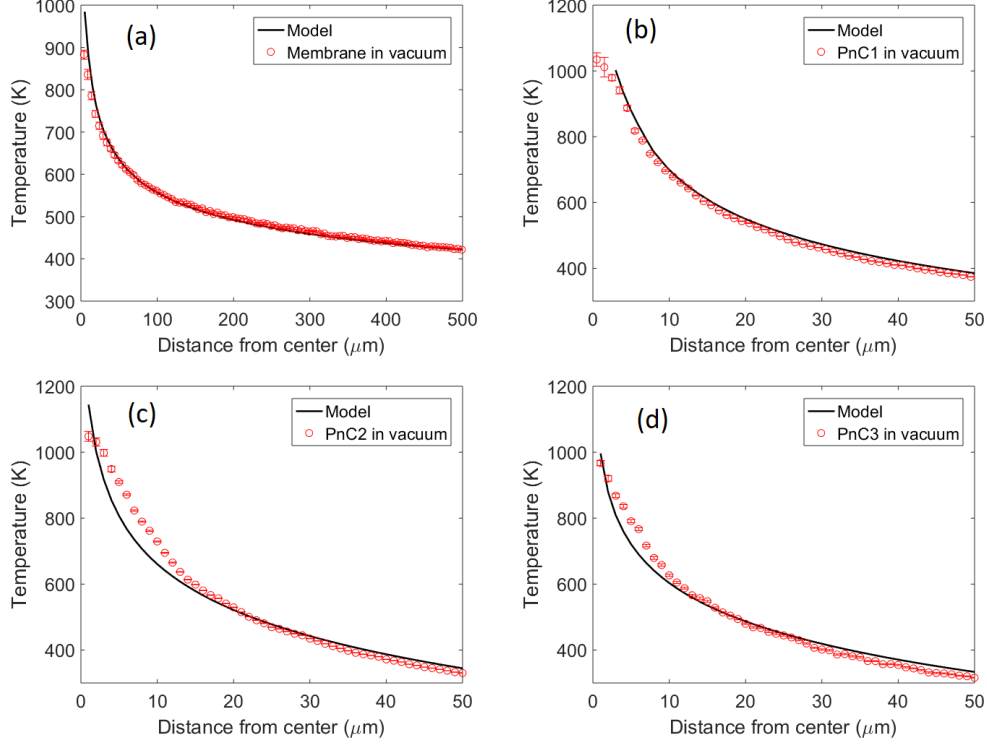


Figure 8.1: Experiment vs. model fitting results: (a) 250 nm thick silicon membrane; (b) sample PnC1 with lattice parameter of $a = 300$ nm and hole diameter of $d = 135$ nm; (c) sample PnC2 with lattice parameter of $a = 250$ nm and hole diameter of $d = 110$ nm; (d) sample PnC3 with lattice parameter of $a = 300$ nm and hole diameter of $d = 130$ nm. The red circles represent experimental data measured in vacuum and black lines represent our analytical model.

8.2 Setting the PnC thermal convection parameters in air

The temperature profiles measured by 2LRT in air are displayed in the figure 8.2. Analogically to the analysis of the temperature profile in vacuum, the one in air remains dependent on the same phonon scattering parameters. Consequently, the three fitting parameters f_{p-p} , f_{s-p} and f_{h-p} are considered as constants and are implemented in the analysis including heat convection. Here, we applied fitting parameter f_{conv} to that we developed in the previous chapter:

$$h = f_{conv} \left(\frac{T - T_{\infty}}{T + T_{\infty}} \right)^{\frac{1}{4}} \quad (8.1)$$

where h is the heat transfer coefficient, f_{conv} refers to the fitting parameter responsible for air convection and T_{∞} stands for the room temperature.

The fitting process is similar to previous case for vacuum measurement. We start the fitting with the temperature profile of silicon membrane measured in air (shown in figure 8.2 (a)). In this primary fitting step, we implement f_{p-p} and f_{s-p} from the fitting of 8.1 (a) and extract the heat loss factor f_{conv} , i.e. the Umklapp and surface-phonon scattering processes are consistent in air and in vacuum, the only dependence lies on the temperature and the thickness of the membrane. Differing from the cases in vacuum, the fitting parameter f_{conv} is correlated to the hole diameter.

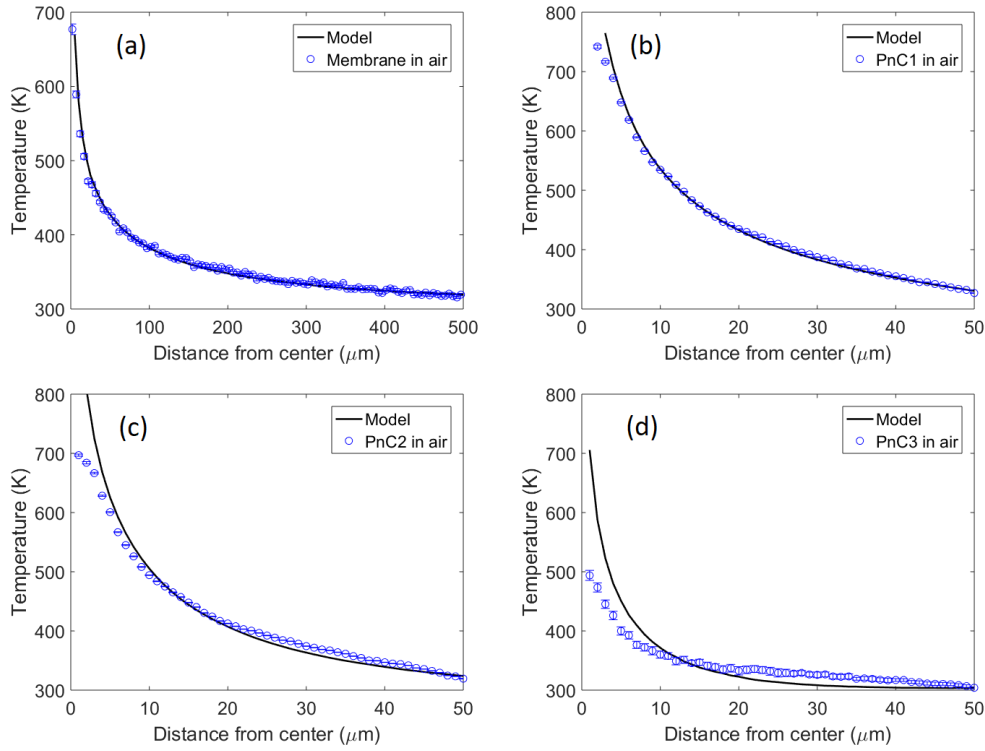


Figure 8.2: Experiment vs. model fitting results including air convection: (a) 250 nm thick silicon membrane; (b) sample PnC1 with lattice parameter of $a = 300$ nm and hole diameter of $d = 135$ nm; (c) sample PnC2 with lattice parameter of $a = 250$ nm and hole diameter of $d = 110$ nm; (d) sample PnC3 with lattice parameter of $a = 300$ nm and hole diameter of $d = 130$ nm. The blue circles represent experimental data measured in air and black lines represent our analytical model.

8.3 Discussion

A first simple Fourier heat conduction analysis yields the temperature dependent thermal conductivity from experimental data. This thermal conductivity can

be approximated by a simple power law:

$$\kappa(T) = \alpha T^{-\beta} \quad (8.2)$$

where α and β are fitting parameters that we determine from fitting. For 250 nm thick silicon membrane at 300 K, we found that its thermal conductivity is 83 W/m/K, which is close to the value reported in Cuffe et al. (2015). As can be seen in figure 8.3, the temperature dependence of thermal conductivity becomes weaker with decreasing the neck distance. The phononic crystal with 165 nm neck distance corresponds to 0.74 as temperature dependence factor of thermal conductivity (shown in table 8.1). When the neck distance shrinks to 70 nm, the temperature dependence factor reduces to 0.11. The reduction of the temperature dependence is due to the fact that the phonon-hole scattering process becomes predominance among three scattering processes. At room temperature, the phonon mean free path is approximate 100 nm, which is comparable to the neck distance in PnC2 (with 110 nm neck distance) and PnC3 (with 70 nm neck distance). The geometrical confinement occurs mostly in the neck region and leads to the PnC2 and PnC3 have less influence of Umklapp scattering process.

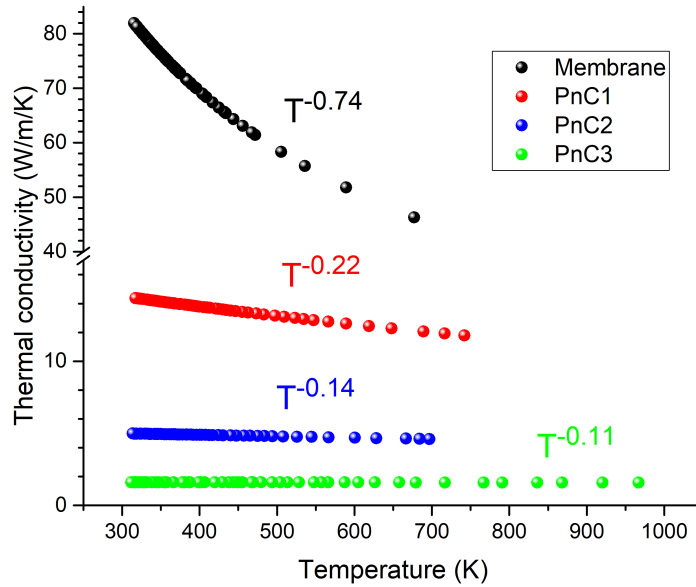


Figure 8.3: Thermal conductivities of a 250 nm thick silicon membrane and three phononic crystals as a function of temperature. Temperature dependence is weaker for the phononic crystal with smaller neck distance.

The surface-to-volume ratio is calculated as follows:

$$\frac{S}{V} = \frac{2a^2 - \frac{\pi}{2}d^2 + \pi dt}{a^2t - \frac{\pi}{2}d^2t} \quad (8.3)$$

where a refers to the periodicity, d is the hole diameter and t is the thickness of the membrane.

From the table above, we obtain the surface-to-volume ratio related to the three porous samples: 0.0136 for PnC1, 0.0173 for PnC2 and 0.0232 for PnC3. The heat transfer coefficient obtained through the fitting parameter f_{conv} is plotted in Figure 8.4 as a function of temperature, showing that the larger the surface-to-volume ratio leads to the stronger the temperature dependence of the porous membrane. This can be explained by a larger surface-to-volume ratio may allows free air flow through the holes and significant increase the cooling efficiency.

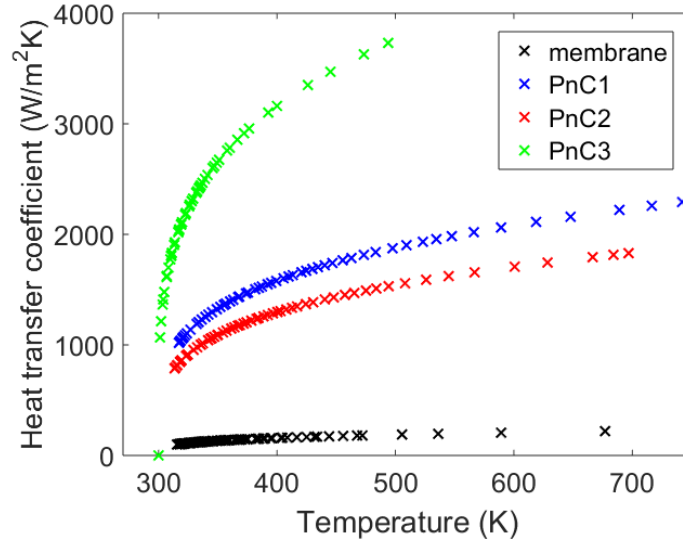


Figure 8.4: Heat transfer coefficient of a 250 nm thick silicon membrane (black cross) and three types of phononic crystals: PnC1 with lattice parameter $a = 300$ nm and hole diameter $d = 135$ nm (blue cross); PnC2 with lattice parameter of $a = 250$ nm and hole diameter $d = 110$ nm (red cross); PnC3 with lattice parameter $a = 300$ nm and hole diameter $d = 130$ nm (green cross).

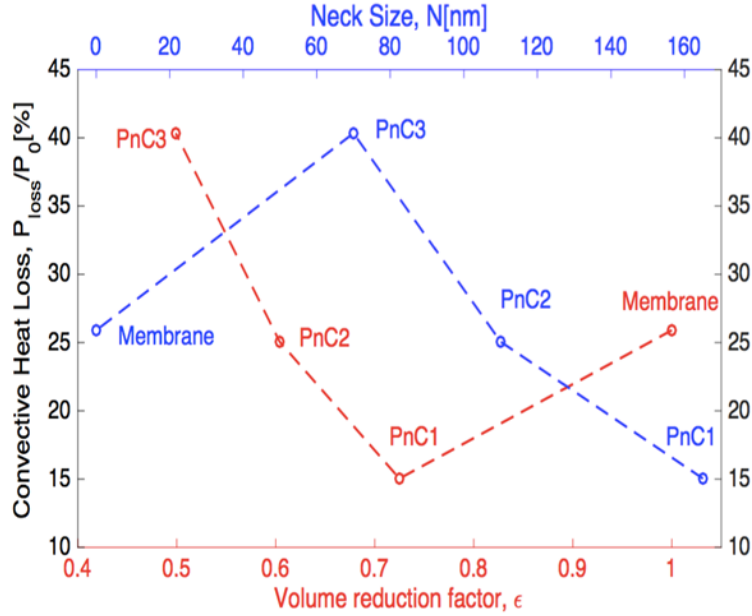


Figure 8.5: Convective heat loss in percentage as a function of neck distance (blue discontinuous line) and of volume reduction factor (red discontinuous line).

Shown in Figure 8.5, the PnC3 sample can reach more than 40 % by air convection.

	neck distance (nm)	surface to volume ratio (nm^{-1})	excitation power (mW)	thermal conductivity temperature dependent	power loss with convection (%)
membrane	-	0.008	7.125	-0.74	25.9
PnC_1	165	0.0136	3.57	-0.22	15.03
PnC_2	110	0.0173	1.474	-0.14	25.06
PnC_3	70	0.0232	0.419	-0.11	40.33

Table 8.1: Neck distance, volume reduction factor, excitation power, thermal conductivity with temperature dependence and power loss of silicon membrane and phononic crystals.

8.4 Conclusion

In this chapter, we investigate the heat conduction and convection in phononic crystal through an analytical model. The model is coupled with the experiment designed to use the two laser Raman thermometry to measure the temperature profile of porous silicon membranes in air and in vacuum. We show that the thermal conductivity can be significantly suppressed by reducing the neck size of

the porous membrane. Furthermore, we determine the heat dissipation through air convection and show that it can be significantly tuned by designing the surface-to-volume ratio.

Chapter 9

Photothermal Radiometry

Non-destructive and accurate measurement is required to characterize the thermal properties of the bulk materials or thin layered samples. In this chapter, an overview of the photothermal radiometry (PTR) technique is provided. An analytical model based on the heat conduction equation in mono- and double layers of an opaque sample is developed. Numerical evaluation provides an experimental guide for modulation frequency measurement.

9.1 Introduction

Accurate characterization of the thermo-physical properties such as the thermal conductivity, thermal diffusivity, and heat capacity of thin films and superlattices is essential for the electronics industry today to characterize the thermal performance of the isolation layer and its durability. Potentially the widespread use of a layered structure exists in various applications such as lasers, LEDs, thermal barrier coatings, thermoelectric devices, etc.

Photothermal radiometry (PTR) method is based on the laser excitation and the infrared detection. The collected signal emitted from a solid surface is referred as to photothermal signal. The infrared signal is emitted in the far field and collected by a IR photodetector, then converted into an electrical intensity. By applying a modulated excitation source, the incident thermal wave and the radiated one generate a phase difference, which is correlated to the thermal properties such as the thermal conductivity, the thermal diffusivity and the heat capacity. The sample characteristic length of the solid also depends on the phase decay curve, which can be potentially applied to geometrical quantification or vacancy detection.

The PTR experimental setup developed in the EM2C laboratory is displayed in Figure 9.1. A pump laser with a 532 nm wavelength serves as excitation

source. It is modulated in frequency by an acoustic-optic modulator. The laser is reflected by a tunable mirror and focused on the vertically placed sample. A Thorlab photodiode is placed next to the sample stage to collect the reflected laser power. The emitted infrared thermal wave from the sample surface is collected and focused into an IR detector. A lock-in amplifier is used to record the amplitude of the IR signal and the phase difference between the IR signal and the modulated laser. The measurement is conventionally carried out between 1 Hz and 10000 Hz, based on the thermal properties of the samples as well as their thicknesses. A heating stage can be attached on the back side of the sample, which is compatible to measure the thermoelectric sample.

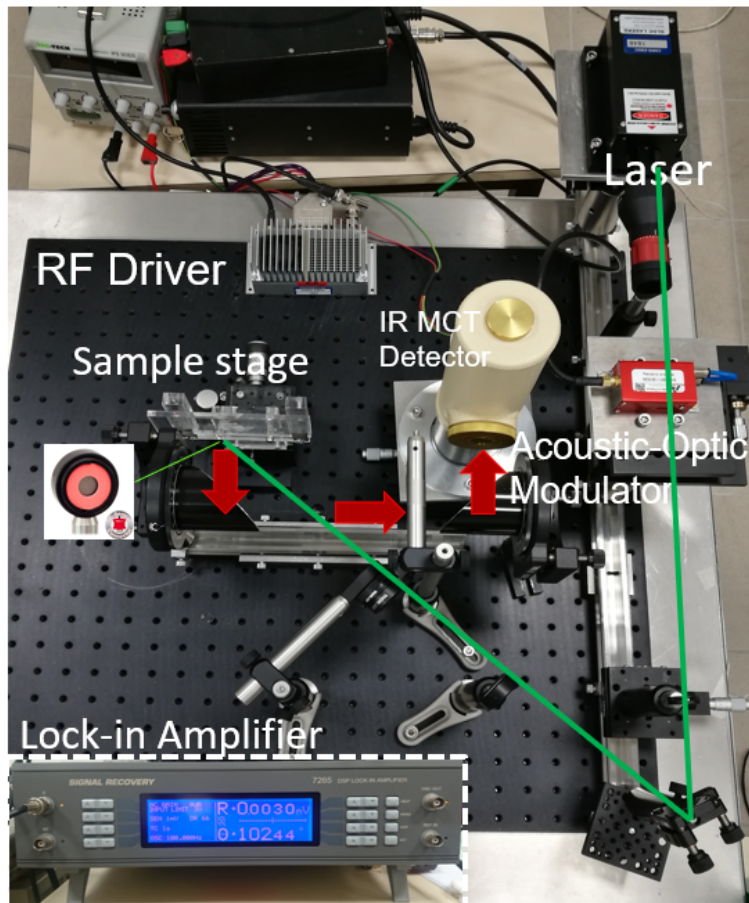


Figure 9.1: Diagram of the PTR experimental setup developed in the EM2C laboratory.

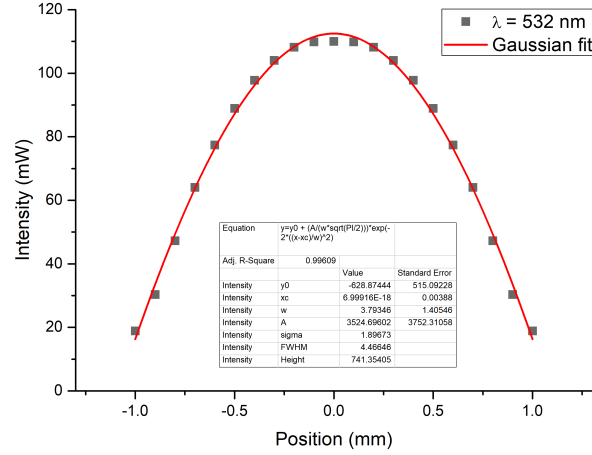


Figure 9.2: Radial profile of the laser beam intensity measured by Thorlab photodiode.

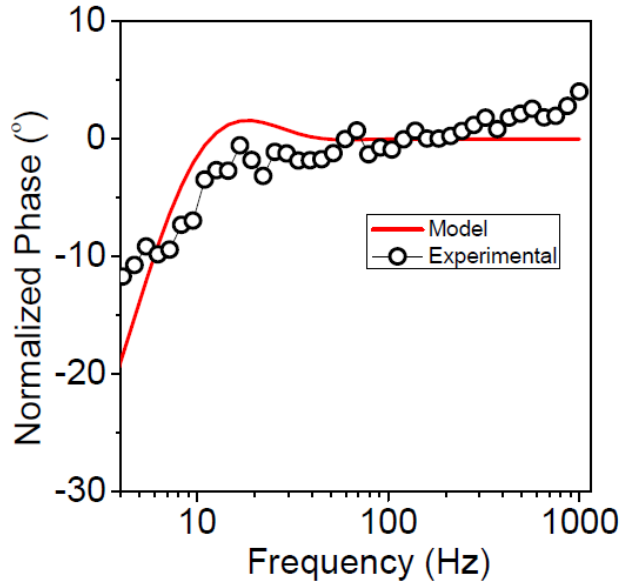


Figure 9.3: Calibration of the PTR phase signal with a 0.5 mm thick stainless steel sample.

We have also performed a calibration of the laser beam diameter as shown in Figure 9.2 and a calibration of a 0.5 mm thick stainless steel sample as shown in Figure 9.3. The experimental phase signal from PTR compare with the monolayer model we provide in the next section. The best fit leads to a thermal conductivity 10 W/m/K, comparable with the reference value 12

W/m/K (provided by engineeringtoolbox.com).

9.2 Heat propagation in layered samples

In the next section, we develop an analytical model to extract the thermal and the geometrical properties of the sample.

9.2.1 Case of a monolayer system

The incident laser with intensity q generates a temperature difference $T(x, y, z, t)$ in the sample. The temperature field is governed by the transient heat conduction equation:

$$\nabla^2 T(x, y, z, t) - \frac{1}{\alpha} \frac{\partial T(x, y, z, t)}{\partial t} = 0 \quad (9.1)$$

where α is the thermal diffusivity.

To simplify the problem, we assume that the thermal diffusion length is much smaller than the diameter of the laser, meaning that the temperature gradient is predominant in the out-of-plane direction. The three dimensional diffusion is then limited to a one dimensional problem, and Equation 9.1 reduces to the form:

$$\frac{\partial^2 T(z, t)}{\partial z^2} - \frac{1}{\alpha} \frac{\partial T(z, t)}{\partial t} = 0 \quad (9.2)$$

By Fourier transformation (see Equation 9.3), the temporal temperature evolution is tuned into a frequency-dependent one as follows Equation 9.4:

$$T(z, t) = \int_{-\infty}^{\infty} \tilde{T}(z, f) e^{2i\pi f t} df \quad (9.3)$$

$$\frac{\partial^2 \tilde{T}(z, f)}{\partial z^2} - \frac{2i\pi f}{\alpha} \frac{\partial \tilde{T}(z, f)}{\partial t} = 0 \quad (9.4)$$

where f is the modulation frequency. Equation 9.4 has a general solution as follows:

$$\tilde{T}(z, f) = T^P (e^{i\sigma z} + R e^{-i\sigma z}) \quad (9.5)$$

where T^P and R are two undefined variables, σ is a complex wavevector with the form as follows:

$$\sigma = \sqrt{\frac{2i\pi f}{\alpha}} \quad (9.6)$$

To find the proper expression of Equation 9.6, one applies the continuity of the heat flux amplitude on the top and bottom surfaces:

(1) on the top surface $z = 0$, the heat convection in air is considered:

$$\kappa \frac{\partial \tilde{T}(f)}{\partial z} = h\tilde{T}(f) - q \quad (9.7)$$

where κ refers to the thermal conductivity and h is the heat exchange coefficient with air.

(2) on the bottom surface $z = l$, where l is the sample thickness. The heat flux conservation leads to:

$$\kappa \frac{\partial \tilde{T}(f)}{\partial z} = -h\tilde{T}(f) \quad (9.8)$$

By combining Equation 9.5 with these two boundary conditions Equation 9.7 and 9.8, one obtains:

$$T^P = \frac{q}{h(1+R) - i\kappa\sigma(1-R)} \quad (9.9)$$

where

$$R = \frac{i\sigma\kappa + h}{i\sigma\kappa - h} e^{2i\sigma l} \quad (9.10)$$

Hence, the frequency-dependent surface temperature $\tilde{T}(z = 0, f)$ is expressed as:

$$\tilde{T}(f) = \frac{q}{h - \frac{i\kappa\sigma}{\gamma}} \quad (9.11)$$

$$\gamma = \frac{1+R}{1-R} = \frac{i\kappa\sigma(1 + e^{2i\sigma l}) - h(1 - e^{2i\sigma l})}{i\kappa\sigma(1 - e^{2i\sigma l}) - h(1 + e^{2i\sigma l})} \quad (9.12)$$

When the thermal diffusion length μ equals to the thickness of the sample l , one obtains a specific modulation frequency $f_c = \frac{\alpha}{\pi l^2}$, called critical frequency.

We list four of the reference samples with well-known thermal properties in Table 9.2.1. The numerical solution is displayed in Figure 9.4 based on Equation 9.11.

Samples	Thickness (mm)	Thermal Conductivity (W/mK)	Thermal Diffusivity (mm ² /s)	Critical Frequency (Hz)
Stainless Steel	0.5	10	3.87	4.93
Vitreous Carbon	0.5	6.3	6	0.48
Silver	0.5	429	165.63	210.88
Copper	0.5	111	401	141.33

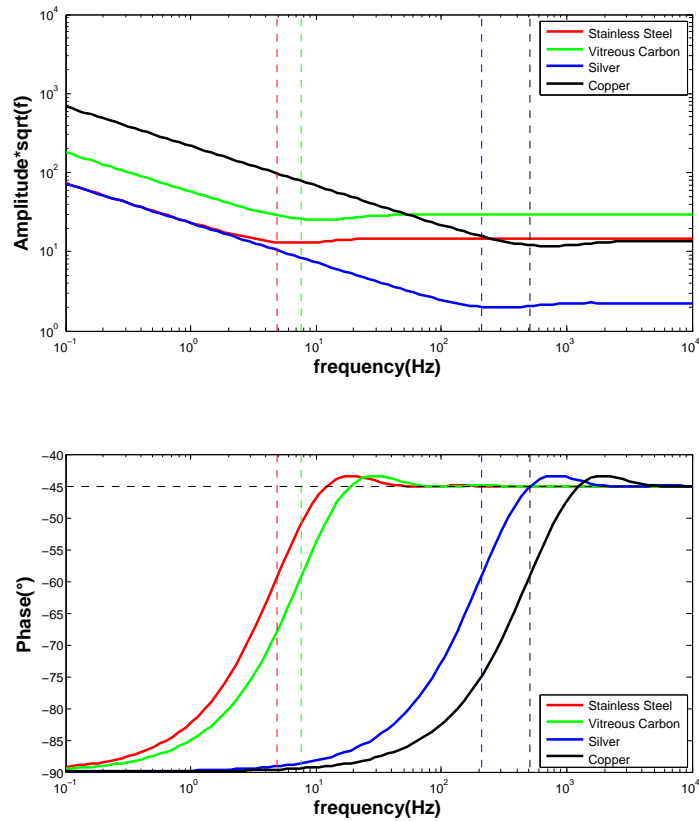


Figure 9.4: Amplitude and phase of the radiative thermal waves as a function of modulated frequency, for four different samples: Stainless Steel (red); Vitreous Carbon (green); Silver (blue); Copper (black). The vertical dotted lines refer to the critical frequencies.

From the Figure 9.4, one observes that the critical frequency indicates the minimum of the amplitude and the transient in phase. This quantity is useful in the experiment to specify the transient region.

9.2.2 Case of a bilayer system

In the following, we solve the one dimensional heat conduction problem for a bilayer system. This model can be applied to characterize a system consisting of a thin film deposited onto a finite or semi-infinite substrate. Each thermal or geometrical property can be analysed individually.

We define the temperature profile in the first layer and in the second layer by $\widetilde{T}_1(z, f)$ and $\widetilde{T}_2(z, f)$, respectively as follows:

$$\widetilde{T}_1(z, f) = T_1^P (e^{i\sigma_1 z_1} + R e_1^{-i\sigma_1 z_1}) \quad (9.13)$$

$$\widetilde{T}_2(z, f) = T_2^P (e^{i\sigma_2 z_2} + R e_2^{-i\sigma_2 z_2}) \quad (9.14)$$

Another boundary condition represents the heat transfer at the interface of these two layers:

(1) heat flux is continuous at the interface $z = z_1$:

$$\kappa_1 \frac{\partial \widetilde{T}_1(f)}{\partial z} = \kappa_2 \frac{\partial \widetilde{T}_2(f)}{\partial z} \quad (9.15)$$

where z_1 refers to the thickness of the top layer.

(2) temperature is discontinuous due to the thermal interfacial resistance and the corresponding condition can be written as:

$$\widetilde{T}_2(f) - \widetilde{T}_1(f) = R_{th} \kappa_2 \frac{\partial \widetilde{T}_2(f)}{\partial z} \quad (9.16)$$

If thermal interfacial resistance is negligible, Equation 9.16 leads to:

$$\widetilde{T}_2(f) = \widetilde{T}_1(f) \quad (9.17)$$

(3) on the top surface $z = 0$, the sample surface is heated up by a modulated source with intensity q as follows:

$$\kappa \frac{\partial \widetilde{T}_1(f)}{\partial z} = h \widetilde{T}_1(f) - q \quad (9.18)$$

(4) on the bottom surface $z = l_1 + l_2$, the heat flux continuity leads to:

$$\kappa \frac{\partial \widetilde{T}_2(f)}{\partial z} = -h \widetilde{T}_2(f) \quad (9.19)$$

Taking into account these four Equations 9.15 9.16 9.18 9.19, one obtains a proper form of the temperature profile as follows:

$$T_1^P = \frac{q}{h(1 + R_1) - i\kappa_1\sigma_1(1 - R_2)} \quad (9.20)$$

where R_1 and R_2 have the expressions as follows:

$$R_1 = \frac{(1 + R_2) - \epsilon_{21}(1 - R_2)}{(1 + R_2) + \epsilon_{21}(1 - R_2)} e^{2i\sigma_1 l_1} \quad (9.21)$$

$$R_2 = \frac{i\sigma_2\kappa_2 + h}{i\sigma_2\kappa_2 - h} e^{2i\sigma_2 l_2} \quad (9.22)$$

where ϵ_{21} is the thermal effusivity from layer 2 to layer 1:

$$\epsilon_{21} = \frac{\sigma_2\kappa_2}{\sigma_1\kappa_1} \quad (9.23)$$

Hence, the surface temperature $\widetilde{T}_1(z = 0, f)$ have the expression:

$$\widetilde{T}_1(f) = \frac{q}{h - \frac{i\kappa_1\sigma_1}{\gamma_1}} \quad (9.24)$$

where γ_1 and γ_2 can be written as:

$$\gamma_1 = \frac{1 + R_1}{1 - R_1} = \frac{\epsilon_{21}\tanh(i\sigma_1 l_1) - \gamma_2}{\epsilon_{21} + \gamma_2 \tanh(i\sigma_1 l_1)}, \quad (9.25)$$

$$\gamma_2 = \frac{1 + R_2}{1 - R_2} = \frac{i\sigma_2\kappa_2 + h \tanh(i\sigma_2 l_2)}{-i\sigma_2\kappa_2 \tanh(i\sigma_2 l_2) - h} \quad (9.26)$$

In Figure 9.5, we plot the PTR signal of a 0.5 mm thick stainless steel sample with deposited gold layers of different thickness. The PTR signal strongly depends on the thickness of the gold deposition. One observes that at high frequency, a thicker the gold layer leads to a lower of the amplitude. It implies that when the thickness of the gold layer exceed a certain value, the surface temperature is decreased and the interfacial resistance is no longer negligible.

The thermal diffusion length is defined as $\mu = (\alpha/\pi f)^{\frac{1}{2}}$ where α corresponds to the thermal diffusivity and f refers to the excitation frequency. This quantity correlates to the probing depth. It is defined to be inverse proportional to the frequency, i.e. to measure the thinner sample, higher frequency is required.

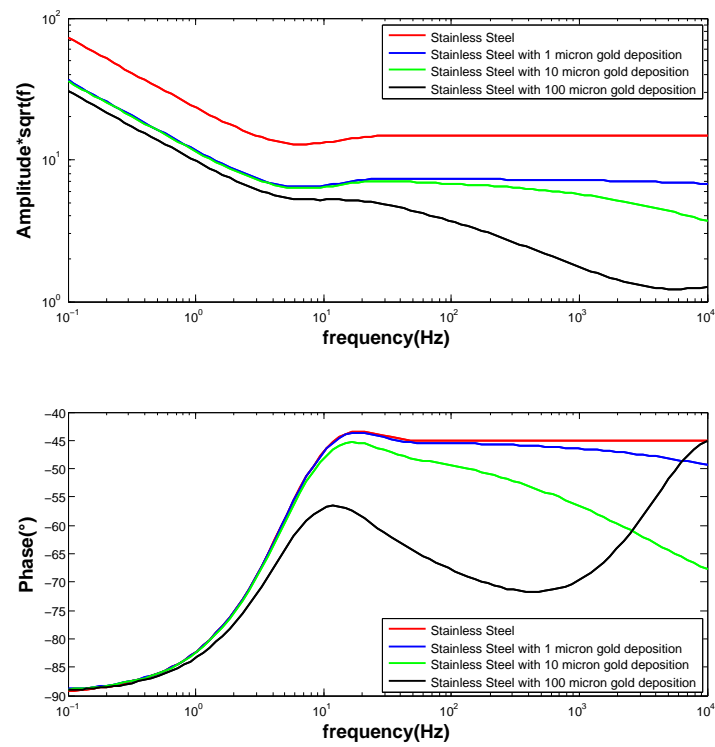


Figure 9.5: PTR signal as a function of the modulated frequency based on a 0.5 mm thick stainless steel sample with no deposition (red line); with 1 μm (blue line), 10 μm (green line) and 100 μm (black line) thick gold film deposition.

9.3 Conclusion

In this chapter, we provide an overview of the photothermal radiometry technique, which based on a modulated laser excitation and the infrared detection in the far field. This non-destructive characterization can be applied on the investigation of the thermal properties of bulk or thin layered materials. We provide the analytical model based on a single suspended film or a thin film deposited on the substrate. This model can be applied in photothermal measurement and provide a quantitative study.

Chapter 10

$Bi_2Te_xSe_{3-x}$ nanostructured film synthesis and thermal characterization

Recent attention was drawn by the high ZT value of thermoelectric materials improved by nanostructuring. One case is the one of bismuth telluride, a material known to have the best thermoelectric performances around room temperature. This chapter reports a collaborative project between EM2C laboratory and Thales R&D. In this chapter, the synthesis of nanocomposite $Bi_2Te_xSe_{3-x}$ will be briefly provided and the thermal characterization by PTR in the EM2C laboratory will be analysed.

10.1 Synthesis method of $Bi_2Te_xSe_{3-x}$ alloy films

Bismuth telluride is a material known to have the best thermoelectric performances around the ambient temperature. By optimizing the composition with selenium and nanostructuring, the goal is to minimize the thermal conduction whereas the electrical conductivity is maintained. One common interest of this study is to search the optimum of the synthesis method to maximize the size effect.

The synthesis of samples with various compositions is done by adjusting the concentrations of the various precursor salts of bismuth, tellurium and selenium according to the target composition $Bi_2Te_xSe_{3-x}$ ($0 \leq x \leq 3$) as shown below. In order to verify the feasibility of this approach, four synthesis are carried out with Bi_2Te_3 as target composition, Bi_2Te_3 , Bi_2Te_2 and Bi_2Te thus allowing us to control a wide range of compositions. For these synthesis, the reaction reducer, hydroxylamine, is added to the reaction medium by rapid injection with the aid of a dropping funnel and the reaction then continues for 30 mins. More details regarding to the synthesis process can be found in [Bude \(2018\)](#).

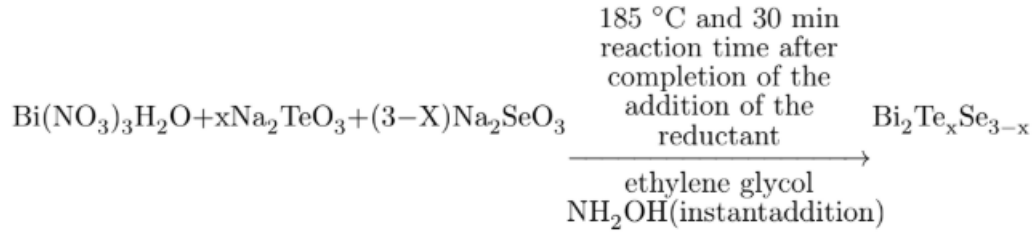


Figure 10.1: Schematic of the synthesis process.

The next step is to compact the obtained powder into massive disk-shaped samples as shown in 10.3. The compression leads to obtaining dense materials with highlighted size effects. The shaping process is done by a piston coupled with a thermocouple. After the first pressing at room temperature under vacuum for 20 mins, a heating resistor heats up the powder during the second pressing. A 30 mins thermalization after pressing should be noticed.

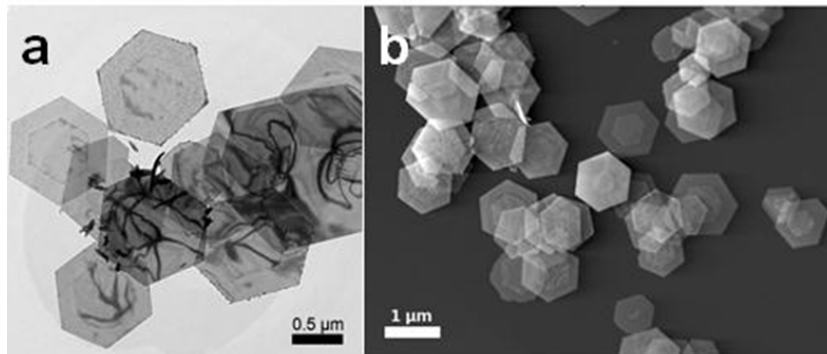


Figure 10.2: SEM images of disk-shaped of $Bi_2Te_{2.85}Se_{0.15}$ (Bude (2018)).

10.2 Photothermal characterization of $Bi_2Te_xSe_{3-x}$ alloy films

One of our interest is to investigate the thermal properties after the optimized synthesis and heterostructuring. Before conducting a photothermal characterization by PTR, we develop an analytical model to study the size effect on thermal conductivity of the disk-shape nanograins.

In the Figure 10.3, one presents an analogical schematic of the disk-shaped nanograins after pressing and drying processes. The thickness of the nanograins on averages is 10 nm. And the porosity of the pressed sample is approximately 0.1 due to the high temperature pressing and drying.

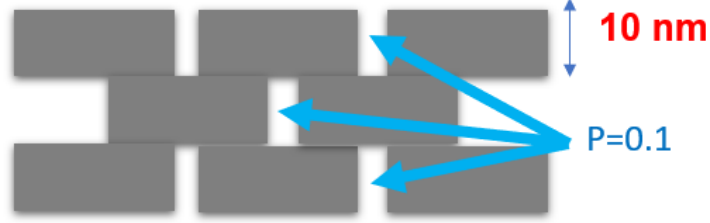


Figure 10.3: Analogical schematic of disk-shaped nanograins after pressing and drying. The thickness of the nanograins averages 10 nm. And the porosity of the pressed sample is approximately 0.1.

The analytical thermal conductivity model targeting the low porosities and deformed particles is proposed by [Ordenez-Miranda et al. \(2016\)](#), and it yields:

$$k = k_m(1 - p)^n, \quad (10.1)$$

$$n = \frac{3L + 1}{6L(1 - L)}, \quad (10.2)$$

where k is the thermal conductivity of the porous sample, k_m is the thermal conductivity of the matrix, p is the porosity and L is the geometrical factor L which depends on the aspect ratio $\rho = b/a > 1$ with b is the diameter and a is the thickness and it yields:

$$L = 1 - \frac{\text{arccosh}(\rho)}{\rho\sqrt{\rho^2 - 1}}, \quad (10.3)$$

By inputting the known parameters from [Bude \(2018\)](#), we obtained the thermal conductivity through the Equation 10.2: 0.12 W/m/K for $Bi_2Te_{2.85}Se_{0.15}$, 0.33 W/m/K for Bi_2Te_3 , 0.18 W/m/K for $Bi_2Te_{1.5}Se_{1.5}$ and 0.24 W/m/K for Bi_2Se_3 . The predicted values indicate that the doping of selenium significantly decreases the thermal conductivity of Bi_2Te_3 alloy film.

In Figures 10.4, we compare the theoretical predictions with the calculated and the experimental results. The prediction $k = 0.12W/m/K$ reveals a satisfying agreement. A calibration of the amplitude of the PTR signal of a 0.5 mm thick stainless steel shown in the insert figure. The measurement for a modulation frequency higher than 10 Hz is more reliable.

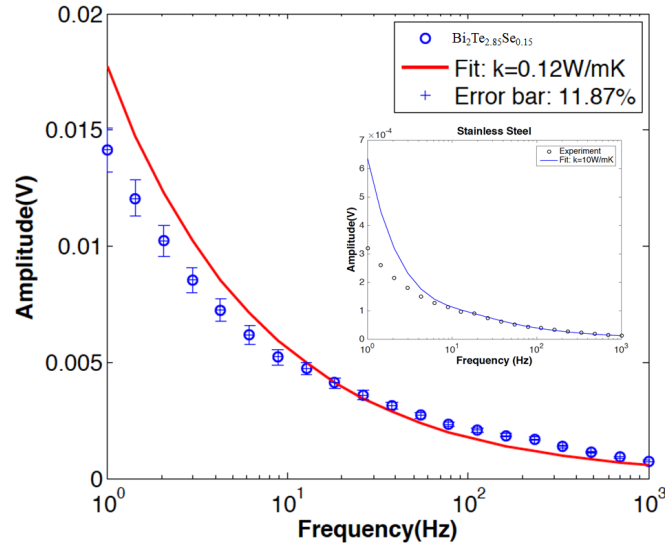


Figure 10.4: Amplitude of PTR signal (blue circle) compared to the theoretical prediction (red curve) of $Bi_2Te_{2.85}Se_{0.15}$ alloy film. The inset figure highlights a calibration of the amplitude of the PTR signal of a 0.5 mm thick stainless steel.

In Figure 10.5, we compare the theoretical predictions with the calculated and the experimental results. The predicted thermal conductivities do not agree well with the experimental data at the low frequency regime. The disagreement imply the nanograins are no longer deformed in disk-shape but potentially merging into cluster form. The merge of nanograins reduces the interfacial thermal resistance between the nanograins and leads to the effective thermal conductivity higher than the theoretical prediction. This hypothesis should be verified by SEM in the future investigation.

10.3 Conclusion

In this chapter, we introduce briefly the synthesis of the $Bi_2Te_xSe_{3-x}$ alloy films. The synthesis of samples with various compositions is done by adjusting the concentrations of the various precursor salts of bismuth, tellurium and selenium according to the target composition $Bi_2Te_xSe_{3-x}$ ($0 \leq x \leq 3$). The next step is to compact the obtained powder of massive disk-shaped samples with a piston at high temperature. This compression leads to obtain dense materials with highlighted size effects. An analytical thermal conductivity model based on the deformed particle shape is applied. The compressed sample is measured by PTR developed at the EM2C laboratory. The experimental results imply that the merging of the nanograins occurs and leads to an effective thermal

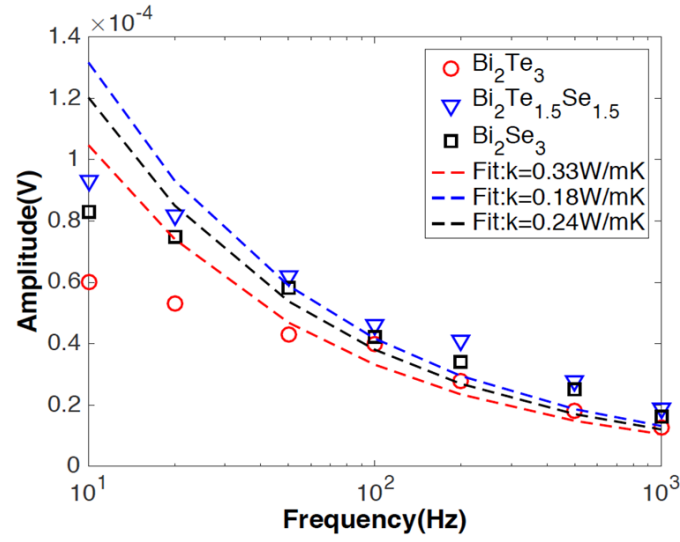


Figure 10.5: Amplitude of PTR signal compared to the theoretical prediction of Bi_2Te_3 , $\text{Bi}_2\text{Te}_{1.5}\text{Se}_{1.5}$ and Bi_2Se_3 alloy film.

conductivity higher than the one obtained by our model.

Conclusion

In this thesis, our interest was to investigate the size effects on the SPhPs modes supported by a dielectric medium and the phonon transport in insulating materials such as silicon based phononic crystals or thermoelectric materials. In the second chapter of this work, we explore the fundamental description of the excitation and propagation of the SPhPs modes quantifies in two cases: a single interface of air-dielectric and a suspended dielectric film surrounded by air. Furthermore, we developed the formalism which quantify the contribution of the SPhPs modes to in-plane thermal conductivity based on the Boltzmann transport equation. Our parametric study is mainly dedicated to the SiN sub-micron film, due to the fact that it is industrially widely used as an insulating layer for MEMs, and also that it can serve as a substrate for biological sample observation in-situ TEM. These applications require consistent thermal properties of the SiN film, nevertheless, have not been well investigated yet. We believe that our results with temperature- and thickness dependence can be used as a reference to improve the reliability in other research fields.

We have measured the in-plane thermal conductivity of the SiN film by TDTR technique. The results obtained at high temperatures reveal that the SPhPs thermal conductivity exceeds the phonon thermal conductivity when the SPhPs modes are thermally excited in the 50 nm film, whereas the 200 nm film remains temperature independent.

We have also developed an analytical model to quantitatively study the heat dissipation by natural convection in the phononic crystals. Our results indicate that the air-losses can reach more than 40 % and this result is essential to evaluate the performance of the thermoelectric devices such as phononic crystals due to the fact that those are operating in air. The geometrical effects are hence taken into account.

Last but not least, we developed an analytical thermal conductivity model based on the particle shape. The compressed sample is measured by PTR developed at the EM2C laboratory. The experimental results imply that the merging of the nanograins occurs and leads to an effective thermal conductivity higher than the one obtained by our model.

To conclude, this thesis provides, on one hand, the first qualitative proof of the contribution of SPhPs to thin film in-plane thermal conductivity. This proof has to be further confirmed in terms of quantitative estimations by taking into account parasitic effects such as the modification of the dielectric function with temperature and size as well as the specification of the coupling between phonon and SPhPs systems. On the other hand, phonon transport was addressed in two film configurations. First, a complete model describing the size effects on the thermal conductivity of Phononic Crystals including the contribution of losses in air was proposed. The heat transfer coefficient was found to increase as hole diameter decreases reaching several thousands of $W/m^2/K$, while the coefficient of the pristine membrane remains below $100 W/m^2/K$. Those highly dissipative membranes should be relevant to the thermal management of integrated systems. Second, the thermal conductivity of nanostructure thermoelectric alloy materials was measured and the impact of nanostructuration demonstrated based on a porous medium model. The obtained substantial thermal conductivity decrease is promising for the design of future thermoelectric materials.

References

- Anufriev, R., J. Maire, and M. Nomura (2016, jan). Reduction of thermal conductivity by surface scattering of phonons in periodic silicon nanostructures. *Physical Review B* 93(4), 045411. (p. [xiv](#), [15](#), [39](#))
- Anufriev, R., A. Ramiere, J. Maire, and M. Nomura (2017). Heat guiding and focusing using ballistic phonon transport in phononic nanostructures. *Nature communications* 8, 15505. (p. [39](#), [44](#))
- Anufriev, R., R. Yanagisawa, and M. Nomura (2017, oct). Aluminium nanopillars reduce thermal conductivity of silicon nanobeams. *Nanoscale* 9(39), 15083–15088. (p. [xiv](#), [xvii](#), [15](#), [44](#))
- Balandin, A. A. and D. L. Nika (2012, jun). Phononics in low-dimensional materials. *Materials Today* 15(6), 266–275. (p. [7](#))
- Baxter, J., Z. Bian, G. Chen, D. Danielson, M. S. Dresselhaus, A. G. Fedorov, T. S. Fisher, C. W. Jones, E. Maginn, U. Kortshagen, A. Manthiram, A. Nozik, D. R. Rolison, T. Sands, L. Shi, D. Sholl, and Y. Wu (2009, jun). Nanoscale design to enable the revolution in renewable energy. *Energy & Environmental Science* 2(6), 559. (p. [xiii](#), [7](#), [8](#))
- Biswas, K., J. He, I. D. Blum, C.-I. Wu, T. P. Hogan, D. N. Seidman, V. P. Dravid, and M. G. Kanatzidis (2012). High-performance bulk thermoelectrics with all-scale hierarchical architectures. *Nature* 489(7416), 414. (p. [5](#), [19](#))
- Bude, R. (2018). Synthèses et caractérisations de matériaux thermoélectriques nanostructurés. Technical report. (p. [xx](#), [93](#), [94](#), [95](#))
- Button, K. J. (1983). *Infrared and millimeter waves Volume 8, Electromagnetic waves in matter. Part I*. Academic Press. (p. [26](#))
- Cahill, D. G., W. K. Ford, K. E. Goodson, G. D. Mahan, A. Majumdar, H. J. Maris, R. Merlin, and S. R. Phillpot (2003). Nanoscale thermal transport. *Journal of applied physics* 93(2), 793–818. (p. [5](#), [19](#))
- Cataldo, G., J. A. Beall, H.-M. Cho, B. McAndrew, M. D. Niemack, and E. J. Wollack (2012). Infrared dielectric properties of low-stress silicon nitride. (p. [26](#))
- Chen, D.-Z. and G. Chen (2010). Heat flow in thin films via surface phonon-polaritons. *Frontiers in Heat and Mass Transfer (FHMT)* 1(2). (p. [7](#), [19](#))
- Chen, D.-Z. A. and G. Chen (2007). Measurement of silicon dioxide sur-

- face phonon-polariton propagation length by attenuated total reflection. *Applied Physics Letters* 91(12), 121906. (p. 7, 19)
- Chen, D.-Z. A., A. Narayanaswamy, and G. Chen (2005a). Surface phonon-polariton mediated thermal conductivity enhancement of amorphous thin films. *Physical Review B* 72(15), 155435. (p. 10, 19)
- Chen, D.-Z. A., A. Narayanaswamy, and G. Chen (2005b, Oct). Surface phonon-polariton mediated thermal conductivity enhancement of amorphous thin films. *Phys. Rev. B* 72, 155435. (p. 29)
- Cuffe, J., J. K. Eliason, A. A. Maznev, K. C. Collins, J. A. Johnson, A. Shchepetov, M. Prunnila, J. Ahopelto, C. M. Sotomayor Torres, G. Chen, and K. A. Nelson (2015, jun). Reconstructing phonon mean-free-path contributions to thermal conductivity using nanoscale membranes. *Physical Review B* 91(24), 245423. (p. 78)
- Dusastre, V. (2011). *Materials for sustainable energy: a collection of peer-reviewed research and review articles from Nature Publishing Group*. World Scientific. (p. 5, 19)
- Feurer, T., N. S. Stoyanov, D. W. Ward, J. C. Vaughan, E. R. Statz, and K. A. Nelson (2007, aug). Terahertz Polaritonics. *Annual Review of Materials Research* 37(1), 317–350. (p. 10)
- Gluchko, S., B. Palpant, S. Volz, R. Braive, and T. Antoni (2017). Thermal excitation of broadband and long-range surface waves on sio2 submicron films. *Applied Physics Letters* 110(26), 263108. (p. xiv, 10, 11, 19)
- Goodson, K. E. (1996). Thermal Conduction in onhomogeneous. CVD eamond Layers =n Electronic Microstructures. Technical report. (p. 5)
- Graczykowski, B., A. El Sachat, J. S. Reparaz, M. Sledzinska, M. R. Wagner, E. Chavez-Angel, Y. Wu, S. Volz, Y. Wu, F. Alzina, and C. M. Sotomayor Torres (2017, dec). Thermal conductivity and air-mediated losses in periodic porous silicon membranes at high temperatures. *Nature Communications* 8(1), 415. (p. xviii, xix, 69, 70, 71)
- Greffet, J.-J., R. Carminati, K. Joulain, J.-P. Mulet, S. Mainguy, and Y. Chen (2002). Coherent emission of light by thermal sources. *Nature* 416(6876), 61. (p. 19)
- Griffin Jr, A., F. Brotzen, and P. Loos (1994). The effective transverse thermal conductivity of amorphous si3n4 thin films. *Journal of applied physics* 76(7), 4007–4011. (p. xvi, 34, 35, 54)
- Huang, K. (1951, may). Lattice Vibrations and Optical Waves in Ionic Crystals. *Nature* 167(4254), 779–780. (p. 9)
- Joseph, F. J. B. (1822). Théorie analytique de la Chaleur. Technical report. (p. 3)
- Joulain, K., J.-P. Mulet, F. Marquier, R. Carminati, and J.-J. Greffet (2005, apr). Surface Electromagnetic Waves Thermally Excited: Radiative Heat Transfer, Coherence Properties and Casimir Forces Revisited in the Near Field. (p. xiv, 8, 9)
- Kadoya, K., N. Matsunaga, and A. Nagashima (1985, oct). Viscosity and

- Thermal Conductivity of Dry Air in the Gaseous Phase. *Journal of Physical and Chemical Reference Data* 14(4), 947–970. (p. 72)
- Lee, S.-M. and D. G. Cahill (1997). Heat transport in thin dielectric films. *Journal of applied physics* 81(6), 2590–2595. (p. xvi, 34, 35, 54)
- Lerario, G., A. Fieramosca, F. Barachati, D. Ballarini, K. S. Daskalakis, L. Dominici, M. De Giorgi, S. A. Maier, G. Gigli, S. Kéna-Cohen, and D. Sanvitto (2017, jun). Room-temperature superfluidity in a polariton condensate. *Nature Physics* 13(9), 837–841. (p. 10)
- Mastrangelo, C. H., Y.-C. Tai, and R. S. Muller (1990). Thermophysical properties of low-residual stress, silicon-rich, lpcvd silicon nitride films. *Sensors and Actuators A: Physical* 23(1-3), 856–860. (p. xvi, 34, 35)
- Minnich, A. J., M. S. Dresselhaus, Z. F. Ren, and G. Chen (2009, may). Bulk nanostructured thermoelectric materials: current research and future prospects. *Energy & Environmental Science* 2(5), 466. (p. xiv, 13, 14)
- Mulet, J.-P., K. Joulain, R. Carminati, and J.-J. Greffet (2001). Nanoscale radiative heat transfer between a small particle and a plane surface. *Applied Physics Letters* 78(19), 2931–2933. (p. 7, 19)
- Nomura, M. (2016). Control of Phonon Transport by Phononic Crystals and Application to Thermoelectric Materials *. (p. xiii, 4)
- Ordonez-Miranda, J., M. Hermens, I. Nikitin, V. G. Kouznetsova, O. van der Sluis, M. A. Ras, J. Reparaz, M. Wagner, M. Sledzinska, J. Gomis-Bresco, C. Sotomayor Torres, B. Wunderle, and S. Volz (2016, oct). Measurement and modeling of the effective thermal conductivity of sintered silver pastes. *International Journal of Thermal Sciences* 108, 185–194. (p. 95)
- Ordonez-Miranda, J., L. Tranchant, T. Tokunaga, B. Kim, B. Palpant, Y. Chalopin, T. Antoni, and S. Volz (2013). Anomalous thermal conductivity by surface phonon-polaritons of polar nano thin films due to their asymmetric surrounding media. *Journal of Applied Physics* 113(8), 084311. (p. 10, 19, 25)
- Otto, A. (1968, aug). Excitation of nonradiative surface plasma waves in silver by the method of frustrated total reflection. *Zeitschrift für Physik A Hadrons and nuclei* 216(4), 398–410. (p. 9)
- Palik, E. D. (1998). *Handbook of optical constants of solids*. Academic Press. (p. 26)
- Pokatilov, E., D. Nika, and A. Balandin (2005a). Acoustic-phonon propagation in rectangular semiconductor nanowires with elastically dissimilar barriers. *Physical Review B* 72(11), 113311. (p. xiii, 6)
- Pokatilov, E. P., D. L. Nika, and A. A. Balandin (2004, aug). A phonon depletion effect in ultrathin heterostructures with acoustically mismatched layers. *Applied Physics Letters* 85(5), 825–827. (p. xiii, 6)
- Pokatilov, E. P., D. L. Nika, and A. A. Balandin (2005b). Acoustic phonon engineering in coated cylindrical nanowires. *Superlattices and Microstructures* 38, 168–183. (p. xiii, 6)

- Queen, D. and F. Hellman (2009). Thin film nanocalorimeter for heat capacity measurements of 30 nm films. *Review of Scientific Instruments* 80(6), 063901. (p. *xvi*, 35)
- Reparaz, J. S., E. Chavez-Angel, M. R. Wagner, B. Graczykowski, J. Gomis-Bresco, F. Alzina, and C. M. S. Torres (2014). A novel contactless technique for thermal field mapping and thermal conductivity determination: Two-Laser Raman Thermometry. *REVIEW OF SCIENTIFIC INSTRUMENTS* 85, 34901. (p. 70)
- Rousseau, E., A. Siria, G. Jourdan, S. Volz, F. Comin, J. Chevrier, and J.-J. Greffet (2009, sep). Radiative heat transfer at the nanoscale. *Nature Photonics* 3(9), 514–517. (p. *xiv*, 7, 9)
- Sledzinska, M., B. Graczykowski, F. Alzina, J. Santiso Lopez, and C. Sotomayor Torres (2016, jan). Fabrication of phononic crystals on free-standing silicon membranes. *Microelectronic Engineering* 149, 41–45. (p. 69)
- Staude, I. and C. Rockstuhl (2016, aug). To scatter or not to scatter. *Nature Materials* 15(8), 821–822. (p. 7)
- Thi Ha, D., D. Thi Thuy, V. Thi Hoa, T. Thi Thanh Van, and N. Ai Viet (2017). On the theory of three types of polaritons (phonon, exciton and plasmon polaritons). *J. Phys* 865, 12007. (p. 10)
- Tolpygo, K. B. (1950). PHYSICAL PROPERTIES OF A ROCK SALT LATTICE MADE UP OF DEFORMABLE IONS. Technical report. (p. 9)
- Tsintzos, S. I., N. T. Pelekanos, G. Konstantinidis, Z. Hatzopoulos, and P. G. Savvidis (2008, may). A GaAs polariton light-emitting diode operating near room temperature. *Nature* 453(7193), 372–375. (p. 10)
- Volz, S., J. Ordonez-Miranda, A. Shchepetov, M. Prunnila, J. Ahopelto, T. Pezeril, G. Vaudel, V. Gusev, P. Ruello, E. M. Weig, et al. (2016). Nanophononics: state of the art and perspectives. *The European Physical Journal B* 89(1), 15. (p. 5, 19)
- Volz, S., J. Shiomi, M. Nomura, and K. Miyazaki (2016). Heat conduction in nanostructured materials. *Journal of Thermal Science and Technology* 11(1), JTST0001–JTST0001. (p. 5, 19)
- Von Lukowicz, M., E. Abbe, T. Schmiel, M. Tajmar, M. von Lukowicz, E. Abbe, T. Schmiel, and M. Tajmar (2016, jul). Thermoelectric Generators on Satellites—An Approach for Waste Heat Recovery in Space. *Energies* 9(7), 541. (p. *xiv*, 12)
- Yang, F., J. R. Sambles, and G. W. Bradberry (1991, sep). Long-range surface modes supported by thin films. *Physical Review B* 44(11), 5855–5872. (p. 25)
- Yeh, C. and F. I. Shimabukuro (2008). *The Essence of Dielectric Waveguides*. Boston, MA: Springer US. (p. 24, 25)
- Yu, P. Y. and M. Cardona (2010). Fundamentals of Semiconductors: Physics and Materials Properties, 4th Edition. Technical report. (p. *xiv*, 10)
- Zamfirescu, M., A. Kavokin, B. Gil, G. Malpuech, and M. Kaliteevski (2002,

- apr). ZnO as a material mostly adapted for the realization of room-temperature polariton lasers. *Physical Review B* 65(16), 161205. (p. 10)
- Zeng, T. and G. Chen (2001, apr). Phonon Heat Conduction in Thin Films: Impacts of Thermal Boundary Resistance and Internal Heat Generation. *Journal of Heat Transfer* 123(2), 340. (p. 5)

Titre : Etude expérimentale des effets de taille sur les phonon polaritons de surface et le transport de phonon

Mots clés : transfert de chaleur, conductivité thermique, ondes de surface, phonon polaritons de surface, rayonnement de champ proche, thermoréfectance dans le domaine temporel, radiométrie photothermique.

Résumé : La conduction thermique devient moins efficace à mesure que la taille des structures diminue en dessous du micron, car la diffusion de surface des phonons devient prédominante et limite plus efficacement les phonons que la diffusion phonon-phonon Umklapp. Des études récentes ont indiqué que les phonon polaritons de surface (SPhPs), qui sont les ondes électromagnétiques évanescentes générées par l'hybridation des phonons optiques et des photons et se propageant à la surface d'une surface diélectrique polaire, pourraient servir de nouveaux vecteurs de chaleur pour améliorer les performances thermiques dans des dispositifs micro- et nano-métriques. Nous étudions l'état des SPhPs existant dans un film submicronique diélectrique dans une

large gamme de fréquences. Le calcul de la conductivité thermique des SPhPs basé sur l'équation de transport de Boltzmann (BTE) montre que le flux de chaleur transporté par les SPhPs est supérieur à celui des phonons. Nous effectuons également une mesure de réflectance thermique dans le domaine temporel (TDTR) de films submicroniques de SiN et démontrons que la conductivité thermique due aux SPhPs à haute température augmente lorsque l'épaisseur du film diminue. Les résultats présentés dans cette thèse ont des applications potentielles dans le domaine du transfert de chaleur, de la gestion thermique, du rayonnement en champ proche et de la polaritoniques.

Title : Experimental Investigation of Size Effects on Surface Phonon Polaritons and Phonon Transport

Keywords : heat transfer, thermal conductivity, surface waves, Surface Phonon Polaritons, near-field radiation, time domain thermal reflectance, photo thermal radiometry.

Abstract : Thermal conduction becomes less efficient as structures scale down into submicron sizes since phonon-boundary scattering becomes predominant and impedes phonons more efficiently than Umklapp scattering. Recent studies indicated that the surface phonon polaritons (SPhPs), which are the evanescent electromagnetic waves generated by the hybridation of the optical phonons and the photons and propagating at the surface of a polar dielectric material surface, potentially serve as novel heat carriers to enhance the thermal performance in micro- and nanoscale devices. We study the condition of SPhPs existing in a dielectric submicron film with

a broad frequency range. The calculation of SPhPs thermal conductivity based on Boltzmann transport equation (BTE) demonstrates that the heat flux carried by SPhPs exceeds the one carried by phonons. We also conduct a time-domain-thermal-reflectance (TDTR) measurement of SiN submicron films and demonstrate that the thermal conductivity due to the SPhPs at high temperatures increases by decreasing the film thickness. The results presented in this thesis have potential applications in the field of heat transfer, thermal management, near-field radiation and polaritonics.